POLITECNICO DI TORINO

SCUOLA DI DOTTORATO
Dottorato in Fluidodinamica – XX ciclo

Doctoral Dissertation

Mesoscale Vortices, Lagrangian Transport and Marine Ecosystem Dynamics

Inga Koszalka

Tutors **Coordinator of the doctorate course**

Prof. Antonello Provenzale & Dr. Annalisa Bracco

Reviewer

Dr. Jeffrey B. Weiss Prof. Luca Zannetti

Summary

Ocean dynamics at mesoscales and submesoscales (horizontal length scales between about 1 and 500 km) is strongly influenced by the presence of coherent vortices (*eddies*). These are low-frequency energy fluctuations (having a life span ranging from a few weeks to several months) and play an important role in global transport and mixing processes. Recent observations suggest that eddies can draw nutrients from the deep layers up to the surface, fertilizing the waters, creating blooms of phytoplankton in the open ocean, and export the organic matter to the sea bed (Sweeney *et al.*, 2003; McGillicuddy *et al.*, 2007; Benitez-Nelson *et al.*, 2007). Despite their importance, a detailed, three-dimensional study of ocean coherent vortices is still lacking. It is therefore difficult to quantify and parameterize their role in biogeochemical cycling.

In my dissertation, I concentrate on ocean eddies with the goal of improving our understanding of mesoscale turbulence and of its interplay with the marine ecosystem. First of all, I investigate numerically how spatial-temporal variability, coupled with horizontal advection by a flow populated by mesoscale vortices, can disguise limit cycle behavior (self-sustained oscillations) in planctonic populations to the point that it cannot be detected in fixed-point measurements of plankton abundance.

Secondly, with a primitive-equation model I simulate and study the three-dimensional structure of mesoscale eddies. The flow I consider is surface-intensified, quasi two-dimensional (averaged horizontal velocities are more than two orders of magnitude larger than vertical ones), characterized by small average Rossby number and by small Rossby deformation radius, and therefore dominated by coherent anticyclones. The vortical motion dominates the divergent component and the horizontal circulation displays transport and mixing properties similar to those of two-dimensional barotropic and quasigeostrophic turbulence.

Analyzing the vertical circulation, on the other hand, I find that the contributions related to the presence of vortices, filaments, vortex Rossby waves, as well as their interactions with Ekman circulation and inertial-internal waves, feature a complexity inaccessible to the simpler quasigeostrophic and shallow-water formulations. Vertical velocities reach instantaneous values up to 100 m/day, that is one order of magnitude larger than in large-scale upwelling areas, and exhibit a fine spatial structure not correlated with relative vorticity. The distribution of vertical velocities is non-Gaussian, with long tails associated with high values found inside and around the vortices. These intense vertical motions are responsible for large vertical excursions of Lagrangian tracers.

In light of the recent observations on the crucial role played by mesoscale eddies in the marine ecosystem and ocean biochemistry (McGillicuddy *et al.*, 2007; Benitez-Nelson *et al.*, 2007), my results emphasize the three-dimensional complexity of the dynamics of wind-driven vortices, and in particular the submesoscale variability of the associated vertical circulation. The latter is mainly linked to ageostrophic motion, and cannot be captured by simpler models. My findings on the structure of the eddy-induced vertical velocity field may indeed rationalize the observed intermittency of the biological response to the presence of eddies in the Sargasso Sea (Sweeney *et al.*, 2003) and the submesoscale pattern of extraordinarily intense and sustained plankton blooms observed in mode-water eddies near Bermuda (McGillicuddy *et al.*, 2007). In general, these results provide a basis for understanding the physics of wind-forced open-ocean vortices that will, I believe, be useful for future studies of the role of coherent eddies in the marine ecosystem in a fully three-dimensional framework.

Acknowledgements

I would fist and foremost like to thank my advisors, Antonello Provenzale and Annalisa Bracco. I have gained greatly from their profound knowledge, insight and intuition in fluid dynamics. Throughout my graduate studies, they indicated the right directions and encouraged me along the way, showing remarkable patience, for this I am very grateful.

Moreover, Annalisa, Antonello, and Claudia Pasquero supplied me with numerical codes of 2D turbulence and plankton dynamics upon which the first part of the thesis' work is based.

I would also like to thank my reviewer, Jeff Weiss for his helpful comments and suggestions upon reading this manuscript.

My gratitude also goes to the staff of the Instituto di Ricerca dell'Atmosfera e del Clima, Centro Nazionale di Ricerca in Torino who have provided a wonderful and enjoyable environment for graduate work.

I gratefully acknowledge support of the Doctoral Fellowship of the "Progetto Lagrange", Fondazione CRT, Torino.

Finally, to my Mother, my Father and Sister for unrelenting warmth and assistance.

Contents

Summary I

Acknowledgements II

1 Introduction **1**
1.1 Mesoscale flows and open-ocean vortices . . . 1
1.2 Three-dimensional view of open-ocean eddies: A motivation . . . 1
1.3 Mesoscale eddies and the marine ecosystem . . . 3
1.4 Outline of the work . . . 5

2 Mesoscale vortices in quasigeostrophic and shallow-water approximations **7**
2.1 Navier-Stokes equations . . . 7
2.2 The scales of the problem . . . 8
2.3 f-plane approximation . . . 8
2.4 Boussinesq approximation and incompressibility . . . 8
2.5 Balanced flows . . . 9
2.6 Hierarchy of models for geophysical vortices . . . 10
2.6.1 Barotropic turbulence . . . 10
2.6.2 Generalized quasigeostrophic (reduced-gravity) model . . . 11
2.6.3 Three-dimensional quasigeostrophic turbulence for a stratified fluid . . . 12
2.6.4 Shallow water equations . . . 13

3 Eddies and marine ecosystem: a lesson from quasigeostrophic turbulence **14**
3.1 Plankton and mesoscale turbulence . . . 14
3.2 Limit cycles in plankton dynamics . . . 14
3.3 Ecosystem model and turbulent advection . . . 15
3.4 Limit cycles disguised . . . 18

4 Primitive Equations: Formulation and the problem of the vertical velocity **22**
4.1 Introduction . . . 22
4.2 Formulation . . . 22
4.3 Vorticity dynamics in Primitive Equations . . . 24
4.4 Vertical velocity problem . . . 25

5 Primitive Equations: Numerical methods **27**
5.1 Introduction . . . 27
5.2 Spatial discretization . . . 28
5.2.1 Vertical grid . . . 28
5.2.2 Horizontal Grid . . . 30

5.3 Equation of state . . . 31
5.4 Time discretization . . . 31
5.5 Advection . . . 33
5.6 Horizontal diffusion . . . 33
5.7 Vertical diffusion . . . 34
5.8 Parallelization and data format . . . 35
5.9 Configuration of the numerical model . . . 35
5.9.1 Wind-forced vortices . . . 36
5.9.2 Freely-decaying version . . . 37
5.9.3 Vertical resolution and the mixed layer . . . 37

6 Results **39**
6.1 System evolution and general description . . . 39
6.1.1 Flow evolution . . . 39
6.1.2 General properties of statistically-stationary flow . . . 41
6.1.3 Anticyclonic vortices . . . 41
6.1.4 Quasigeostrophic eddies and ageostrophic effects . . . 47
6.2 Horizontal circulation from an Eulerian viewpoint . . . 51
6.2.1 Flow Topology . . . 51
6.2.2 Wavenumber spectra . . . 53
6.2.3 Velocity distributions . . . 54
6.3 Horizontal transport from a Lagrangian perspective . . . 57
6.3.1 Introduction . . . 57
6.3.2 Lagrangian autocorrelation time . . . 58
6.3.3 Absolute dispersion . . . 59
6.3.4 Relative dispersion . . . 61
6.4 Vertical velocity . . . 63
6.4.1 Introduction . . . 63
6.4.2 Vertical velocity field in the presence of vortices . . . 64
6.4.3 Vertical velocity dynamics . . . 68
6.4.4 Lagrangian view of vertical motion . . . 71
6.5 Sensitivity study: mixed layer and vertical resolution . . . 74
6.5.1 Mixed layer . . . 75
6.5.2 Vertical resolution . . . 78
6.5.3 The problem of mixing . . . 80

7 Discussion **82**
7.1 Mesoscale eddies and marine ecosystem behavior . . . 82
7.2 Three-dimensional dynamics of open-ocean vortices . . . 83
7.2.1 Problem setup . . . 83
7.2.2 General properties of simulated flow . . . 83
7.2.3 Horizontal dynamics and transport of primitive-equation eddies . . . 84
7.2.4 Vertical velocity . . . 85
7.2.5 Numerical issues . . . 86

7.3 Conclusions 87

A-1 Appendix **101**

A-1 Time-stepping technique 101

A-1 .1 Barotropic time stepping 101

A-1 .2 Barotropic/baroclinic mode coupling 102

A-1 .3 Baroclinic time stepping 103

Chapter 1

Introduction

1.1 Mesoscale flows and open-ocean vortices

The dynamics of the ocean is strongly influenced by planetary rotation and stable vertical density stratification which make the flows strongly anisotropic, favoring movements on the local horizontal plane and inhibiting vertical fluid motions. A remarkable property of remotely-sensed surface ocean is the ubiquity of mesoscale (10-500km) and submesoscale (1-10km) turbulent, energetic flow structures: frontal jets, filaments and eddies. Frontal jets are localized features associated with zones of strong horizontal density gradients (fronts) and are subject to baroclinic instability leading to their meandering. Filaments are elongated regions of high levels of vorticity, the curl of velocity, emerging whenever the turbulent energy cascade from meso- towards smaller scales takes place. *Eddies*, on the other hand, are *coherent vortices*, rotating flow structures that can be defined as approximately axisymmetrical concentrations of vorticity, whose lifetime (several weeks or months) is much larger than their eddy-turnover time and are capable of travelling over large distances. The goal of this study is to investigate the dynamics of ocean eddies.

Current understanding of the origin and emergence of ocean eddies points towards several processes. Vortices form primarily along the baroclinically-unstable meanders of boundary currents and jets (Beckmann *et al.*, 1994; Stammer, 1997). Examples include the famous warm-core "rings" of the the Gulf Stream (McWilliams and Weiss, 1994), Kuroshio's "rings" near the eastern coast of Japan (Rabinovich *et al.*, 2002), eddies in the Agulhas Current near South Africa (Penven *et al.*, 2001), the Algerian Current eddies (Millot and Taupier-Letage, 2005), and vortices in the Beaufort Sea (Spall *et al.*, 2007). Horizontal shear instability is believed to generate submesoscale spiral eddies scattered in the Atlantic and Pacific (Munk *et al.*, 2000). The interaction of flow with the topography has local importance (Bracco and Pedlosky, 2003; Serra *et al.*, 2005) and atmospheric forcing seems to be the major energy source of surface eddies in mid-ocean regions far from strong currents (Muller and Frankignoul, 1981; Stammer, 1997). There are also subsurface vortices at various depths of the ocean. The most famous ones are the so-called Meddies, formed by warm salty Mediterranean water overflowing into the Atlantic by the Strait of Gibraltar (Tokos and Rossby, 1991) and small Arctic vortices originating under sea ice during freezing and melting events (Chao and Shaw, 1996).

1.2 Three-dimensional view of open-ocean eddies: A motivation

The fact that till recently eddies have escaped full recognition is due to their spatio-temporal intermittency which make them elusive to ship-bore measurements. Resolving the mesoscale eddy field synoptically is only practical with remote sensing (satellite images and aircraft photographs), which sample solely the ocean surface (Fig. 1.1), and with Lagrangian drifters. The three-dimensional structure of the underlying flow is little known which makes the progress

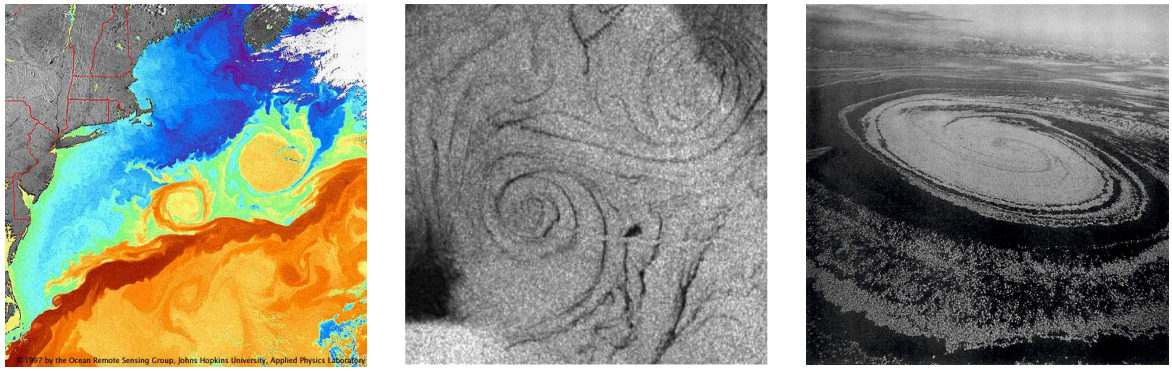

Figure 1.1: Left: Eddies off the East Coast visible in Advanced Very High Resolution Radiometer (AVHRR) satellite image of sea surface temperature field. Blue and red colors correspond to cold and warm waters, respectively. From Ocean Remote Sensing Group, John Hopkins University, 1997. Middle: ERS-2 Synthetic Aperture Radar (SAR) image of two eddies off Sicily (image size 15 x 13 km) observed on September 19, 1993. Vortices are marked by varying radar backscatter intensity due to their effect on the distribution of natural surfactants (surface films). From Ivanov and Ginzburg (2002). Right: A photograph of ice-ocean eddy in the Okhotsk Sea taken on January 12, 1987. The eddy is about 20 km in diameter and is marked by belts of ice floats. From Wakatsuchi and Ohshima (1990).

in interpreting these features rather slow. Given the observational difficulties, one relies on numerical methods. In past years the dynamics and transport properties of mesoscale ocean vortices has been exhaustively studied in the framework of barotropic (2D), quasigeostrophic (QG, e.g. McWilliams, 1984, 1990; Provenzale, 1999; Bracco *et al.*, 2004), or shallow-water (SW) turbulence (Polvani *et al.*, 1994; Graves *et al.*, 2006). Many works focused on the horizontal advection by these structures: Coherent eddies are very efficient in trapping fluid in their cores and transporting it over large distances, preventing mixing with the surrounding water (Elhmaidi *et al.*, 1993; Provenzale, 1999). This is likely one of the main mechanisms producing anomalies in physical and chemical fields evident in space-born images (Fig. 1.1). Much less is known about the vertical eddy transport of momentum and heat. This comes from the fact that barotropic, quasigeostrophic and shallow-water approximations fail to capture local three-dimensional ageostrophic effects contributing to the complex structure of the vertical velocity field associated with vortices. It seems dubious that such models fully explain how the vortices can impact comunication between ocean surface and deep layers.

Still, three-dimensional effects of open-ocean vortices need to be adequately parameterized in ocean components of climate models that use coarse resolution and does not resolve mesoscale flows (Killworth, 1998; Griffies *et al.*, 2000). Although various parameterizations of eddy transport have been proposed (Gent and McWilliams, 1995; Visbeck *et al.*, 1997; Pasquero *et al.*, 2001), it has proved difficult to accomplish this satisfactorily as the understanding of the physics of ocean vortices and their transport properties is far from complete.

1.3 Mesoscale eddies and the marine ecosystem

Owing to their transport properties, eddies impact the ocean biogeochemistry and the marine ecosystem. The *marine ecosystem* results from biological, chemical and physical processes entangled in complicated interactions. The physical component of this system create the conditions for many biochemical processes, which cannot be understood in isolation. The key biological ingredient of the marine ecosystem are tiny and passively carried organisms called *plankton*, and the plants belonging to this group, *phytoplankton*, form the base of numerous intricate food chains. In the process of photosynthesis these organisms convert inorganic compounds, carbon dioxide and water, into carbohydrates; the amount of organic matter produced in this way, the *primary production*, feeds the consumer components of a food chain: zooplankton, fish, wales, birds. The energy needed for the photosynthesis comes from solar energy absorbed by pigments, chlorophyll and carotenoides present in phytoplankton. In addition to light, phytoplankton grow on *nutrients*, certain chemical elements like nitrogen, phosphorus and iron, essential components of their metabolism. The sun's energy that reaches the surface waters is absorbed as it passes downward, decreasing exponentially with depth. The phytoplankton is therefore found in the sunlit layer of the ocean, *the euphotic zone*, typically the first 50-150m from the surface. As a consequence of biological activity, the euphotic zone becomes depleted of nutrients. Decomposition of organisms that sink and decay, hence the regeneration of nutrients, tends to take place in deep water or on the sea floor. In consequence, concentrations of nutrients typically increase sharply with depth. Thus, water movement is needed to bring those nutrients back up into the euphotic zone, or alternatively advect them horizontally from more fertile areas for use by the primary producers (Mann and Lazier, 1996).

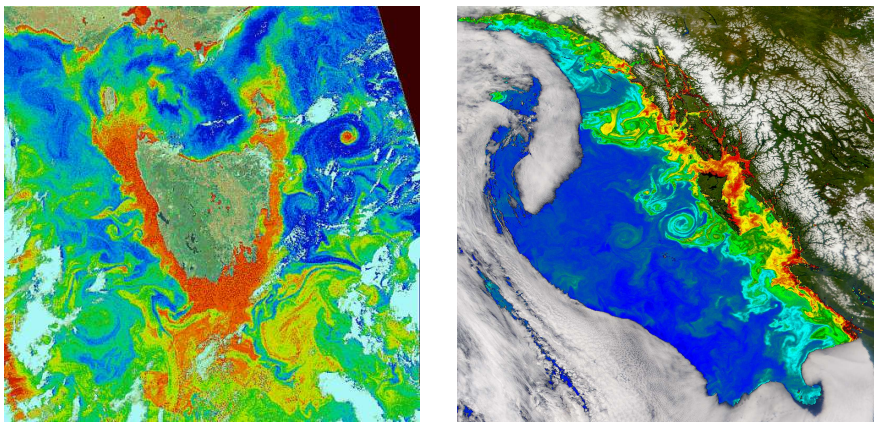

Figure 1.2: Satellite images of chlorophyll-a (phytoplankton pigment). Blue and red colors correspond to low and high concentrations of chlorophyll respectively, and inhomogeneities in its distribution reveal the presence of approximately axisymmteric eddies, meandering fronts and elongated thin filaments. Left: the waters off the island of Tasmania as seen by Coastal Zone Color Scanner (CZCS) on November 27, 1981 (http://daac.gsfc.nasa.gov/oceancolor/scifocus/). Right: the waters off the Queen Charlotte Island on June 13, 2002 (SeaWiFS Project, NASA/Goddard Space Flight Center, and ORBIMAGE, http://earthobservatory.nasa.gov).

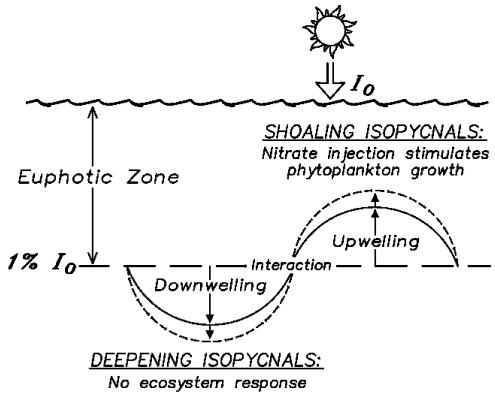

Figure 1.3: A schematic representation of the "eddy-pumping" mechanism. The solid line depicts the vertical deflection of an individual isopycnal caused by the presence of a anticyclonic eddy (left) and an cyclonic eddy (right). The dashed line indicates how the isopycnal might be subsequently perturbed by interaction of the two eddies. I_o represents incident solar radiation at the surface, and the level at which $I = 0.01\, I_o$ defines the base of the euphotic zone. From McGillicuddy *et al.* (1998).

Phytoplankton, apart from making the largest contribution to primary production in the oceans, constitute a vital component of the carbon cycle: They participate in oceanic uptake of atmospheric carbon dioxide and produce chemical compounds that ultimately influence the concentrations of particular atmospheric gases and aerosols (Bigg, 2003, chpt.4). Hence, the distribution and production of plankton are active parameters in the ocean-atmosphere system and they seem to be strongly influenced by the presence of mesoscale and submesoscale flows, including eddies. This is reflected in the distribution of chlorophyll, a proxy for the primary productivity in satellite images (Powell and Okubo, 1994; Srokosz, 2000; McGillicuddy *et al.*, 1997; Batten and Crawford, 2005) with examples shown in Figure 1.2. This finding has stimulated much interest in relating biological patchiness to either horizontal or vertical eddy transport.

Horizontal advection of biochemical fields by a mesoscale vortex field has been widely studied in the context of 2D turbulence. This simple, though relevant, formulation offers a relatively computationally inexpensive alternative to fully-three dimensional circulation models coupled to multiple-variable biochemical modules. It has been employed to investigate the properties of plankton patchiness (Abraham, 1998) and the details of the physical-biological interactions at the mesoscale, where high resolution is needed to resolve the details of the stirring and mixing processes (Martin *et al.*, 2002; Pasquero *et al.*, 2004), to study the effect of ocean eddies on the coexistence of competing plankton species (Bracco *et al.*, 2000a) and to assess the impact of the spatial-temporal variability of nutrient input on primary productivity (Pasquero *et al.*, 2005).

In the open ocean, far from boundary currents, large-scale upwelling regions and coastal waters fertilized by the river run-off, the persistence of a phytoplankton community depends mainly on the vertical transport of nutrients from deeper layers to the surface zone (Mann and Lazier, 1996; Gargett and Marra, 2002; Williams and Follows, 2003). In these areas, strong

local upwelling events inject nutrients to surface waters, driving phytoplankton production and their patchy distribution evident in satellite images (Fig. 1.2), but the physical mechanisms for these injection processes need yet to be specified. There is an observational evidence that eddies act to pump nutrients to the euphotic zone (McGillicuddy *et al.*, 1998; Sweeney *et al.*, 2003; Batten and Crawford, 2005; McGillicuddy *et al.*, 2007) as well as enhance the export of particulate organic carbon (POC) into deep layers, thus its sequestration in the sea bed (Siegel *et al.*, 1990; Sweeney *et al.*, 2003; Benitez-Nelson *et al.*, 2007). An explanation for that is based on the eddy-pumping paradigm, as summarized in Figure 1.3: a deflection of isopycnals (density surfaces) relative to the sunlit layers (euphotic zone) associated with the passage of a geostrophically-balanced eddy (Falkowski *et al.*, 1991; McGillicuddy *et al.*, 1998; Flierl and McGillicuddy, 2002; Sweeney *et al.*, 2003). However, a basin-wide estimate for the eddy pumping fluxes (Oschlies and Garcon, 1998; Martin and Pondaven, 2003) suggests that eddies, alone, cannot provide the nutrient flux required to sustain the observed levels of productivity in the nutrient-depleted open ocean. This in turn triggered a series of primitive-equation (PE) modelling studies focused on mesoscale ocean fronts and associated submesoscale motions, another potential source of intense vertical circulation (Spall and Richards, 2000; Mahadevan and Archer, 2001; Levy *et al.*, 2001b; Martin *et al.*, 2001; Mahadevan and Tandon, 2006). These works report on vertical velocities that can be one order of magnitude stronger than in large-scale upwelling areas, leading to an intensification of primary production.

A detailed investigation of the three-dimensional dynamics of open-ocean eddies, of the associated vertical circulation and of their potential role in marine ecosystem is still lacking.This thesis is devoted to such an exploration. I will address the problem with primitive-equation numerical modelling in a configuration that is the closest I could find to the case of forced-dissipated 2D or QG turbulence, with the aim of highlighting similarities and differences between those simpler models and the PE setting. In this way I will try to provide a base for understanding of the physics of wind-forced vortices that will, I believe, be useful for futher studies of biophysical interactions in a fully three-dimensional framework.

1.4 Outline of the work

The work begins with the introduction of necessary theoretical notions and review of state-of-the-art in modelling mesoscale vortices (Chapter 2). Then, in Chapter 3, I present an example of how intricate can be the interplay between a vortex-dominated 2D flow and a coupled biochemical model, leading to the misinterpretation of the behavior of the latter in the Eulerian time series with respect to Lagrangian measurements (results recently published in Koszalka *et al.*, 2007a).

In the remaining part of the work I intend to develop an insight into the dynamics of ocean eddies by a study based on a three-dimensional primitive-equation model. The equations are described in Chapter 4, and the numerical methods used are presented in Chapter 5. Results follow in Chapter 6. I focus on open-ocean eddies that evolve far from strong boundary currents, in a situation where wind is believed to be the main source for coherent structures (Muller and Frankignoul, 1981; Stammer, 1997). I have opted for using an idealized setup rather than modelling a particular oceanic region: Such formulation of the problem allows to isolate the dynamics and effects of the vortices themselves while it is also relatively close to

the case of forced-dissipated QG turbulence to facilitate comparative studies. I characterize the simulated flows showing that:

- The surface-intensified circulation evolving under the action of narrow-band wind-stress forcing, and in the regime of small Rossby deformation radius, is predominantly horizontal, characterized by small average Rossby number and dominated by coherent anticyclonic vortices.
- In terms of Eulerian and Lagrangian notions traditionally employed in the quasigeostrophic framework (wavenumber spectra, velocity p.d.f.s, dispersion measures), the horizontal motions have a spatial structure and transport properties similar to that of 2D and QG turbulence. The differences include the presence of a free-surface and a non-zero divergence leading to anticyclone dominance (effects captured by the shallow-water approximation) as well as nonlinear interaction of vortices with wind-generated circulation.
- Vertical motions related to the presence of vortices, vortex Rossby waves, their interactions with Ekman circulation and internal waves are very intense (one order stronger than in the large-scale, highly-productive upwelling regions), have non-Gaussian distributions and a complex spatial structure not resolved by QG and SW approximations.
- These strong vertical velocities induce large particle excursions with important consequences on nutrient transport from deeper layers to the surface and results in an enhancement of primary production, as well as export of organic matter into the sea bed.

These results, part of which have recently been discussed by Koszalka *et al.* (2007b), provide a framework for further studies of the role of eddies in the marine ecosystem. Concluding remarks are given in Chapter 7.

Chapter 2

Mesoscale vortices in quasigeostrophic and shallow-water approximations

Starting from the Navier-Stokes equations, this chapter reviews and derive the approximations often adopted to investigate the flow motion in highly stratified and rotating environments, where vertical velocities are much smaller than horizontal ones and can be, at first order, neglected. In particular, I focus on 2d barotropic turbulence (used in Chapter 3 to study biophysical interactions), quasi-geostrophic turbulence and shallow-water models. The material contained in this chapter can be found in classical books on fluid dynamics (e.g., Vallis, 2006), but serves to give notions and definitions used in the following of this thesis.

2.1 Navier-Stokes equations

In its most generic form, ocean flow dynamics is described by an adequate form of the Navier-Stokes equations: conservation of mass, or continuity equation:

$$\frac{D\rho}{Dt} + \rho\nabla\cdot\mathbf{u} = 0, \tag{2.1}$$

conservation of momentum:

$$\frac{D\mathbf{u}}{Dt} + 2\boldsymbol{\Omega}\times\mathbf{u} = -\frac{1}{\rho}\nabla p - \nabla\phi + D_U + F_U, \tag{2.2}$$

evolution of temperature and salinity:

$$\frac{DT}{Dt} = \frac{\alpha_T T}{\rho C_P}\frac{Dp}{Dt} + D_T + F_T, \quad \frac{DS}{Dt} = D_S + F_S, \tag{2.3}$$

and the equation of state for seawater:

$$\rho = R(T, S, p). \tag{2.4}$$

The motion occurs on a spherical planet, so the Cartesian reference frame (x, y, z) is defined such that the variable x refers to longitudinal variations, y varies with latitude and z is reversely aligned with the gravity force. The components of the velocity vector $\mathbf{u}=(u, v, w)$ are parallel to the three frame directions respectively and any spatial variability is quantified by the gradient operator $\nabla=\partial_x + \partial_y + \partial_z$. Temporal evolution is described by $D/Dt = \partial/\partial t + \mathbf{u}\nabla$, the total advective derivative. The momentum equation is formulated in a coordinate frame rotating with the Earth at angular velocity $\boldsymbol{\Omega} = \Omega\,\mathbf{k}$ where Ω is the rotation frequency of the Earth and $\mathbf{k}$ is the unit vector in the local vertical direction. This gives rise to the (apparent) Coriolis force, the second term in (2.2). Gravity enters the forces' balance by spatial variations in geopotential $\phi = gz$ where g is the gravitational constant. The tracer fields relevant for ocean thermodynamics are temperature T, salinity S and pressure p needed to calculate the fluid

density, ρ. α_T is the coefficient of thermal expansion and C_P is the heat capacity at constant pressure. Typically, density increases with depth, leading to a stable *stratification* and resulting in the inhibition of motions parallel to the local direction of gravity. Finally, $F_{U,T,S}$ and $D_{U,T,S}$ represent non-conservative forcing and dissipation that parameterize unresolved processes and small-scale turbulence (Pedlosky, 1987; Salmon, 1998).

2.2 The scales of the problem

This work deals with open-ocean vortices. Accordingly, relevant horizontal scales are the so-called mesoscales (10-500km) and submesoscales (1-10km). In addition, since I am investigating wind-forced, surface-intensified flows, I consider only the upper 1000m of the water column. Such a geometry allows to make certain approximations that simplify the dynamical problem.

2.3 f-plane approximation

The Coriolis force arising from the Earth's rotation is traditionally described by the Coriolis parameter $f \equiv 2\Omega \sin\theta$ where θ is the latitude. At the first order, its dependence on latitude (differential rotation) enters as a linear correction $f = f_o + \beta y$, $\beta = 2\Omega \cos\theta_o / R_E$, where R_E is the radius of the Earth and θ_o is a reference latitude. This so called β-plane approximation is adequate for large-scale currents spanning entire basins. However, on meso- and submesoscale scales, the curvature of the Earth can often be neglected; therefore this work adopts the f-plane approximation where β is set to zero and f equals its reference value f_o (Pedlosky, 1987).

2.4 Boussinesq approximation and incompressibility

The ocean is typically stably stratified. Moreover, the density of seawater is never too far from 1000 $kg\,m^{-3}$. Thus, the density field can be decomposed into a constant part ρ_o, a stratification part $\bar{\rho}(z)$, and a residual $\rho'(x, y, z, t)$:

$$\rho(x, y, z, t) = \rho_o + \bar{\rho}(z) + \rho'(x, y, z, t). \tag{2.5}$$

For the seawater typically $\rho_o \approx 1025$ $kg\,m^{-3}$, $\bar{\rho} \approx 30$ $kg\,m^{-3}$ and $\rho' \approx 3$ $kg\,m^{-3}$, so one can safely assume that $|\rho'|, |\bar{\rho}(z)| \ll \rho_o$. This is the basis for the *Boussinesq approximation*, which replaces the exact density with the constant part ρ_o in many terms of the equations of motion (Salmon, 1998). The first target is the continuity equation (2.1) which simplifies to:

$$\nabla \cdot \mathbf{u} = \partial_x u + \partial_y v + \partial_z w = 0, \tag{2.6}$$

which implies that oceanic flows can be considered *incompressible*.

Futher simplification comes from the fact that on the right-hand-side of the temperature equation (2.3), the Dp/Dt term can be neglected for typical oceanic values $T \approx 275$ K, $C_P \approx 1$ $cal\,gm^{-1}\,deg^{-1}$ and $\alpha_T \approx 2x10^{-4}$ deg^{-1}, provided that $\delta T \gg 1.3 \times 10^{-3} \delta p$ measured in atmospheres. This is not satisfied in the deep ocean (below 3000m or so) where the most significant temperature changes are sometimes caused by pressure changes. However, at the depths considered here, this approximation is justified. Physically, it means that sound waves are eliminated from the dynamical problem (Salmon, 1998).

2.5 Balanced flows

Large and mesoscale motion in the oceans can be approximately modelled as a *quasi-twodimensional* (Q2D) flow, i.e. taking place mainly on a local horizontal plane perpendicular to the local direction of gravity. The suppression of vertical motions occurs for geometrical reasons, as well as owing to the balance between the two dominating forces: the Coriolis force and the buoyancy.

The geometry of oceanic flows is usually such that the horizontal length scale L of a motion with characteristic velocity scale U is large compared to the vertical height scale H. That is, the *aspect ratio* of the motion,

$$\Upsilon = \frac{H}{L}, \tag{2.7}$$

is a small number. This geometrical argument by simple scaling in (2.6) implies $w \ll (u, v)$. Consequently, the vertical momentum equation in (2.2) reduces to:

$$\frac{\partial p}{\partial z} = -g\rho \tag{2.8}$$

which represents *hydrostatic balance* in the vertical direction between the vertical pressure gradient and the buoyancy force. That is, the pressure difference between any two points on the same vertical line depends only on the weight of the fluid between those points, as if the fluid were at rest, though in fact it is in motion (Pedlosky, 1987). The Coriolis force becomes significant in (2.2) compared to the advective terms (inertial force) whenever the Rossby number:

$$R_o = \frac{U}{fL} \tag{2.9}$$

is small. The effect of stratification is captured by the internal Froude number, defined as the square root of the ratio between inertia and buoyancy:

$$Fr = \frac{U}{NH}, \tag{2.10}$$

where

$$N^2(z) = -\frac{g}{\rho}\frac{\partial \rho}{\partial z} \tag{2.11}$$

is the squared ambient Brunt-Väisäla (buoyancy) frequency, a measure of the strength of stratification.

In the limit (Υ, Ro, Fr) $\to 0$ the flows are governed by (2.8) and by the balance between the Coriolis force and the pressure gradient force, in the so-called *geostrophic balance* :

$$-fv = -\frac{1}{\rho_o}\frac{\partial p}{\partial x}, \quad +fu = -\frac{1}{\rho_o}\frac{\partial p}{\partial y}. \tag{2.12}$$

For vertically-homogeneous, *barotropic flows*, the variables in (2.12) are functions of (x, y) only. When u, v are functions of depth (*baroclinic flows*), cross-differentiation of (2.12) under the Boussinesq approximation (2.5) yields:

$$\left(\frac{\partial u}{\partial z}, \frac{\partial v}{\partial z}\right) = \frac{g}{\rho_o f_o}\left(\frac{\partial \rho}{\partial y}, -\frac{\partial \rho}{\partial x}\right) \tag{2.13}$$

This is so-called *thermal wind* relation by which the vertical shear of horizontal velocity is balanced by horizontal gradients of density (Salmon, 1998).

Relations (2.8), (2.12) and (2.13) represent diagnostic balances of forces that costrain the fluid acceleration and result in quasi-stationary dynamics of basin-scale currents. Also ocean eddies can be detected from space as sea-height anomalies because in a first approximation they are geostrophically balanced. If fluid motion in such a vortex has the same sense of rotation as the Earth, it is called *cyclonic*. According to (2.12) it is characterized by a low pressure at its center, a dented free-surface and (if stratified) doming isopycnals. The opposite is true for *anticyclonic* eddies. In the Northern Hemisphere, an anticyclonic vortex will rotate clockwise and a cyclone counterclockwise. However, if the relative vorticity of an eddy approaches f ($Ro \approx 1$), the inertial force takes over; the balance becomes *cyclostrophic* whereby vortices are always low-pressure anomalies. Cores of strong ocean vortices are sometimes observed to be cyclostrophically balanced (Tokos and Rossby, 1991).

2.6 Hierarchy of models for geophysical vortices

The geostrophic balance equations cannot be used to make predictions of the ocean dynamics. When the system is allowed to evolve in time but it stays in the asymptotic regime (Υ, Ro, Fr) $\ll 1$, it is said to be quasi-geostrophic (QG) (Pedlosky, 1987). In this formulation, the flow is horizontally non-divergent. Consequently, its time evolution can be recast in an equation for a sole quantity related to the curl of velocity. A hierarchy of models built upon the QG approximation and their generalizations have proved to be useful for describing the emergence and evolution of energetic mesoscale coherent structures.

2.6.1 Barotropic turbulence

The simplest model is 2D barotropic turbulence (Salmon, 1998; Provenzale, 1999):

$$\frac{Dq}{Dt} = \frac{\partial q}{\partial t} + J(\psi, q) = F + D, \tag{2.14}$$

where $D/Dt = \partial/\partial t + J(\psi, q)$ is the total advective derivative, $J(\psi, q) = \partial_x\psi\partial_y q - \partial_y\psi\partial_x q$ is the Jacobian operator, $\psi = p/f_o\rho_o$ is the geostrophic streamfunction, forcing and dissipation are represented by F and D respectively, and the evolving quantity

$$q = \zeta + f_o + \beta y + \Delta h(x, y) - \psi/\lambda^2 \tag{2.15}$$

is potential vorticity. The first term in the definition (2.15) is the relative vorticity $\zeta = \nabla^2\psi$. Thus, the two-dimensional, non-divergent velocity field $\mathbf{u} = (u, v)$ is given by $u = -\partial_y\psi$ and $v = \partial_x\psi$. The second and third term represent the (latitude-dependent) Coriolis parameter and the fourth one accounts for variable bottom. The last term refers to the free-surface effect, which encompasses the deformation of the upper boundary due to pressure changes by (2.12). It is written in terms of dimensionless quantity $\lambda = \lambda_o/L$, where

$$\lambda_o = \frac{\sqrt{gH}}{f_o} \tag{2.16}$$

is the *external Rossby deformation radius*. If the bottom is flat and the domain is sufficiently small compared to λ_o and R_E, potential vorticity (2.15) can be approximated by relative

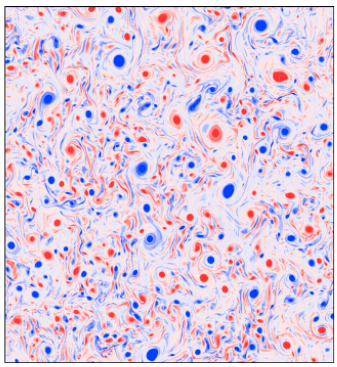

Figure 2.1: A snapshot of the relative vorticity field in 2D forced barotropic turbulence. From Pasquero *et al.* (2001).

vorticity. By filtering out fast gravity wave motions, (2.14) – (2.15) allows fast numerical computation of evolution equation for large-scale, nearly geostrophic modes of oceanic flows. The system (2.15) has been widely studied both experimentally and numerically and its properties can be summarized as follows:

- When the right-hand side of Equation (2.14) vanishes, two quadratic invariants: total kinetic energy, $E = 1/2L^2 \int (\nabla\psi)^2 \, dxdy$, and total enstrophy, $Z = 1/2L^2 \int (\nabla^2\psi)^2 \, dxdy$ are simultaneously conserved. This leads to a direct (from large to small scales) cascade of enstrophy, and an inverse (from small to large scales) cascade of energy (Kraichnan and Montgomery, 1980); the term responsible for the energy and enstrophy transfers in (2.14) is the nonlinear Jacobian term.

- Spectral transfers are accompanied by *self-organization* of the flow: An initially random vorticity field evolves spontaneously into an ensemble of intermittently distributed vortices and high-vorticity filaments immensed in a random, low-energy background turbulent field (Fig. 2.1). The presence of coherent structures is in marked contrast to the concept of turbulence as random formless flow (McWilliams, 1984; Babiano *et al.*, 1987).

- Coherent eddies play a major role in determining the mixing and dispersion properties of the flow (Provenzale, 1999). Vortices trap fluid particles for long times preventing them to mix with the surrounding fluid, and the global transport properties of an eddy field require parameterizations that explicitly take into account the presence of vortices (Pasquero *et al.*, 2001).

2.6.2 Generalized quasigeostrophic (reduced-gravity) model

The model of barotropic turbulence assumes vertical homogeneity. A formalism one step closer to more realistic flows, which however still retain the simplicity of (2.15), is the Generalized QG (reduced-gravity) model (Davey and Killworth, 1984; Cushman-Roisin and Tang, 1990; Salmon, 1998). One begins with considering a two-layer model where a homogeneous layer of

fluid with depth h_1 and density ρ_1 overlies a much deeper layer of slightly larger density ρ_2 (the extratropical ocean behaves grossly like such a two-layer fluid). By defining the *reduced gravity* $g' = g(\rho_2 - \rho_1)/\rho_2$, the two-layer model might be transformed into a set of equations for the barotropic (depth-averaged) mode and the baroclinic mode $\psi_1 - \psi_2$. There one defines the *internal Rossby radius of deformation*,

$$\lambda_I = \frac{\sqrt{g'H}}{f_o}, \tag{2.17}$$

that substitutes (2.16). This model can be used for studies of flow behavior under different regimes depending on value of (2.17) and varying importance of terms in eq. (2.15), including an asymmetry between cyclonic and anticyclonic vortices in the regime of λ_I smaller than the typical horizontal length of the flow (the free-surface effect due to a nonzero last term in eq. (2.15) with λ_I as the appropriate length scale) and an arrest of the energy cascade at wavenumbers determined by the value of β and λ_I (Cushman-Roisin and Tang, 1990; Larichev and McWilliams, 1991). However, this model is still too simple to properly represent the dynamics of a continuously stratified fluid, like the ocean.

2.6.3 Three-dimensional quasigeostrophic turbulence for a stratified fluid

A more realistic approximation that includes the vertical extent of the fluid and therefore the presence of stratification, variation of horizontal momentum with depth, and allows for baroclinic instability, an important aspect of the ocean dynamics, is the three-dimensional, quasigeostrophic turbulence (3D QG). In 3D QG model, eq. (2.14) governs the evolution of the three-dimensional potential vorticity:

$$q = \nabla^2\psi + \frac{\partial}{\partial z}\frac{f}{N(z)}\frac{\partial\psi}{\partial z}. \tag{2.18}$$

In the case of uniform stratification, N=const., the right-hand side of (2.18) becomes the isotropic Laplacian operator, $q = \nabla^2\psi$, $\nabla^2 = \partial_{xx} + \partial_{yy} + \partial_{z'z'}$. In this sense, the motion is three-dimensional, however the vertical velocities vanish at first order and the flow is non-divergent. A well-known prediction by Charney (1971) states that when the stratification is constant, a 3D QG motion should be isotropic. Similarly to what happens for 2D turbulence, also QG flows display an inverse energy cascade in the inertial range. The Charney's proofs have been shown to be problematic (Herring, 1980; Tung and Welch, 2001), with the two-dimensional structure of the Jacobian operator in (2.14) being indicated as the responsible for the observed anisotropy. Numerical simulations have shown that in 3D periodic domain the flow self-organizes into vortices but the prediction is only approximately verified in the shape of the spectrum, evolution of the vortices, their interactions and stability (McWilliams *et al.*, 1994; McWilliams and Weiss, 1994; von Hardenberg *et al.*, 2000). Nevertheless, baroclinic QG vortices induce transport and mixing properties analogous to their barotropic counterparts (Bracco *et al.*, 2004). In the presence of appropriate boundary conditions, the concept of potential vorticity is useful for describing many aspects of oceanic large-scale circulation: zonal flows, topographic steering, western boundary currents can be explained as the consequence of conservation of (2.18) (Pedlosky, 1987). Still, the flow divergence, neglected in the quasigeostrophic approximation, is important for many oceanic phenomena.

2.6.4 Shallow water equations

Taking a first step beyond quasigeostrophy, one considers incompressible, homogeneous, non-viscous, hydrostatic, rotating fluid with a flat bottom:

$$\frac{D\mathbf{u}_H}{Dt} + f\mathbf{k} \times \mathbf{u}_H = -g\nabla h, \quad \frac{Dh}{Dt} + \nabla \cdot (\mathbf{u}_H h) = 0, \tag{2.19}$$

where $\mathbf{u}_H = (u, v)$ is horizontal fluid velocity and $h = H + \eta$ is the total water depth to which a variable bottom $H(x, y)$ and a deformable free-surface $\eta(x, y, t)$ contribute. This is the shallow water (SW) model. The curl of (2.19) gives a conservation equation for potential vorticity $q = (\zeta + f/H + \eta)$, but now this is not the sole variable characterizing the system because in eq. (2.19) the total depth h evolves simultaneously. Consequently, alongside vortical motions, the model admits inertio-gravitational modes (Poincaré waves) with the frequencies ν given by:

$$\nu^2 = f^2(1 + \lambda_o^2\kappa^2) \tag{2.20}$$

where κ is the two-dimensional wavenumber. In the presence of background rotation, the inertia-gravity waves are dispersive and radiate away from the location of initial disturbance in surface level, leaving behind the slowly changing, geostrophic vortical modes which constitute the steady equilibrium solution. This process is called *geostrophic adjustment* (Gill, 1982). Another type of solution that emerges in (2.19) is given by vortex Rossby waves which typically possess frequency smaller than f, thus their time-scales are sufficiently long to allow the Coriolis force to impact their propagation. In consequence, these wave motions are regarded as largely geostrophically balanced (Montgomery and Lu, 1997; McWilliams *et al.*, 2003). Recent studies in the SW framework have shown how the presence of vortex Rossby waves associated with eddies evolving in a straining flow can lead to dominance of anticyclonic vortices (Graves *et al.*, 2006); a phenomenon parameterized as the "free-surface effect" in the reduced-gravity model (Sect. 2.6.2).

The system (2.19) in its inviscid form still conserves the total energy and (potential) enstrophy (Salmon, 1998). Numerical simulations show that spectral transfers undergo similarly to 2D turbulence leading to the emergence of vortices unless the levels of inertio-gravitational energy are high (Farge and Sadourny, 1989). The non-zero divergence by (2.1) implies non-zero vertical velocity at first order; the latter is however simply linearly dependent on depth and does not participate in advection. The homogeneous SW model provides a useful conceptual framework in geophysical fluid dynamics (Pedlosky, 1987; Vallis, 2006) but it is clearly unsuitable to capture details of evolution of a inhomogeneously stratified oceanic flow, in particular a possibly complex structure of the vertical velocity field that need to be addressed with more realistic formulations.

Chapter 3

Eddies and marine ecosystem: a lesson from quasigeostrophic turbulence

Before investigating the three-dimensional complexity of mesoscale flows, I shall present my contribution to the understanding of the impact of vortices on marine ecosystem dynamics. I will show an example of how the horizontal advection can modify the behavior of ecosystem models due to the presence of coherent structures; namely, how it can disguise limit cycle behavior to the point that it cannot be detected in fixed-point measurements of plankton abundance.

3.1 Plankton and mesoscale turbulence

Spatial heterogeneity, or patchiness, is perhaps the most salient characteristic of plankton populations in the ocean. Remarkably, chlorophyll distributions observed in satellite images bear a signature of the mesoscale eddy field (Srokosz, 2000; McGillicuddy *et al.*, 1997; Batten and Crawford, 2005), with examples shown in Fig. 1.2. The horizontal advection by the vortex field has been proposed to be the main mechanism for these phenomena: As the vortices act as transport barriers, they trap chemical and biological tracers that evolve in isolation from the surroundings thus developing a spatial pattern. The concept of 2D turbulence as a first order approximation to mesoscale oceanic turbulence has widely been used to explain the differing scales of variability seen in biochemical fields (Abraham, 1998; Martin *et al.*, 2002; Pasquero *et al.*, 2004), to study the effect of ocean eddies on the coexistence of competing plankton species (Bracco *et al.*, 2000a) and to assess the role of the spatial-temporal variability of nutrient input on primary productivity (Pasquero *et al.*, 2004, 2005). All these studies focused on advection as an agent providing nutrients, hence stimulating growth of phytoplankton in certain regions more that in others. In a recent work, (Koszalka *et al.*, 2007a), I have shown a different aspect of horizontal eddy transport, namely how it can affect the interpretation of ecosystem model behavior in an Eulerian measurement of plankton abundance.

3.2 Limit cycles in plankton dynamics

Many studies of marine ecosystem dynamics are based on the use of spatially-homogeneous descriptions formalized in terms of coupled ordinary differential equations. These homogeneous models, with standard functional representations of biological processes and for realistic parameter values, display a limit-cycle behavior: self-sustained oscillations of model variables (or equivalently, a closed trajectory in the phase space of the dynamical model) not driven by temporal changes in parameter values but by nonlinear dynamics alone, see e.g. Steele and Henderson (1992); Truscott and Brindley (1994); Fasham (1995); Edwards and Brindley (1996); Ryabchenko *et al.* (1997); Edwards and Brindley (1999); Edwards and Yool (2000); Gibson *et al.* (2005). However, field observations do not support the presence of self-sustained oscillations of plankton concentration, therefore these fluctuations have been considered as an indication of the inadequacy of the mathematical formulations employed in the theoretical models.

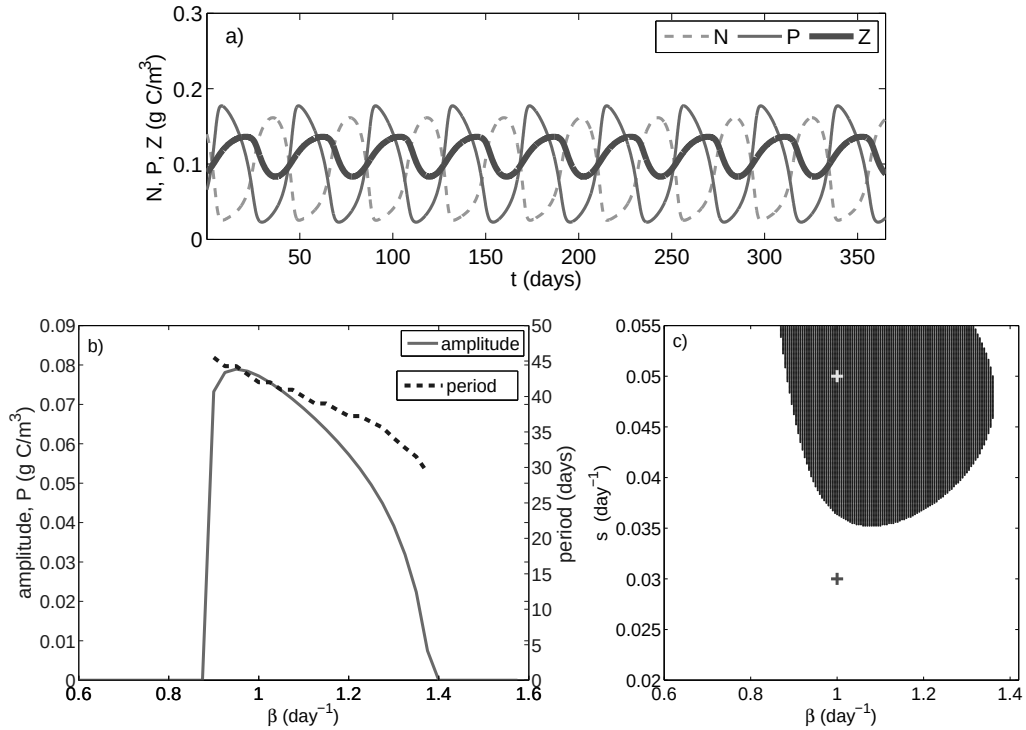

Figure 3.1: (a) N, P and Z time series from the ecosystem model (3.1) for the set of parameter values leading to self-sustained oscillations as given in the text. (b) Amplitude and period of the self-sustained oscillations in phytoplankton concentration as a function of phytoplankton growth-rate, β. All other parameters are as in panel a. (c) Classification of the model solutions as obtained from linear stability analysis. The shaded area indicates the region in parameter space where the system settles on a stable limit cycle, while the white region corresponds to the presence of one stable steady state. The two crosses indicate the parameter values used in the simulations.

On the other hand, plankton dynamics takes place in a turbulent ocean, where mesoscale features such as vortices, fronts and jets advect plankton and nutrient concentrations on space scales of several tens of km and time scales of a few days, comparable with the time scales of biological reactions. Inspired by this problem, I have focused on the effects of advection on limit-cycle dynamics with an aim of quantifying the possibility of detecting self-sustained oscillations in time series of plankton abundance obtained by different sampling techniques.

3.3 Ecosystem model and turbulent advection

Marine ecosystem modelling is typically formalized in terms of coupled deterministic advection-reaction-diffusion (ARD) equations where variables are proxies for continuous concentrations of biochemical fields. In the ARD approach, a homogeneous model parameterizing biochemical processes is coupled to a hydrodynamical module by the advection terms where the tracer fields are passively carried by flow (that is, they do not modify physical water properties) and mix due to gradients in their concentrations between adjacent water parcels (e.g., McGillicuddy, 2001;

Franks, 2002; Pasquero *et al.*, 2004). The biological reactions among the variables in the homogeneous model are described by appropriate mathematical formulas. The functional forms, and the associated parameters, are chosen to most adequately simulate the temporal development of biological production in particular areas of the ocean, mainly those for which good time-series data are available (e.g., Steele and Henderson, 1992; Fasham, 1995). Resolving all the existing plankton species by such a model would make it untreatable, thus the species that play a similar ecological role in the ecosystem are aggregated into "compartments". Abundances in the various compartments become model variables. This work employs one of the simplest dynamical models that describes oceanic plankton dynamics, a standard three-compartment (Nutrient-Phytoplankton-Zooplankton, NPZ) model of the lower trophic levels in the marine ecosystem that displays self-sustained oscillations (Edwards and Yool, 2000). The model equations are:

$$\begin{aligned}
\frac{\partial N}{\partial t} + \mathbf{u}\cdot\nabla N = &\quad s(N_0 - N) - \beta\frac{N}{k+N}P\left(1-\frac{P}{\gamma}\right) + (1-\alpha)\frac{\lambda P^2}{\mu^2+P^2}Z + D_N \\
\frac{\partial P}{\partial t} + \mathbf{u}\cdot\nabla P = &\quad \beta\frac{N}{k+N}P\left(1-\frac{P}{\gamma}\right) - \frac{\lambda P^2}{\mu^2+P^2}Z + D_P \\
\frac{\partial Z}{\partial t} + \mathbf{u}\cdot\nabla Z = &\quad \alpha\frac{\lambda P^2}{\mu^2+P^2}Z - \omega Z^2 + D_Z,
\end{aligned}$$

where t is time in days, N, P, Z are the concentrations of nutrient, phytoplankton and zooplankton averaged over the depth of the subsurface mixed layer and expressed in terms of a common currency (grams of carbon per cubic meter, $g\,C\,m^{-3}$), ∇ is the horizontal gradient, $\mathbf{u}$ is the horizontal velocity field and D_N, D_P, D_Z represent horizontal diffusion of biochemical tracers.

In this model, the consumption of nutrients by phytoplankton and its consequent growth is described by a Holling type II (or Michaelis-Menten) function, $\beta\frac{N}{k+N}P$. Here, the maximum phytoplankton growth rate β is modified assuming that phytoplankton uptake of nutrient saturates and the constant k is a nutrient concentration at which the uptake is half maximum (Nihoul, 1975; Vandermeer and Goldberg, 2003). This term is futher modulated by the logistic growth of phytoplankton, $(1-\frac{P}{\gamma})$, where γ stands for carrying capacity, a saturation of phytoplankton concentration due to reduction in the average light in the mixed layer with increasing phytoplankton population (Steele and Henderson, 1981). This model adopts a Holling type III form for zooplankton grazing, $\alpha\frac{\lambda P^2}{\mu^2+P^2}Z$, where α is zooplankton efficiency in transforming phytoplankton into zooplankton biomass, λ is the maximum zooplankton grazing rate and μ is the half-saturation coefficient for zooplankton grazing (Steele and Henderson, 1981; Vandermeer and Goldberg, 2003). The last term of the first equation represents regeneration processes: Part of the phytoplankton biomass that is not transformed into zooplankton dies and becomes recycled as nutrient in the mixed layer. The quadratic zooplankton mortality, $-\omega Z^2$, assumes that the amount of predators (higher trophic levels unresolved by the model) depends linearly on the amount of the prey (zooplankton) which is eliminated at the rate ω and results in a net biomass loss from the model (Steele and Henderson, 1992). The model employs a relaxation form of the nutrient input, $s(N_0 - N)$, where N_0 is the deep-water nutrient concentration below the mixed layer and s is the vertical exchange rate of water at the base of the mixed layer which provides a simplified representation of turbulent vertical exchanges between the mixed layer and the deeper ocean, and it can be used in a two-dimensional model

to parameterize nutrient input due to unresolved vertical mixing due to eddies, breaking internal waves, wind-induced circulation and other processes (Fasham, 1995). Without advection ($\mathbf{u} = 0$) and for spatially homogeneous conditions, the model (3.1) displays limit cycle behavior in a wide parameter range estimated from observations from the North Atlantic and the North Pacific (Steele and Henderson, 1992; Edwards and Brindley, 1996; Edwards and Yool, 2000). Figure 3.1a shows an example of self-sustained oscillations for the parameter values $N_0 = 0.6$ $g\ C\ m^{-3}$, $s = 0.05$ d^{-1}, $k = 0.03$ $g\ C\ m^{-3}$, $\beta = 1$ d^{-1}, $\gamma = 1$ $g\ C\ m^{-3}$, $\mu = 0.035$ $g\ C\ m^{-3}$, $\alpha = 0.25$, $\omega = 0.25$ $(g\ C)^{-1}\ m^3\ d^{-1}$, and $\lambda = 0.6$ d^{-1}. In this case, the period of the self-sustained oscillations is $T \approx 41$ days. Further details on this particular model are given in Steele and Henderson (1992) and Edwards and Yool (2000). I have considered variations of the phytoplankton growth rate, β, and of the relaxation rate associated with turbulent nutrient input, s. Figure 3.1b shows the amplitude and period of the self-sustained oscillations as a function of β, and Figure 3.1c shows a region of the $\beta - s$ parameter plane where limit-cycle behavior is present.

The horizontal turbulent velocity field is given by eq. (2.14); its properties are described in Sect. 2.6.1. The forcing F is obtained by fixing the energy spectrum at a given forcing wavenumber, k_F. Dissipation is provided by the sum of a hyperviscosity term acting at small scales, $(-1)^{p-1} D_p \nabla^{2p} q$ with $p = 4$, and by large-scale dissipation, $(-1)^{r-1} D_r \nabla^{-2r} q$ with $r = 1$, used to dissipate energy that piles up at small wavenumbers due to the inverse energy cascade (Elhmaidi *et al.*, 1993; Pasquero *et al.*, 2001). Equation (2.14) is integrated using a pseudo-spectral method and a third-order Adams-Bashforth time integration scheme in a doubly-periodic square domain with size $L = 256$ km and spatial resolution $\Delta = 0.5$ km. The forcing scale is fixed at $L/10 = 25.6$ km. The turbulent field is characterized by r.m.s. velocity fluctuation $\sigma_U = 4$ cm/s and a characteristic time, the Eulerian decorrelation time, $T_E = \sum_1^M R(\tau) d\tau$=3.6 day, where the Eulerian velocity autocorrelation function is estimated as $R^E(\tau) = \frac{1}{T} \left\langle \frac{1}{\sigma_U} \sum_{t=0}^{T} \mathbf{u}(t) \cdot \mathbf{u}(t+\tau) dt \right\rangle$ for a time series of length $T = M\tau$. These values are in the appropriate range for mid-ocean conditions. The turbulence flow is evolved to a statistically stationary state prior to its use in the runs with biological tracers. To integrate the dynamics of biological tracers, we adopt the Lagrangian approach described in Pasquero *et al.* (2004) and integrate the motion of 512×512 ecosystem-carrying fluid elements in the two-dimensional turbulent flow described by eq. (2.14). Each parcel represents a given water volume and it is assumed to have homogeneous properties. Owing to the fact that the fluid volumes have a linear size of 0.5 km, we discard mixing of biological tracers between different fluid parcels setting the diffusion terms to zero. The concentration fields of biological tracers are then obtained from the distribution of fluid elements. In the following, the fate of self-sustained oscillations is studied when some of the model parameters (namely, s) are variable in space. The temporal variability of plankton abundance is investigated in time series obtained by either recording the concentrations in a single given fluid parcel (Lagrangian measurement), or the records provided by a "measurement station" at a fixed point in the domain (which is defines a mean over 2×2 grid cells, i.e., a square with side 1 km), corresponding to an Eulerian measurement.

3.4 Limit cycles disguised

In this simple configuration, all model parameters are kept constant in space and time, except for the nutrient input relaxation rate, which is allowed to vary in space. To this end, we assign the value $s = s_f = 0.05\ d^{-1}$ inside a zonal strip of width 128 km and a lower value, $s = s_n = 0.03\ d^{-1}$, in the remaining portion of the domain (Fig. 3.2a). The strip of enhanced vertical exchange rate is placed in the middle of the domain and the integration starts from a homogeneous distribution of the biological tracers. In the case of a homogeneous ecosystem, the value s_n would lead to steady-state behavior, while s_f is in the parameter range of self-sustained oscillations (see figure 3.1c). Figure 3.2b shows one snapshot of the simulated phytoplankton field.

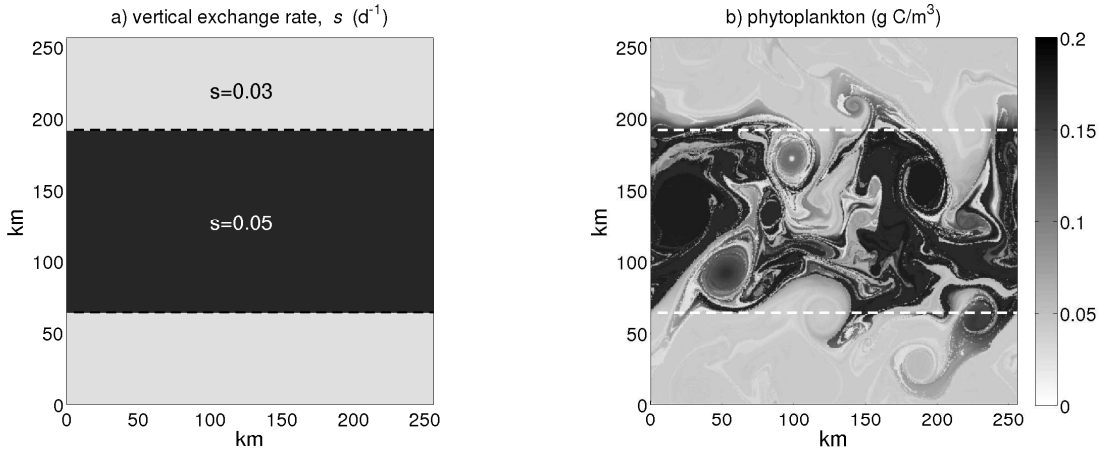

Figure 3.2: (a) Spatial distribution of the vertical exchange rate s. The value of $s = s_n = 0.03\ d^{-1}$ would lead to steady-state behavior in the homogeneous model (3.1) and the value of $s = s_f = 0.05\ d^{-1}$ is in the parameter range of self-sustained oscillations. (b) Snapshot of the phytoplankton concentration after 110 days of integration of model (3.1). Nutrient, phytoplankton and zooplankton are advected by barotropic turbulence, eq.(2.14). The vertical exchange rate is $s = s_f = 0.05\ d^{-1}$ in the central zonal strip with side 128 km and $s = s_n = 0.03\ d^{-1}$ elsewhere. The horizontal dashed lines indicate the edges of the strip. The simulation started from a homogeneous distribution of nutrient and of biological tracers.

Figure 3.3 shows examples of Lagrangian and of Eulerian time series of nutrient, phytoplankton and zooplankton abundances that illustrate the typical effect of advection on limit-cycle behavior. In the case of Lagrangian time series, the repeated passage of the fluid parcel from regions where s is in the range of limit-cycle behavior to regions where the value of s corresponds to a fixed point, and viceversa, leads to a modulation of the amplitude of the oscillations and to the presence of transients from one attractor type to the other. If the transitions back and forth from the stable point to the limit cycle are frequent, the oscillations do not have time to reach the asymptotic amplitude and the system can jump back to the fixed point before a full cycle is completed. For this reason, high fragmentation of upwelling areas (for example, two stripes of width 64 km instead of one strip of 128 km) can significantly challenge the detection of oscillatory behavior.

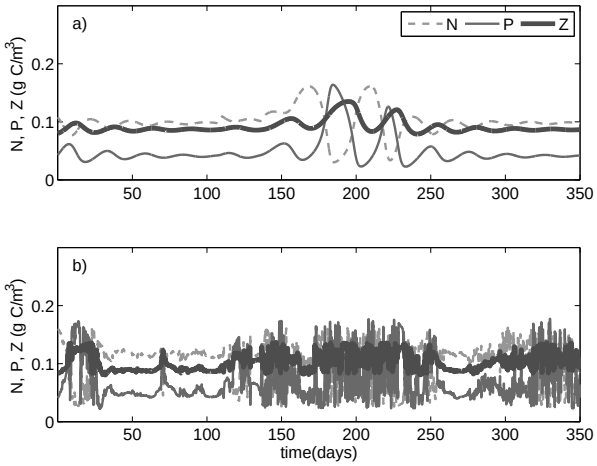

Figure 3.3: Time series of nutrient, phytoplankton and zooplankton from a Lagrangian measurement in an individual fluid parcel moving with the flow (panel a) and from an Eulerian measurement at a fixed position in space at the edge of the strip of enhanced vertical exchange rate (panel b).

In the case of Eulerian measurements, shown in fig.3.3b, one observes a complete obliteration of the self-sustained oscillations. In the course of time, different fluid parcels pass by the measurement site. Even though each particle could have a remnant of self-sustained oscillations, different particles have a different history of alternance between regions with high and low exchange rates and thus reach the limit-cycle behavior with a different phase. As a result, the continuous advection of different parcels recorded at the measurement site, combined with the de-phasing effect due to spatial inhomogeneity completely masks the limit-cycle behavior. Figure 3.4 shows the power spectra of phytoplankton abundance averaged respectively over five Lagrangian trajectories and over five Eulerian time series measured at different positions at the boundary between the two regions (same qualitative results are obtained for different choices of Eulerian measurement positions). While a broad peak at the limit-cycle period is still visible in the power spectrum from the Lagrangian measurements, no evidence of the self-sustained oscillations is present in the Eulerian record.

The results presented here are quite general, and they hold also when other model parameters become space-dependent (e.g., β) and for different versions of the NPZ model. In particular, we repeated the analysis with the model used in Pasquero *et al.* (2005), finding analogous results. Note, also, that it is sufficient a parameter variation of less than a factor of two to mask the limit-cycle behavior in plankton time series. Also, when the parameter is varied such that two limit cycle behaviors with different periods are favored, the findings are analogous as presented above.

The above results have been obtained by assuming spatial variability of one of the control parameters and spatially homogeneous initial conditions. The case with spatially-homogeneous control parameters and inhomogeneous initial conditions leads to a reduction of the amplitude of self-sustained oscillations in Eulerian time series, but not to their complete disappearance. This happens for both random and structured initial conditions, such as an initial distribution

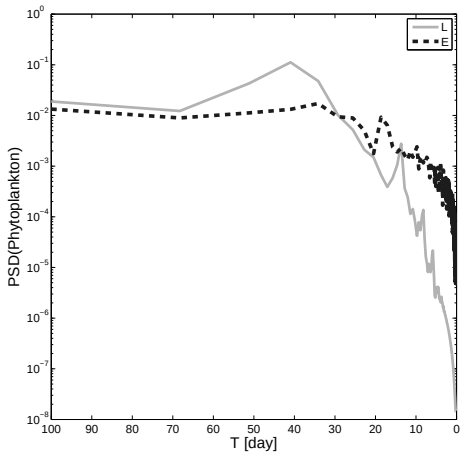

Figure 3.4: Average power spectra of phytoplankton abundance from Lagrangian (solid) and Eulerian (dashed) time series calculated. The Lagrangian spectrum is the average of the spectra computed from five different trajectories and the Eulerian spectrum is the average of the spectra from five different measurement sites located at the edge of the strip with enhanced vertical diffusivity. Qualitatively analogous results are found for different choices of the positions of the Eulerian measurement sites.

of N, P and Z of the form $cos(nx)cos(my)$ with various integer values of m and n. On the other hand, when spatially-structured (random or cos-like) initial conditions are used together with a spatially-inhomogeneous distribution of the control parameters, the smearing out of the limit cycle is emphasized. In this case, limit cycles are completely disguised in Eulerian time series and strongly reduced in Lagrangian data, similarly to what is shown in previous figures. This confirms that the spatial inhomogeneity of the control parameters is the true responsible for the practical undetectability of limit cycles in Eulerian oscillations.

It may be interesting to note that the variations induced in a fluid parcel due to alternance between different regions in space generate a temporal variation of the parameters in the homogeneous ecosystem model inside the fluid parcel itself. Self-sustained oscillations have also been found depressed in the case of a homogeneous ecosystem subject to temporal variation of some of the parameters. If we consider a case with no advection and homogeneous spatial conditions, and assume that the vertical exchange rate s varies periodically in time (mimicking the seasonal variations), we obtain results that are completely analogous to what is observed in Lagrangian time series. Mesoscale advection with both spatial and temporal variability of the model parameters, and/or non-homogeneous initial conditions lead to a similar obliteration of limit-cycle behavior in plankton time series.

In summary, in this study I have shown that the interplay of horizontal advection and of spatial-temporal inhomogeneity can mask the presence of self-sustained oscillations in plankton abundance that can be generated by limit-cycle behavior of the homogeneous ecosystem model. Even starting from homogeneous initial conditions, it is enough that the vertical exchange rate varies by a factor of less than two, a common situation in the ocean, to completely mask the limit cycle signal in Eulerian time series and to severely damp it in Lagrangian records. Horizontal advection at the ocean mesoscales has been simulated with a simple

quasigeostrophic model, but one can expect that any more advanced representation of ocean turbulence can only further mask the oscillations. Clearly, the fact that limit-cycle behavior can be disguised by advection does not imply that self-sustained oscillations are a real property of plankton dynamics in homogeneous conditions. These results simply show that self-sustained oscillations, when and whether they were present in homogeneous conditions, can become undetectable in Eulerian time series. Interestingly, Lagrangian signals keep a track of the limit-cycle behavior. Thus, the analysis of Lagrangian time series can help assessing the issue of whether models predicting limit cycles in plankton abundance provide a reasonable representation of the marine ecosystem.

A central conclusion of the work reported here is that the behavior of a homogeneous model and that of the same model in the presence of advection can differ significantly. Thus, inferences drawn from the analysis of homogeneous ecosystems should be taken with caution, and the role of horizontal advection and dispersion should be taken into account as an important actor in ecosystem dynamics.

The study presented here shows how intricate can be the interactions between mesoscale dynamics, even when only its horizontal component is taken into account, and the biological component of the ocean system. However, ocean eddies are three-dimensional flow features, thus a more complete comprehension of the biophysical processes involved must be based on the understanding of the three-dimensional physics of coherent vortices.

Chapter 4

Primitive Equations and the problem of the vertical velocity

In this Chapter I introduce the Primitive Equations. This mathematical model represents the foundation for the rest of this thesis, which focuses on the dynamics of three-dimensional mesoscale open-ocean vortices.

4.1 Introduction

The quasi-geostrophic framework (Pedlosky, 1987), simple and fast to solve numerically, has been proven a useful tool in the representation of horizontal advection in vortex-dominated flows, and in the interpretation of their velocity distributions, transport and mixing properties (Provenzale, 1999; Pasquero *et al.*, 2001; Bracco *et al.*, 2004). However, the QG approximation does not capture ageostrophic effects and it is limited in the representation of the three-dimensional structure of real, stratified ocean flows. This is overcome by using the Primitive Equations (Pedlosky, 1987; Salmon, 1998), widely adopted in regional ocean modelling (see Chapter 5) as well as in investigations of submesoscale frontal dynamics (Levy *et al.*, 2001b; Martin *et al.*, 2001; Mahadevan, 2006; Mahadevan and Tandon, 2006). The formulation and features of PE are reviewed below.

4.2 Formulation

The Primitive Equations derive from from eq. (2.1)-(2.4) and describe the dynamics of an incompressible, continuously stratified fluid in a local coordinate system (x, y, z) with a free-surface boundary, in the Boussinesq approximation (2.5) and with the hydrostatic vertical momentum balance (2.8):

$$\nabla \cdot \mathbf{u}_H + \frac{\partial w}{\partial z} = 0 \tag{4.1a}$$

$$\frac{D\mathbf{u}_H}{Dt} + 2f\mathbf{k} \times \mathbf{u}_H = -\frac{1}{\rho_o}\nabla p - \frac{g\rho}{\rho_o}\mathbf{k} + D_U + F_U \tag{4.1b}$$

$$\frac{\partial p}{\partial z} = -\rho g \tag{4.1c}$$

$$\frac{DT}{Dt} = D_T + F_T, \quad \frac{DS}{Dt} = D_S + F_S \tag{4.1d}$$

$$\rho = R(T, S, p) \tag{4.1e}$$

The prognostic variables of system (4.1) are the horizontal velocity components $\mathbf{u}_H = (u, v)$, the temperature T and salinity S. Here, $F_{U,T,S}$ represent forcing terms. The density ρ is calculated diagnostically by the equation of state for the seawater $(4.1\mathrm{e})$, and the vertical velocity w is calculated diagnostically from the flow divergence by $(4.1\mathrm{a})$. Equations (4.1) are looked upon as resulting from Reynolds-averaging. This means that any process that occurs on

scales smaller than the model resolution shall be parameterized as $D_{U,T,S}$ terms by Reynolds stresses and turbulent tracer fluxes (Pedlosky, 1987).

The vertical boundary conditions at the free surface, $z = \eta(x, y, t)$, and at the bottom, $z = -H(x, y)$, are respectively:

$$K_M \frac{\partial u}{\partial z} = \tau_S^x(x, y, t) \quad (4.2a) \qquad K_M \frac{\partial u}{\partial z} = \tau_B^x(x, y, t) \quad (4.3a)$$

$$K_M \frac{\partial v}{\partial z} = \tau_S^y(x, y, t) \quad (4.2b) \qquad K_M \frac{\partial v}{\partial z} = \tau_B^y(x, y, t) \quad (4.3b)$$

$$K_T \frac{\partial T}{\partial z} = \frac{Q_T}{\rho_o c_P} \quad (4.2c) \qquad K_T \frac{\partial T}{\partial z} = 0 \quad (4.3c)$$

$$K_S \frac{\partial S}{\partial z} = (E - P)S \quad (4.2d) \qquad K_S \frac{\partial S}{\partial z} = 0 \quad (4.3d)$$

$$w = \frac{\partial \eta}{\partial t} \quad (4.2e) \qquad -w + \mathbf{u}_H \nabla H = 0, \quad (4.3e)$$

where K_M, K_T, K_S are vertical diffusion coefficients, τ_S, τ_B are momentum stresses, Q_T is radiative flux, E is evaporation and P is precipitation.

This model has the following features absent in either QG or SW or both:

- the fully three-dimensional structure of prognostic fields, forcing, dissipation terms, and boundary layers,
- the three-dimensional vertical velocity is derived diagnostically from the continuity equation $(4.1a)$,
- the stratification and nonlinear form of the equation of state, accounting for the thermodynamics of seawater, can vary in all three dimensions,
- three-dimensional form of the advection operator,
- free-surface and variable bottom.

Under typical oceanic conditions (low Ro and Fr), these equations govern two well-separated types of motion. One is the high-frequency internal-inertia-gravity wave with frequency ν bounded by $f \leq \nu \leq N$, for which non-linearity is usually small; the other is low-frequency, non-linear, quasi-geostrophic motion, whose horizontal component can be expected to dominate the solution (Gill, 1982). Thus, unlike the quasi-geostrophic models, the formulation given by eq. (4.1) resolve divergence effects present in the shallow-water system, while it simultaneously features a fully three-dimensional resolution of the ocean dynamics absent in SW. Thus it allows to fully account for the ageostrophic modes in the overall solution.

As intrinsically hydrostatic, the model does not account for non-hydrostatic (NH) effects: vertical acceleration and Coriolis force in the vertical momentum equation. These however are expected to be negligible on the range of scales considered here, as indicated both by scaling arguments (Salmon, 1998) and by comparative numerical studies of submesoscale flows with PE and NH models alike (Boccaletti *et al.*, 2007; Mahadevan, 2006). Consequently, oceanic

phenomena such as breaking of internal waves, convection, and shear-induced overturning are not admitted; their effect must be included by an adequate numerical scheme (see Section 5.7).

4.3 Vorticity dynamics in Primitive Equations

In order to identify eddies and study their dynamics, a measure of the vortical component of the motion needs to be defined. In a stratified flow, potential vorticity is of general use, and the quasi-geostrophic approximation adopts (2.18). For Primitive Equations, the concept of Ertel's potential vorticity is usually invoked (Ertel, 1942; Hoskins and Bretherton, 1972; Vallis, 2006). It is defined as the component of absolute vorticity which is perpendicular to the density gradient and can be expressed as:

$$q = \vec{\omega} \cdot \nabla b, \quad \text{where } b = -\frac{g\rho}{\rho_o} \tag{4.4}$$

is the buoyancy. The quantity (4.4) has been used for interpretation of observational data (Tokos and Rossby, 1991; Allen and Smeed, 1996) and studies of submesoscale fronts (Thomas, 2005). A limitation associated with (4.4) is that q is not a prognostic variable as it depends on temperature and salinity fields through the nonlinear equation of state, thus it entangles both the three-dimensional momentum and tracer equations. These arguments point to use of vorticity rather than potential vorticity to describe vortical flows. In the primitive-equation formulation, vorticity is a three-dimensional vector. However, rapid rotation and stable stratification ensure that in the ocean vertical velocities are small compared to horizontal ones. The vortical mode of the horizontal dynamics in eq. (4.1) is described by the vertical component of relative vorticity:

$$\zeta = \partial_x v - \partial_y u. \tag{4.5}$$

The use of (4.5) also allows a direct comparison with quasigeostrophic systems. Consequently, I have chosen the relative vorticity to be the key quantity in this study.

Novel features of the Primitive Equations model listed in the preceding section imply much richer dynamics of vorticity, governed by (Vallis, 2006):

$$\begin{aligned}\frac{\partial \zeta}{\partial t} + u\frac{\partial \zeta}{\partial x} + v\frac{\partial \zeta}{\partial y} + w\frac{\partial \zeta}{\partial z} = &-(\zeta + f)\left(\frac{\partial u}{\partial x} + \frac{\partial v}{\partial y}\right) + \left(\frac{\partial u}{\partial z}\frac{\partial w}{\partial y} - \frac{\partial v}{\partial z}\frac{\partial w}{\partial x}\right) + \\ &+ \frac{1}{\rho^2}\left(\frac{\partial \rho}{\partial x}\frac{\partial p}{\partial y} - \frac{\partial \rho}{\partial y}\frac{\partial p}{\partial x}\right) + \nabla \times \left(\frac{1}{\rho_o}\frac{\partial \tau}{\partial z}\right) + \nabla \times (D_U).\end{aligned} \tag{4.6}$$

The non-zero vertical advection (last on l.h.s), stretching (first on r.h.s) and tilting terms (second on r.h.s) in (4.6) are new with respect to QG approximation. The baroclinic generation term (third on r.h.s), is accounted for in the definition of potential vorticity (2.18), but here it has a possibly more complex three-dimensional structure. The dissipation term, which comprises the parameterization of the physics of the boundary layer, is three-dimensional as well; and circulation caused by divergent wind forcing can non-linearly interact with pre-existing motions in the subsurface. All these processes might imprint on vortex evolution generating effects that cannot be investigated in quasigeostrophic models. Numerical simulations in an

idealized, yet typical open-ocean configuration, will allow me to address the issue of comparing transport properties of stratified, three-dimensional vortices with their quasigeostrophic equivalents.

4.4 Vertical velocity problem

Vertical motion in the upper ocean, albeit small, is instrumental in supplying nutrients to phytoplankton in the sunlit layers, conveying heat, salt and momentum fluxes, and exchanging gases with the atmosphere. However, the measurement of vertical velocities is a longstanding problem in oceanography due to the lack of reliable observational techniques for the small values involved, at least two magnitudes smaller than those typical of horizontal circulation (Pollard and Regier, 1992). Measurements by vessel-mounted or moored acoustic current profilers are too sparse and generally of unsatisfactory accuracy (Allen *et al.*, 2001). Thus, maps of w can only be constructed relying on indirect methods. Of these, the most successful is the omega equation, a diagnostic equation for w obtained from flow divergence by assuming quasi-geostrophic balance (Tintore *et al.*, 1991; Pinot *et al.*, 1996), where the geostrophic velocity field is derived from hydrographic surveys of density. Omega-based estimates in frontal regions suggest that mesoscale features can be the source of strong vertical velocities, up to 10^{-3} m/s, corresponding to the excursions of the thermocline by 100 m/day (Allen and Smeed, 1996; V.-Belchi and Tintore, 2001). This is one order of magnitude larger than what found in coastal upwelling regions where the vertical transport of nutrients to the surface waters feeds up high biological productivity (Mann and Lazier, 1996). The vertical motion induced by internal waves and tides can be still of one order higher; however, the direct role of these typically high-frequency and propagating phenomena in ocean biogeochemistry is limited to the coastal regions (Granata *et al.*, 1995; Gargett and Marra, 2002) [1] unless interactions of these motions with lower-frequency flows are involved (M. Levy, work in preparation); this is the time scale of mesoscale circulations, comparable to the time scales of biogeochemical processes in the ocean, that makes them so influential in the ocean marine ecosystem (Smith *et al.*, 1996; Mann and Lazier, 1996; Gargett and Marra, 2002; Mahadevan and Campbell, 2002).

The omega equation provides a correct pattern and phase of vertical velocity field when tested against PE modeling (Pinot *et al.*, 1996; Allen *et al.*, 2001), although the discrepancy in magnitude estimation can reach 15%. Moreover, recent studies report on significant systematic errors in the accuracy; these arise from the necessary compromise between spatial resolution (physical variables discretely sampled on a suitable spatial grid) and the synoptic nature of hydrographic surveys (because the time required to complete a survey is comparable with the time scale of evolution of the features studied) leading to errors of 85% in the estimation of net vertical heat flux (Allen *et al.*, 2001). The solution appears also to be sensitive to the choice of the vertical boundary conditions (Allen and Smeed, 1996). In addition, a QG balance form of the omega-equation fails to capture local ageostrophic effects responsible for high vertical velocities at ocean fronts (Giordani *et al.*, 2006). All this has cast doubts on the method based on the omega equation and stimulated three-dimensional modelling studies.

[1] breaking internal tides and waves also contribute to vertical mixing by small-scale ($<$ 500m) turbulence. However, the present work focuses on mesoscale dynamics.

In the primitive-equation model used here, the vertical velocity is a diagnostic variable calculated from the instantaneous flow divergence by the continuity equation $(4.1\mathrm{a})$. The alternative is a nonhydrostatic model providing w prognostically; however as shown by Mahadevan (2006), qualitative results and average vertical fluxes do not depend on whether non-hydrostatic effects are accounted when simulating the mesoscale and submesoscale ocean dynamics. Recent PE numerical investigations of frontal dynamics report on intense vertical motions reaching 200 m/day associated with mesoscale meandering, submesoscale frontogenesis, ageostrophic instabilities and nonlinear interactions with wind-generated circulation; these vertical velocities display intricate three-dimensional spatial structure and non-Gaussian distributions (Levy *et al.*, 2001b; Mahadevan, 2006; Mahadevan and Tandon, 2006; Capet *et al.*, 2007b). Insofar, however, no similar study has been devoted to the w field related to the presence of mesoscale vortices. This is the cornerstone of the present work and its main pioneering aspect. To address the vertical velocity problem in the context of mesoscale open-ocean eddies, I will use a primitive-equation numerical model which is described in the next Chapter.

Chapter 5

Primitive Equations: Numerical methods

This chapter describes the numerical code employed in the remaining part of the work. The principles of model functioning and options relevant for this study are presented. The details of an idealized configuration representative of vortex-dominated open-ocean, are also given.

5.1 Introduction

Over the past 10 years, a variety of ocean circulation models have been designed for regional applications, the most popular being POM (Princeton Ocean Model), MICOM (Miami Isopycnal Coordinate Ocean Model), MIT (Massachusetts Institute of Technology) and most recently, ROMS (Regional Ocean Modelling System) developed jointly by Rutgers University (New Jersey) and UCLA (University of California, Los Angeles). For the purpose of this work, I have chosen the ROMS model version 2.2 for its potential ability to simulate mesoscale processes at high resolution as well as a wide choice of innovative solutions for advection and mixing schemes.

The model, written in Fortran90/95, solves the Primitive Equations (4.1) using a staggered "C" grid in the horizontal and terrain-following vertical coordinates, which allow to smoothly represent the irregular shape of the model domain and to enhance resolution at the desired depth. The code employs a mode splitting technique whereby the fastly evolving barotropic and slow baroclinic variables are time-marched separately, with a special averaging procedure for the barotropic mode. An elaborated, third-order predictor-corrector (Leap-Frog/Adams-Molton) time-stepping algorithm allows a substantial increase in the permissible time-step size.

The concept of ROMS is to provide the best and newest available algorithms in a modular code with a single makefile, 477 files and over 340 000 lines of code; a large number of choices, including different advection, diffusion, boundary conditions, forcing and data assimilation schemes can be selected; the desired executable code is configured through a C-language preprocessing (CPP) commands which provide users with a large flexibility. The model can be run in either serial (OpenMP 2.0 Standard) or parallel (MPI) mode. The Network Common Data Format (NetCDF) offers portability and direct array accessibility thus facilitating the interchange of data between computers as well as the analysis.

ROMS is widely used by the scientific community for a diverse range of regional applications: the southern Agulhas Current (Penven *et al.*, 2001), the California Current (Marchesiello *et al.*, 2003; Penven *et al.*, 2006), the Middle Atlantic Bight (Fennel *et al.*, 2006) and the Artic region (Smedsrud *et al.*, 2006). This chapter continues with description of options relevant for my work; for additional information on the model features the reader is invited to consult Haidvogel *et al.* (2000) and Shchepetkin and McWilliams (2005), as well as to the documentation and support provided by the Rutgers University community (https://www.myroms.org/wiki/ and http://marine.rutgers/edu/po).

5.2 Spatial discretization

5.2.1 Vertical grid

Stratified oceanic flows governed by eq. (4.1) are characterized by the dominance of lateral over vertical transport. Hence, it is a common modelling strategy to build a computational domain by orienting the two horizontal coordinates orthogonal to the local vertical direction as determined by gravity. The choice of vertical coordinate system is the single most important aspect of ocean model design and in general three solutions are available: geopotential (depth coordinates), isopycnic (representing potential density surfaces) and terrain-following (so-called "stretched" or "s") coordinates (Griffies *et al.*, 2000). The numerical model chosen for this work belongs to the last group. In building its coordinate system it uses a staggered vertical grid principle, which will be introduced first.

A staggered grid

The *staggered grid* solution with variables discretized at alternate points in space is schematized in Figure 5.1a. Vertical resolution N_z gives the number of layers between $N_z + 1$ vertical w-points (called z_w depths) at which are variables with specified vertical boundary conditions are evaluated: vertical velocity, forcing terms and vertical diffusion coefficients. Thus, z_w include the ocean bed and the free-surface. The z_w depths intervene with vertical r-points (z_r depths) where the tracer and horizontal velocity components are computed. The derivatives of vertical r variables are evaluated at w-points and vice-versa.

Stretched coordinate transformation

The model uses stretched (terrain following) s coordinates, a uniform mapping between depth z and a set of curves which follow the variations of sea bottom and deformations of the free-surface. Its main advantage over the z-coordinate is the ability to enhance the resolution near the surface layer, a crucial region in a configuration of surface-intensified vortex dynamics; the additional penalty of the depth-coordinate models is that they have been found to produce vorticity errors in the presence of wind forcing (Mellor *et al.*, 2002). The main preference over the isopycnal coordinates is an improved representation of the subsurface and bottom layers, or generally weakly-stratified regions. Moreover, the formulation for seawater thermodynamic is much more problematic in ρ-coordinates than on the stretched grid (Griffies *et al.*, 2000).

The transformation from the depth, z, to the stretched s coordinates, is in general given by $\hat{x} = x$, $\hat{y} = y$, $\hat{t} = t$ and

$$\begin{aligned} s &= s(x, y, z) \\ z &= z(x, y, s), \end{aligned}$$

associating the lowermost coordinate level with the the ocean floor and the uppermost one with the surface. The s coordinates are set by:

$$s = ((0 : N_z) - N_z)/N_z, \quad s = ((1 : N_z) - N_z - 0.5)/N_z, \tag{5.1}$$

for w- and r- vertical points respectively. The form for s used in the model, adapted from Song and Haidvogel (1994), is:

$$z = \eta + \left(1 + \frac{\eta}{H}\right)\left[h_c + (H - h_c)C(s)\right], \tag{5.2}$$

where the set of s-curves used to stretch the vertical grid is given by:

$$C^o(s) = (1-b)\frac{\sinh(\theta s)}{\sinh(\theta)} + b\frac{\tanh[\theta(s+1/2)] - \tanh[\theta/2]}{2\tanh[\theta/2]}, \tag{5.3}$$

where the subscript o refers to the unperturbed primary depth. Parameters θ, b and h_c are chosen by the user to enhance the vertical resolution where adequate. The surface control parameter θ spans $0 \geq \theta \geq 20$, and the higher its value the more resolution is put near the surface. However, too high values of θ cause a subtle mismatch in the discretization of the model equations, for instance in the horizontal viscosity term, so it is recommended to keep it $\theta \leq 5$ for most applications. More layers are put near the bottom for higher values of the bottom control parameter b which range is $0 \geq b \geq 1$; and the resolution is additionally augmented near a critical depth h_c.

The transformation given by eq. (5.1)-(5.3) has a linear dependence on η, is infinitely differentiable in s and its Jacobian is:

$$\mathcal{H} \equiv \frac{\partial z}{\partial s}. \tag{5.4}$$

In the numerical model, $\mathcal{H}$ is computed discretely as $\Delta z/\Delta s$ since it leads to the vertical sum of $\mathcal{H}$ being exactly the total water depth.

The chain rules for this transformation are:

$$\left(\frac{\partial}{\partial x}\right)_z = \left(\frac{\partial}{\partial x}\right)_s - \left(\frac{1}{\mathcal{H}}\right)\left(\frac{\partial z}{\partial x}\right)_s \frac{\partial}{\partial s} \tag{5.5a}$$

$$\left(\frac{\partial}{\partial y}\right)_z = \left(\frac{\partial}{\partial y}\right)_s - \left(\frac{1}{\mathcal{H}}\right)\left(\frac{\partial z}{\partial y}\right)_s \frac{\partial}{\partial s} \tag{5.5b}$$

$$\frac{\partial}{\partial z} = \left(\frac{\partial s}{\partial z}\right)\frac{\partial}{\partial s} = \frac{1}{\mathcal{H}}\frac{\partial}{\partial s}. \tag{5.5c}$$

As a trade-off for this geometric simplification the dynamic Equations (4.1) become somewhat more complicated (after dropping the carrats):

$$0 = \frac{\partial \mathcal{H}}{\partial t} + \nabla(\mathcal{H}\mathbf{u}_H) + \frac{\partial(\mathcal{H}W)}{\partial s} \tag{5.6a}$$

$$\frac{D\mathbf{u}_H}{Dt} + 2f\mathbf{k_s} \times \mathbf{u}_H = -\nabla\phi - \frac{g\rho}{\rho_o}\nabla z - g\nabla\eta + F_U + D_v \tag{5.6b}$$

$$\frac{\partial \phi}{\partial s} = -\left(\frac{g\mathcal{H}\rho}{\rho_o}\right) \tag{5.6c}$$

$$\frac{DT}{Dt} = D_T + F_T, \quad \frac{DS}{Dt} = D_S + F_S \tag{5.6d}$$

$$\rho = R(T, S, p) \tag{5.6e}$$

where $\mathbf{u}=(u, v, W)$, $\mathbf{u}\nabla = u\partial_x + v\partial_y + W\partial_s$. The vertical velocity in s coordinates is given by:

$$W(x, y, s, t) = \frac{1}{\mathcal{H}}\left[w - (1+s)\frac{\partial \eta}{\partial t} - u\frac{\partial z}{\partial x} - v\frac{\partial z}{\partial y}\right]. \tag{5.7}$$

Other symbols have the same meaning as in eq. (4.1), but now they stand for the variables in the stretched coordinate system. Notably, using s-coordinates results in an appreciable simplification of vertical boundary conditions which at the free surface ($s = 0$) and at the bottom ($s = -1$) become, respectively:

$$\left(\frac{K_M}{\mathcal{H}}\right)\frac{\partial u}{\partial s} = \tau_S^x(x,y,t) \quad (5.8a) \qquad \left(\frac{K_M}{\mathcal{H}}\right)\frac{\partial u}{\partial s} = \tau_B^x(x,y,t) \quad (5.9a)$$

$$\left(\frac{K_M}{\mathcal{H}}\right)\frac{\partial v}{\partial s} = \tau_S^y(x,y,t) \quad (5.8b) \qquad \left(\frac{K_M}{\mathcal{H}}\right)\frac{\partial v}{\partial s} = \tau_B^y(x,y,t) \quad (5.9b)$$

$$\left(\frac{K_T}{\mathcal{H}}\right)\frac{\partial T}{\partial s} = \frac{Q_T}{\rho_o c_P} \quad (5.8c) \qquad \left(\frac{K_T}{\mathcal{H}}\right)\frac{\partial T}{\partial s} = 0 \quad (5.9c)$$

$$\left(\frac{K_S}{\mathcal{H}}\right)\frac{\partial S}{\partial s} = (E-P)S \quad (5.8d) \qquad \left(\frac{K_S}{\mathcal{H}}\right)\frac{\partial S}{\partial s} = 0 \quad (5.9d)$$

$$W = 0 \quad (5.8e) \qquad W = 0 \quad (5.9e)$$

The set of unperturbed primary curves given by eq. (5.3) follows the system evolution according to:

$$C(s) = C(s)^o + \eta\left(1 + \frac{C(s)^o}{H}\right). \quad (5.10)$$

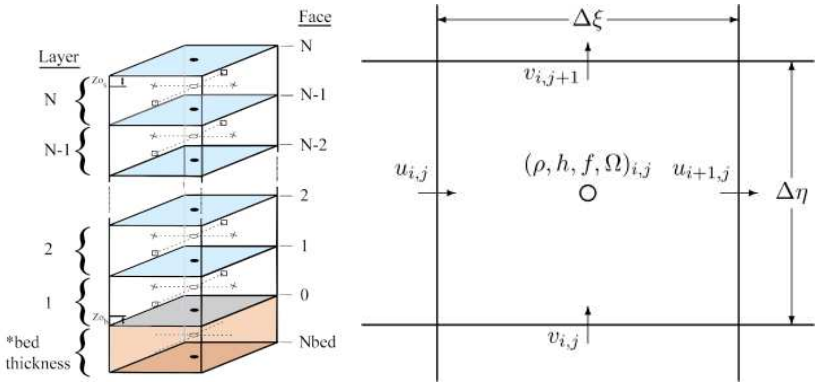

Figure 5.1: (a) Vertical placement of s – surfaces. (b) Schematic of the placement of model variables on the staggered horizontal Arakawa "C" grid.

5.2.2 Horizontal Grid

ROMS employs the Arakawa "C" grid, characterized by an alternate placement of tracer and velocity variables as shown in Fig. 5.1b. Tracer fields and vertical velocity are evaluated at so-called horizontal tracer-, or r-points. The u component falls on the interface between tracer cells in the x direction. Similarly for the v component in the y direction. The advantages are trifold. Firstly, such a lattice will have four times less variables per unit area than the one with

all the variables overlapping, which reduces the computational time as well as filters shortest and fastest waves (Mesinger and Arakawa, 1976). Secondly, this discretization assures that a numerical shallow water wave frequency increases monotonically with wavelength as does the solution in eq. (2.20), which translates into a correct behavior of barotropic waves in the PE system. Thirdly, it performs very well at fine resolution due to the off-set between the horizontal velocity components which implies some interpolation during the computation. In contrast, another popular choice, the grid "B", where both velocity components are solved at the same point, shows a spurious wave-frequency maximum in the $(\nu - \kappa)$ space (Arakawa and Lamb, 1977) related to a computational checkboard mode in the solution (Griffies *et al.*, 2000)[1].

5.3 Equation of state

In the Primitive Equations the density is a diagnostic variable determined by the equation of state (eq. 5.6e), which for seawater is a complicated, non-linear function of temperature, salinity and pressure. In general, oceanography relies on the officially accepted, empirical UNESCO equation, but the numerical calculation of density based on it can account for 15-20% of the computational load (Griffies *et al.*, 2000). For that reason ROMS implements a reformulation of UNESCO equation of Jackett and McDougall (1995). It is a polynomial expression found by fitting to 248 oceanographic observations, which uses potential temperature (prognostic model variable) instead of the in situ temperature (diagnostic variable) and pressure is understood as interchangeable with depth. This method saves a significant amount of computer time and can directly calculate Brunt-Väisäla frequency.

5.4 Time discretization

The time scales of variability of oceanic processes range from seconds to thousands of years. This fact has motivated the *time-splitting technique* (Griffies *et al.*, 2000) where the different modes are time-marched separately, so that the integration of slower variables is accelerated. For the stability of the regional-scale ocean model four time scales are important, quantified by the maximum characteristic speeds that need to be resolved:

1. The inertial time scale with wave speeds $c_f = 2dx \cdot f$ which yields 0.2 $m\,s^{-1}$ for horizontal spacing of dx=1km,

2. A time scale related to the advection speed, that do not usually exceed 1 $m\,s^{-1}$,

3. The time scale of evolution of three-dimensional, depth-varying (baroclinic) fields in eq. (4.1), as for example, internal waves with frequencies ν bounded by $N \leq \nu \leq f$. Their phase speeds, $c_p = \sqrt{g'\delta z}$, depend on the stratification and are typically not larger than 10 $m\,s^{-1}$,

4. The time scale determined by the phase speed of barotropic gravity waves $C_P = \sqrt{gH}$ which reach 100 $m\,s^{-1}$ in the basin of 1000 m depth.

[1] When the resolution is coarse and waves poorly resolved, geostrophy is better represented by the "B" grid because of the co-location of velocity points, which is the reason behind its popularity in the large-scale climate modelling studies in contrast to regional models like ROMS.

Thus the stability of the barotropic mode determines that of the whole model and as a consequence the barotropic time step δt needs to be smaller than the time step Δt used for the baroclinic fields. An adequate time-stepping algorithm for such a problem should fullfill the following requirements (Shchepetkin and McWilliams, 2005):

- have high efficiency, i.e a possibly large stability limit, quantified by the Courant number $Cu = C_P \kappa_{MAX} \delta t$, and possibly small ratio between baroclinic and barotropic time steps, $M = \Delta t / \delta t$,
- resolve the problem of coupling between barotropic (fast) and baroclinic (slow) modes in eq. (4.1),
- ensure that if a tracer field is initially uniform in space, it will remain so at later times,
- ensure the integral volume conservation property: in a hydrostatic free-surface model the vertical velocity computed from the 3D continuity equation $(4.1\mathrm{a})$ must be consistent with changes in control volumes determined by the dynamics of the fast-evolving free-surface,
- be compatible with the method of evaluation of Coriolis terms as well as advection and mixing schemes,
- satisfy all above conditions with minimal storage and work demands.

There are two ways to time-step in oceanic modelling (Griffies *et al.*, 2000; Shchepetkin and McWilliams, 2005): synchronous, where all the equations are computed at once and applied every time step, and forward-backward (FB). The first method is common in ocean modelling and it is usually realized by the Leap-Frog algorithm (MOM, MICOM, POM). It can be available to high orders of accuracy but is not very efficient ($Cu \leq 1$). The FB technique is approximately twice as efficient, but only first-order accurate. The time-stepping solution of ROMS was intended to generalize synchronous algorithms: a predictor (Leap-Frog) substep of the form:

$$Q^{n+1,*} = Q^{n-1} + 2dt\mathcal{F}(Q^n), \tag{5.11}$$

and a corrector step of the form:

$$Q^{n+1} = Q^n + dt\mathcal{F}(c_1 Q^{n+1,*} + c_2 Q^n + c_3 Q^{n-1}), \tag{5.12}$$

where superscripts denote the time level at which the terms is evaluated and $(c_1, c_2, c_3) = (5/12, 8/12, -1/12)$ can be recognized as coefficients of the third-order Adams-Moulton (AM3) scheme (Canuto *et al.*, 1988). Additionally, the model introduces a FB-like feedback at both stages, so that the newly computed momentum field is used to update the tracer equation, and vice-versa, after the predictor substep rather than only at the next time step. The time-marching algorithm, described in more detail in the Appendix, is both conservative and able to preserve tracer homogeneity due to slow-fast mode coupling at every baroclinic time step n and every half-step $n + 1/2$. The storage requirements are reduced by using the same arrays for the newly-computed variables after predictor and corrector substeps. The additional computational cost of the predictor-corrector technique relative to the centered scheme (due to the

elevated number of stages, see Appendix) may be offset by allowing the use of a larger time step. Indeed, inverse stability analysis suggests that the Courant number for the barotropic scheme applied in ROMS can be as high as 1.14 (Shchepetkin and McWilliams, 2005). In practice however, the stability properties are additionally affected by vertical stratification and forcing, and the resulting time-step is usually smaller than theoretically predicted.

5.5 Advection

The choice of the advection scheme is crucial as it can greatly affect the solution: in an intercomparison study, Ezer *et al.* (2002) have shown that most of the differences in the solutions between the ROMS and POM models are due to advection schemes while Levy *et al.* (2001a) got primary production estimates that varied by 30% depending on the numerics of transport. The advective schemes use the flux formulation form for a quantity ϕ:

$$\frac{\partial \phi}{\partial t} + \frac{\partial}{\partial \mathbf{x}}(\mathbf{u}\phi) = 0. \tag{5.13}$$

while differing in their estimation of the advective flux across the faces of the grid cells. In general, there is a tradeoff between conservation and smoothness, which exists between centered schemes and dissipative schemes. Centered schemes (conservative) preserve first (total tracer) and second (tracer variance) moments but admit dispersive errors which tend to result in overshoots for sharp fronts and artificial extrema. In contrast, dissipative schemes suppress dispersion errors yet only conserve the first moment (Griffies *et al.*, 2000). Additional considerations arise when the flow becomes turbulent and cascades of enstrophy and tracer variance associated with mesoscale eddies must be dissipated to avoid spurious accumulation of variance at small scales (Shchepetkin and McWilliams, 1998; Levy *et al.*, 2001a).

Third-order, upstream-biased advection schemes used in this work are the model default and belong to the dissipative class. For the baroclinic momentum, a third-order, upstream bias scheme with velocity dependent hyperdiffusion is employed, and a third-order upstream-biased scheme is also used for advection of tracers. These formulations reduce dispersive errors and thus allow the generation of steep gradients; and they are stable for the predictor-corrector methodology of the model (Shchepetkin and McWilliams, 1998). The improved performance of the upstream schemes in the presence of strong gradients results in higher computational cost: 150% relative to the standard second order central difference (Ezer *et al.*, 2002). The fast-evolving barotropic momentum is advected by a second-order central difference scheme; in that case the advective medium is the vertically averaged baroclinic component, kept constant during the barotropic time stepping.

For the vertical advection of tracers, the model uses a fourth-order, central difference method in finite-volume formulation; for the baroclinic momentum it uses an analogous method preceded by interpolation of vertical velocity to horizontal u and v points.

5.6 Horizontal diffusion

The diffusion schemes in ocean models have a dual task of supressing numerical instabilities and parameterize unresolved, small-scale turbulent processes in eq. (4.1). A proper formulation for $D_{U,T,S}$ requires particular care in case of geophysical turbulence. On one hand, diffusion

should be as small as possible to let the turbulent processes develop. On the other, the solution needs to be relatively smooth on the grid scale, thus some dissipation is required to absorb enstrophy and tracer variance cascading towards the smallest scales. Currently, there is no generally agreed-upon form of a physically motivated closure in ocean models and one applies either the Laplacian or biharmonic operator with as small a diffusion coefficient as feasible to maintain numerical stability (Griffies *et al.*, 2000). For the purpose of this work, the biharmonic horizontal diffusion has been employed:

$$D_\phi = -A_H^\phi \nabla_H^2 \nabla_H^2 \phi, \tag{5.14}$$

where ϕ is a momentum or tracer quantity and A_H^ϕ is a constant diffusion coefficient. This form provides enhanced scale-selectivity over the Laplacian, hence allows for less dissipation at the resolved scales while concentrating it at the grid-scale. For that reason it is widely used in numerical studies of 2D turbulence (Provenzale, 1999) and ocean modelling alike (Griffies *et al.*, 2000). However, it has been shown that in the presence of strong vorticity gradients, any form of diffusion might result in spurious diapycnal (cross-isopycnal) transfers of tracers associated with the dissipation vorticity filaments at the grid scale, so-called "Veronis effect" (Roberts and Marshall, 1998). Being asymptotic in nature (there is always a grid scale), the effect is quite insensitive to model resolution and the value of A_H, though it can be partially mitigated by applying the operator (5.14) on isopycnal surfaces. However, isopycnals tend to outcrop on the free-surface in the presence of energetic, geostrophically-balanced eddies leading to problems with numerical stability and a meaningful solution. Therefore in this work I will let diffusion to act along *s*-surfaces irrespective of the drawbacks discussed above.

5.7 Vertical diffusion

All present vertical mixing schemes employ semi-empirical laws to describe the physics of unresolved processes occurring within the Ocean Boundary Layer (OBL), as well as in the interior and bottom boundary layer: fluxes due to wind and buoyancy forcing, current shear instability, advection by unresolved turbulence, internal wave breaking. The formulation chosen here is a non-local, K-Profile Parameterization scheme (KPP) introduced by Large *et al.* (1994). It is an elaborated version of the K-theory, which in general assumes a relationship between turbulent fluxes and first-moment prognostic variables. Unlike in traditional approaches, this relation is not necessary a local one; rather the subgrid-scale, turbulent vertical kinematic flux of a quantity ϕ is given by:

$$\overline{w_\phi \phi} = -K_\phi(z)(\partial_z \phi - \gamma_\phi) = \overline{w_\phi \phi_o} + K_\phi(z)\gamma_\phi, \tag{5.15}$$

where a non-local transport term γ_ϕ is nonzero only for tracers in unstable (convective) forcing conditions when it depends directly on the surface flux $\overline{w_\phi \phi_o}$ and inversely on boundary layer depth d_B and wind forcing. The mixing coefficient K_ϕ in OBL depends on both the surface forcing and the depth of the boundary layer by:

$$K_\phi(\sigma) = d_B \, w^*(\sigma) G(\sigma), \tag{5.16}$$

where a dimensionless vertical boundary layer coordinate $\sigma = z'_B/d_B$ depends on the distance from the surface, z'_B and the boundary layer depth d_B. The latter is set by a bulk Richardson

number $Ri_B = (b_r - b)z'/(u_r - u)^2 + (v_r - v)^2 + u_{TS}) > 0.3$ where u_r, v_r and $b_r = -g\rho_r/\rho_o$ are estimates of the average horizontal velocities and buoyancy in the layer on the top of d_B. The turbulent velocity shear term $(u_{TS}/z') \propto \sqrt{Nw_\phi/z'}$ accounts for the entrainment processes at the bottom of the boundary layer. The shape function $G(\sigma)$ is a cubic polynomial determined by matching conditions for K_ϕ across the OBL, and $w^*(\sigma)$ is a turbulent velocity scale computed by the Monin-Obukhov similarity theory. In the ocean interior, $K_\phi(z) = K^s_\phi(z) + K^w_\phi(z)$, encompassing the mixing due to shear instability and internal wave breaking. The mixing due to shear is a augmented in regions of small local gradient Richardson number:

$$Ri = \frac{N^2}{(\partial_z u)^2 + (\partial_z v)^2} \tag{5.17}$$

by $K^s_\phi(z) = (1 - (Ri/0.7)^2)^3 \cdot K^o_\phi$ in the range of $0 < Ri > 0.7$ where K^o_ϕ is an initial background value set by a model user and it becomes 0 where $Ri > 0.7$ and 1 where Ri becomes negative (Large *et al.*, 1994). Mixing due to internal wave breaking depends on stratification $K^w_\phi = \frac{10^{-6}}{N}\, m^2\, s^{-1}$. The fidelity of the KPP scheme and its advantageous performance relative to other parameterizations has been shown by the comparisons with either observations and small-scale resolving simulations (Large and Gent, 1999; Li *et al.*, 2001). As is customary in ocean modelling, ROMS advances the vertical diffusion in time by an implicit Crank-Nicholson scheme which is stable for an arbitrary K_ϕ (Canuto *et al.*, 1988; McWilliams, 1998).

5.8 Parallelization and data format

The ROMS code can be run in either serial mode (OpenMP 2.0 Standard) or parallel computers (MPI). The relevant compiler-dependent directives are placed in the model kernel and activated by a single makefile switch; configuration options for different systems (Linux, Mac, Sun) are provided. Coarse-grained parallelization is realized by partitioning grid into subdomains (tiles). Each tile is then assigned to particular node/processor and operated by different parallel threads. Synchronization of the solution occurs at the tile boundary ("halo" region) by the MP routines.

The Input/Output (I/O) data structure of the model is realized by NetCDF (Network Common Data Form, www.unidata.ucar.edu/software/netcdf). It is a set of interfaces for array-oriented access and a collection of libraries for C, Fortran, C++, Java, and other languages. Main advantages of NetDCF format is its *portability* (a NetCDF file can be accessed by computers with different rules for storing integers, characters, and floating-point numbers) and *direct-accessibility* (a small array of a large dataset can be loaded immediately, without first reading in the whole file). It facilitates the interchange of data between computers and analysis software.

5.9 Configuration of the numerical model

This section describes in detail the idealized configuration of the numerical model used to simulate open-ocean mesoscale vortices, discussed in Chapter 6. I focus on a simulation with 18 vertical layers and 256x256 horizontal grid points, called V18-256. To elucidate certain aspects of the flow behavior, and the influence of the vertical resolution, additional simulations have been performed; these are described at the end of the section.

5.9.1 Wind-forced vortices

1. **Spatial grid:** The Regional Oceanic Modelling System (ROMS) has been integrated on a flat bottom domain of the depth $H = 1000$ m. The vertical resolution is set to $N_z = 18$ levels, configured to get the finest (17m) resolution near the surface by setting the grid parameters to $\theta = 3.0$, $b = 0.12$ and $h_c = 1.0$ in eq. (5.2) and (5.3); as a result 6 layers spans the first 100m of the water column. In the horizontal, the domain is double-periodic, with physical length of $L = 256$ km, and discretized in 256 grid points in both directions, with a resolution of $dx{=}dy{=}1km$. As discussed in Section 2.3, on these horizontal length scales the curvature effects on the Earth can be disregarded; consequently the system (5.6) is solved in Cartesian frame rotating with a constant Coriolis frequency $f = 10^{-4}\ s^{-1}$, a value characteristic for mid-latitudes.

2. **Initial conditions:** The simulation starts from the state of no motion. The initial stable stratification are set to match sample oceanic profiles of temperature and salinity (World Ocean Atlas 2001, Conkright *et al.*, 2002). These were chosen from a 1000m-deep, sub-tropical part of the Indian Ocean basin (10N, 58E), an example region characterized by the presence of mesoscale eddies (Bruce *et al.*, 1994) being the important ingredient of the marine ecosystem (Wiggert *et al.*, 2005), and the exponential fitting gives:

$$T(z) = 10 + 12e^{(0.017\,z)}\ {}^{o}C, \quad S(z) = 35 + 2.0e^{(0.024\,z)}\ PSU. \tag{5.18}$$

   The density is calculated from equation of state internally by the numerical code as described in Section 5.3.

3. **Forcing and dissipation:** The system is subjected to a narrow-band wind forcing in eq. (5.8a):

$$\tau_S^x(x,y) = 0.1\Big(\sin(2\pi k_x\,x)\sin(2\pi k_y\,y) + 0.3\,d\xi\Big)\ W/m^2 \tag{5.19}$$

   where $k_x = k_y = 6$ is the horizontal wave number in the x and y directions respectively (giving the radial wave number $k_f = \sqrt{k_x^2 + k_y^2} \approx 8$) and $d\xi$ is a white-in-time noise component added at each time step. The wind wavenumber spectrum is intended to be a zero-order approximation of the geostrophic wind in the wavenumber range of oceanic eddies and for periods longer than a couple of weeks (Muller and Frankignoul, 1981), and is the closest approximation to the narrow-band spectral forcing usually adopted in simulations of forced 2D or QG turbulence (Elhmaidi *et al.*, 1993; Babiano and Provenzale, 2007). This form of the forcing is divergent and rotational, but due to its spatial symmetry, on average there is no net input of rotation or divergence into the system. A wavelength of $k_x = k_y = 6$ corresponds to 12 alternating negative and positive circulation cells along the domain length. The radius of such a circulation cell is therefore $256/12/2 \approx 11$ km.

   The bottom forcing eq. (5.9a) and eq. (5.9b) is prescribed by a quadratic drag law:

$$\tau_B^x = \left(\gamma_B\sqrt{u^2+v^2}\right)u, \quad \tau_B^y = \left(\gamma_B\sqrt{u^2+v^2}\right)v \tag{5.20}$$

   with nondimensional drag coefficient $\gamma_B = 3\cdot 10^{-4}$.

With the goal of using this set-up for futher studies of the dynamics of the marine ecosystem, the temperature equation $(5.6\mathrm{d})$ is forced with a costant solar shortwave radiation, $Q_T = 150\ W\,m^{-2}$, a value characteristic for mid-latitudes in April (Hatzianastassiou *et al.*, 2005). The solar flux penetrates through the interior according to exponential decay law of Paulson and Simpson (1977) based on Jerlov water type (Jerlov, 1976), assumed here to be clear open-ocean water. Since the configuration was intended to be as simple as possible, neither diurnal cycle, nor latent/sensible/longwave flux parameterizations are applied. Instead, in order to avoid accumulation of energy and barotropization of the flow (Smith and Vallis, 2001), the solution relaxes to initial profiles of salinity and temperature with characteristic time of 60 days, which allows to reach a long-time statistically stationary equilibrium. The surface fluxes of salinity, as well as vertical bottom fluxes of heat and salt are set to zero in eq. (4.3). The biharmonic diffusion operator given by eq. (5.14) acts along s-surfaces with the same diffusion coefficient of $A_H = 10^6\ m^4 s^{-1}$ for temperature, salinity and momentum. The background value of vertical mixing for momentum and tracers is initially set to $K_v = 10^{-6}\,m/s^2$ and is modified by KPP scheme (Sect. 5.7) as the flow evolves.

5.9.2 Freely-decaying version

To explain some aspects of the behavior of vortex-dominated, turbulent PE flows, I numerically integrated a freely-decaying version of the configuration, analogous to the one described above, but with wind forcing and relaxation to the initial stratification turned off. The horizontal resolution is again 256^2 collocation points, but the physical size of the domain is either L=256 km, L=128 km, or L = 64 km (referred as FD-256, FD-128 and FD-64, respectively). The vertical resolution and initial stratification are identical. In that case, random initial conditions for surface horizontal velocities are defined by a narrow-band kinetic energy spectrum was $E(k) = \frac{k^{m/2}}{k+k_o^m}$, where wavenumber $k = \sqrt{k_x^2 + k_y^2}$, $k_o = 13$ and $m = 25$ (e.g., Polvani *et al.*, 1994; Bracco *et al.*, 2000c). The initial horizontal velocity decays with depth exponentially with the characteristic depth of 100m. These initial velocities are characterized by a non-zero divergence and Gaussian probability distributions.

5.9.3 Vertical resolution and the mixed layer

Table 5.1: Model set-up of the simulations presented in this work: N_z (number of vertical layers), L (domain length), *ML* (Mixed Layer depth), *WF* (wind forcing) and *DC* (diurnal cycle of the radiative flux).

Feature	V18-256	V80-128	V80ML-128	V20ML-128	FD-256	FD-128	FD-64
N_z	18	80	80	20	18	18	18
L (km)	256	128	128	128	256	128	64
ML (m)	-	-	20	20	-	-	-
WF	+	+	+	+	-	-	-
DC	-	-	+	+	-	-	-

Although idealized simulations of oceanic flows often do not include a representation of a surface homogeneous mixed layer and adopt linear and exponential tracer profiles (e.g., Smith and Vallis, 2001; Thomas, 2007), in the real ocean such a mixed layer (ML) at the top of the fluid column is present. The mixed layer forms in the ocean primarily due to wind waves or convection generated by the loss of heat at the surface. These processes are not resolved at meso- and submesoscales and are only partially parameterized in this idealized configuration by the KPP scheme (Sect. 5.7) under the applied wind forcing and radiation. Therefore, a ML must be externally imposed during initialization of the simulation (Levy *et al.*, 2001b; Mahadevan and Tandon, 2006). New temperature and salinity profiles are defined to introduce a ML of 20m, typical of tropical waters and mid-latitudes in the summer (Mann and Lazier, 1996, chpt. 3.2). The appropriate analytical expressions have been found to keep the initial and relaxation stratification below 20m as close as possible to that given by eq. (5.18) while temperature and salinity above 20m are constant. To futher increase the realism of the configuration, a daily modulation of radiative forcing is introduced with an amplitude of 150 W/m^2. To properly resolve ML, the vertical resolution is set to 80 vertical layers. Consequently, to limit the computational cost, the horizontal physical length of the domain is reduced to 128km while keeping the same horizontal resolution of 1km, and the forcing wavenumbers are changed to $k_x = k_y = 3$ to keep the same forcing scale. The number of layers in the first 100m is 22 with the finest resolution of 3.8 m near the surface. Two simulations in a reduced domain and high vertical resolution have been performed: one with the mixed layer (V80ML-128) and one with original profiles given by eq. (5.18) called V80-128.

A sensitivity study of the impact of vertical resolution has been done with the mixed layer already present, horizontal domain length of 128km, and 20 and 80 vertical layers. These configurations are called V20ML-128 and V80ML-128 respectively. The summary of configurational details is given in Table 5.1. All other parameters are identical to V18-256 simulation, with the exception of horizontal mixing which is twice the original value. The vertical mixing coefficient has not been scaled with increasing resolution because it is modulated by the KPP scheme during the evolution of the system even up to three orders of magnitude depending on local stratification, shear and boundary layer processes. The sensitivity of the results to the vertical mixing is further addressed in Section 6.5.3.

Chapter 6

Results

This chapter describes the properties of simulated three-dimensional, open-ocean eddies. First, the system evolution is investigated. Then, the horizontal component of the vortex-dominated PE flow is compared with QG turbulence, often used in the literature as a first-order approximation to oceanic mesoscale dynamics. This is done by analyzing, in the traditional Eulerian framework, vorticity statistics, wavenumber spectra and velocity distributions. The Lagrangian analysis of transport phenomena completes the picture. The chapter proceeds with the description and interpretation of vertical velocities in presence of coherent structures. This part represents the main original contribution of this chapter. Finally, the effects of a surface mixed layer and of variations in vertical resolution are discussed.

6.1 System evolution and general description

The analysis of the dynamical properties of the simulated flow is based on the V18-256 simulation, integrated in a horizontal domain of 256x256 km^2 (see Sect. 5.9). The sensitivity studies in Section 6.5, aiming at investigating the role of vertical resolution and of the surface mixed layer, are performed on a smaller domain (L=128 km).

6.1.1 Flow evolution

Under the action of the symmetric wind forcing (eq. 5.19) applied to an initially motionless fluid, a process called stratified spin-up (SSU) develops in a time scale of $\mathcal{O}(1/f)$ (Allen, 1973; Pedlosky, 1987; Thomas and Rhines, 2002). The wind-driven motions are deflected to the right by the Coriolis force, associated with convergence and downwelling where the wind-stress curl is negative and divergence and upwelling where it is positive. In a stratified fluid, this circulation is not limited to the few-meter deep Ekman layer, but extends down to a depth of the order of $h_{SSU} = f/k_f N$, which is 100-200m in my configuration. During the first few days the total volume-averaged kinetic energy,

$$KE = \frac{1}{2V}\int_{dv}\left(u^2 + v^2 + w^2\right)dv, \tag{6.1}$$

continually grows with time (Fig.6.1), and so does the surface Rossby number, which can be conveniently estimated in terms of relative vorticity as:

$$Ro = \frac{\zeta}{f}. \tag{6.2}$$

After few days advection processes become important in the overall dynamics, and positive feedback between Ekman transport and negative vorticity regions causes the latter to grow, as shown by Niiler (1969) in the case of a barotropic jet, and explored further by Thomas and Rhines (2002) in the context of an idealized baroclinic front. The asymmetry between positive and negative vorticity regions in the nonlinear regime can be understood by noticing that the

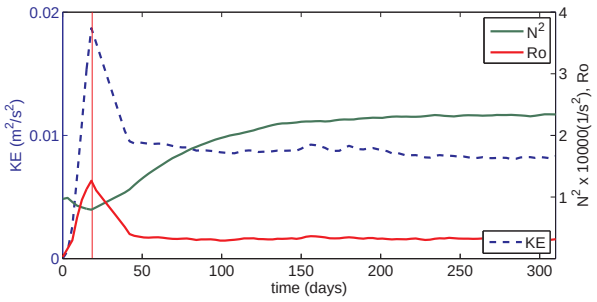

Figure 6.1: Evolution of the volume-averaged total kinetic energy (eq. 6.1), surface average Rossby number *Ro* and squared Brunt-Väisäla frequency (eq. 2.11). The vertical line marks the onset of instability of the Ekman circulation.

Ekman transport induced by a wind stress blowing in the direction of the preexisting flow is given by

$$M_E = \frac{\tau}{\rho_o(f+\zeta)}. \tag{6.3}$$

Thus for flows with locally large *Ro*, the Ekman transport varies inversely with the absolute vorticity rather than f. If relative vorticity is much smaller than f, it can be neglected in eq. (6.3) and the traditional formulation of M_E can be recovered. However, if ζ is negative and close in magnitude (but still smaller) than f, the denominator in (6.3) becomes very small, thus amplifying the wind stress contribution; such effect is absent for positive ζ. The depth-dependent density gets vertically advected, and in consequence the stratification drops in anticyclonic areas (Fig. 6.2a-b). The intense growth of anticyclonic regions is accompanied by weakening of volume-averaged stratification quantified by N^2 (Fig.6.1). After about one week, the average surface $|Ro|$ is greater than 1, and the flow enters into ageostrophic regime. Once $\zeta \leq -f$, the sign of the forcing term in eq. (6.3) reverses. The reversed forcing results in "draining" of anticyclonic cells marked by positive w at their centers (Fig. 6.2c). After $t = 19$ days, upon the vorticity locally reaching $|\zeta| \sim 2f$, a small perturbation due to the random component in the forcing (eq. 5.19) triggers the instability of the stratified Ekman flow (Fig. 6.2d). To pinpoint the instabilities at work, one can follow the guidelines developed for a simple problem of a horizontally uniform, vertically sheared current (Eady, 1949). Based on the value of *Ro* and the local gradient Richardson number *Ri*, the following classification has been elaborated (Stone, 1966; Molemaker and McWilliams, 2005), specifying conditions for the fastest growth rates:

1. geostrophic baroclinic instability: $Ro \to 0$, $Ri \to \infty$,
2. ageostrophic baroclinic instability: $|Ro| \geq 1$, $1 < Ri < 2$,
3. centrifugal instability: $|Ro| \geq 1$, $0.25 < Ri < 1$,
4. Kelvin-Helmholtz instability: $|Ro| \geq 2$, $0 < Ri < 0.25$,
5. gravitational instability: $N^2 < 0$, $Ri < 0$.

A surface map of these regimes during the onset of the instability of the Ekman circulation is presented in Fig. 6.2e. The three (2-4) submesoscale, ageostrophic phenomena can be active in the regions of the flow where the SSU flow breaks up, so the observed instability is likely of a mixed type.

In addition, the flow is characterized by locally negative values of Ri indicative of gravitational instability, which gets damped by the KPP scheme in ROMS (Sect. 5.7). It is worth noting that the wind has a dual role in the destabilization of the nearly-ageostrophic anticyclonic circulation causing $|Ro|$ to rise by a positive feedback with negative vorticity regions and lowering Ri by inducing a vertical circulation that weakens the stratification (Thomas, 2007). Favorable conditions for ageostrophic (2-5) instability phenomena have been found to accompany simulated frontal dynamics (Boccaletti *et al.*, 2007; Capet *et al.*, 2007c; Mahadevan and Tandon, 2006; Thomas *et al.*, 2007); however, in general, it is difficult to draw rigorous conclusions about the occurrence of any of these processes for complex, mesoscale flow configurations dominated by meandering fronts or eddies.

Few days after the onset of instability, the system re-stratifies and after another 200 days reaches a stably-stratified, statistically stationary state (Fig. 6.1), characterized by an average $Ro \approx 0.3$ and therefore evolving in the regime where the quasigeostrophic approximation should provide a satisfactory description of the horizontal dynamics.

6.1.2 General properties of statistically-stationary flow

Surface- and four-day-averaged vertical profiles of temperature, salinity and density are shown in Fig. 6.3a-c. In the following, I will refer to the *surface layer* as the region between the surface and the 1026.7 $kg\ m^{-3}$ isopycnal, where most of the coherent structures are confined (see Sect. 6.1.3), and below which the flow is nearly homogeneously stratified. The surface layer has a depth of about 120m, marked by a black line in Fig. 6.3c.

By analogy to the reduced gravity model (Sect. 2.6.2), and with respect to the surface layer, eq. (2.17) provides an estimate of the first internal Rossby radius of deformation, $\lambda_I \approx$ 15-16 km, typical of extratropical oceans (Stammer, 1997). This value of λ_I is small compared to the domain size and it is only slightly larger than the forcing scale (see Sect. 5.9).

Characteristic (root-mean-square, r.m.s) horizontal velocity across the surface layer is $U \approx 0.1\ m\,s^{-1}$, while the vertical velocities are $W \approx 0.5 \cdot 10^{-4}\ m\,s^{-1}$, and are less intense than (u, v) by three orders of magnitude throughout the fluid column. The magnitudes of horizontal velocity decay rapidly with depth (Fig. 6.3 e). The dynamics can be therefore grossly considered as predominately horizontal (quasi2D) in a slab-like surface flow. Due to the difference in the relative magnitudes of horizontal and vertical flow components, they will be analyzed separately. First, I will focus on the properties of the horizontal circulation and compare them with analogous quantities in QG turbulence. Then I will consider the vertical velocities.

6.1.3 Anticyclonic vortices

The statistically stationary state is characterized by the presence of negative-vorticity vortex monopoles (Fig. 6.4a): anticyclones of various sizes, the largest having a radius comparable to λ_I. Coherent structures are surface-intensified. The smallest features weaken rapidly with depth (Fig. 6.4b), while the strongest eddies can reach values of $\mathcal{O}(0.1\,f)$ at 200m depth.

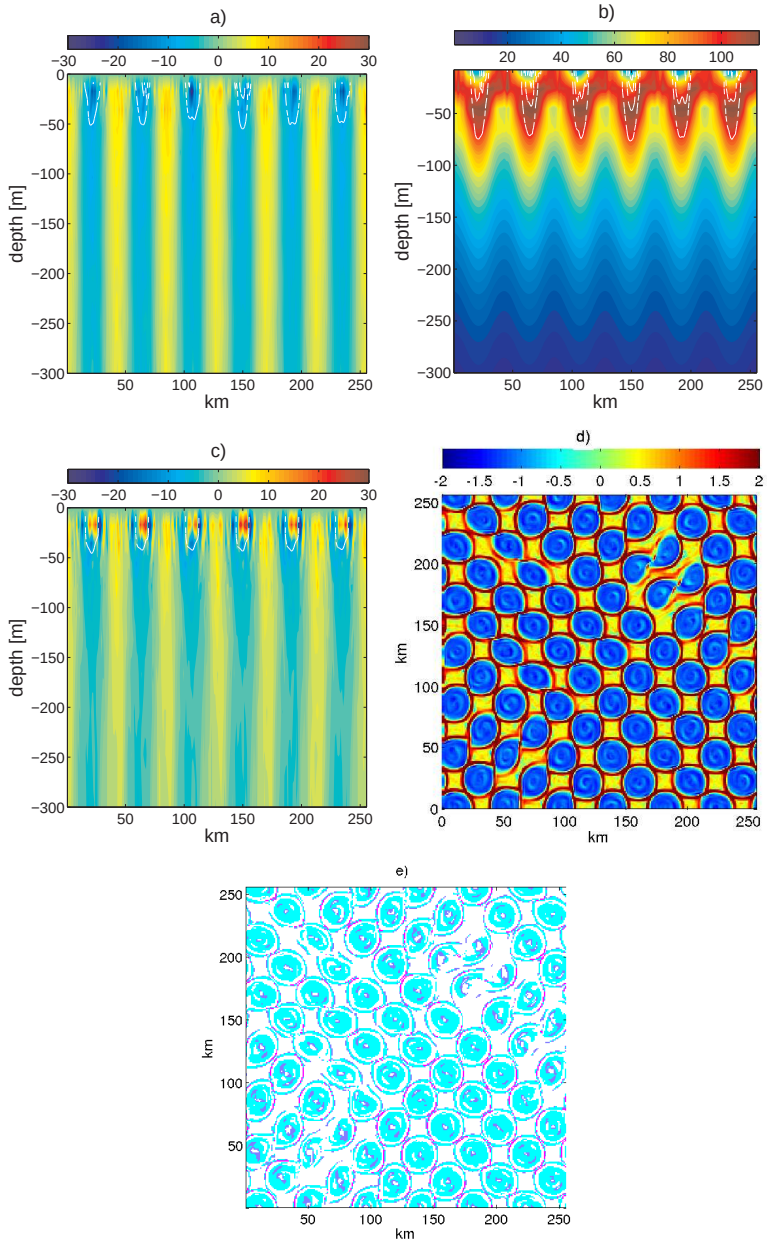

Figure 6.2: (a) A section of the vertical velocity field in the upper 300m on the 3rd day of the simulation, in units of m/day. Anticyclonic circulation cells are marked with a white line. (b) corresponding section of Brunt-Väisäla frequency N in units of f. (c) A section of the vertical velocity field on the 7th day of the simulation in units of m/day. (d) Surface ζ in units of f during the onset of instability of SSU. (e). Corresponding map of instability-favorable conditions: cyan - symmetric centrifugal, dark blue - baroclinic ageostrophic, magenta - Kelvin-Helmholtz. White areas correspond to ($Ro < 1, Ri > 2$), that is, to the geostrophic baroclinic regime.

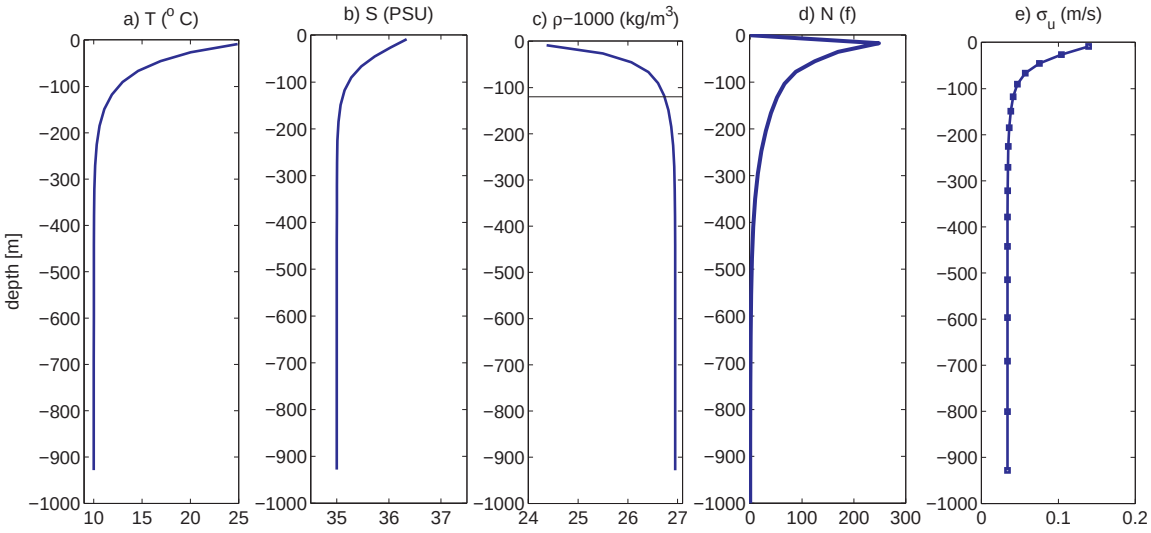

Figure 6.3: Twenty-day averaged vertical profiles after stationarity has been reached: temperature (a), salinity (b), density (c), Brunt-Väisäla frequency in units of f (d) and r.m.s of horizontal velocities (e).

Vortices are surrounded by areas of very high horizontal strain rate, defined as:

$$S = \sqrt{s_n^2 + s_s^2}, \tag{6.4}$$

where $s_n = \partial_x u - \partial_y v$ and $s_s = \partial_y u + \partial_x v$ are, respectively, the normal and shear components (Fig. 6.4 c). Eddies are approximately axisymmetric (an axisymmetric vortex being a stationary solution of the conservative fluid-dynamical equations) and when perturbed by an external strain field they relax back to the circular shape developing shielding rings of positive vorticity (Graves *et al.*, 2006). On each horizontal plane, the relative vorticity field has zero average; cyclonic filaments are abundant, but positive vorticity eddies are absent. Surface vorticity reaches absolute values of $2.5f$, and ageostrophic regions where $|Ro| > 1$ are found inside vortex cores and strong filaments covering about 6% of the domain. The surface-averaged enstrophy $\mathcal{Z} = 0.5 < \zeta^2 >$ decays rapidly with depth (Fig. 6.4d). Surface eddies complete their rotation in approximately one day.

Whenever energetic events occur sparsely in time and/or space, the flow becomes intermittent. A measure of spatial intermittency can be obtained by considering the kurtosis of vorticity, $Ku =< \zeta^4 > / < \zeta^2 >^2$ (McWilliams, 1984). The profile of kurtosis is shown in Fig. 6.4e; the flow is intermittent at all depths, but particularly near the base of the surface layer where only a few large vortices dominate the dynamics (Fig. 6.4b). The basin-averaged kurtosis is $Ku \approx 12$.

As already noticed when analyzing the spin-up of the flow, there is striking dominance of negative-vorticity regions, which in the statistically-stationary state are represented by coherent anticyclones (Fig. 6.4a-b). The evident asymmetry can be quantified by the third moment about the mean (skewness) expressed in dimensionless form by $Sk =< \zeta^3 > /\sigma_\zeta^3$. The vorticity distributions are characterized by negative skewness (Fig. 6.4f), associated with the long tail to the left of the central maximum in the distribution (Fig. 6.4g). The minimum values of Sk are again due to few strong eddies which dominate the dynamics at approximately 100m depth, where cyclonic filaments are very weak (Fig. 6.4b).

Vorticity asymmetry is absent in the QG approximation (Provenzale, 1999; McWilliams and Weiss, 1994) (see Fig. 2.1). In general, three factors can contribute to the observed dominance of anticyclones:

- nonlinear interaction with the wind forcing, that is, positive feedback between Ekman transport and negative vorticity regions (Thomas and Rhines, 2002),
- the ageostrophic free-surface (FS) effect owing to small value of λ_I (Cushman-Roisin and Tang, 1990; Polvani *et al.*, 1994; Graves *et al.*, 2006),
- low values of divergence and weak stretching of vorticity filaments responsible for the preponderance of cyclonic vorticity observed in oceanic fronts (Capet *et al.*, 2007c; Mahadevan and Tandon, 2006), as well as the limited role of baroclinic and centrifugal instabilities (Stone, 1966; Molemaker and McWilliams, 2005).

The first factor has been explained in Section 6.1.1 for the spin-up phase. The "free-surface" (FS) effect, i.e., the sensitivity to background rotation leading to the vorticity asymmetry in

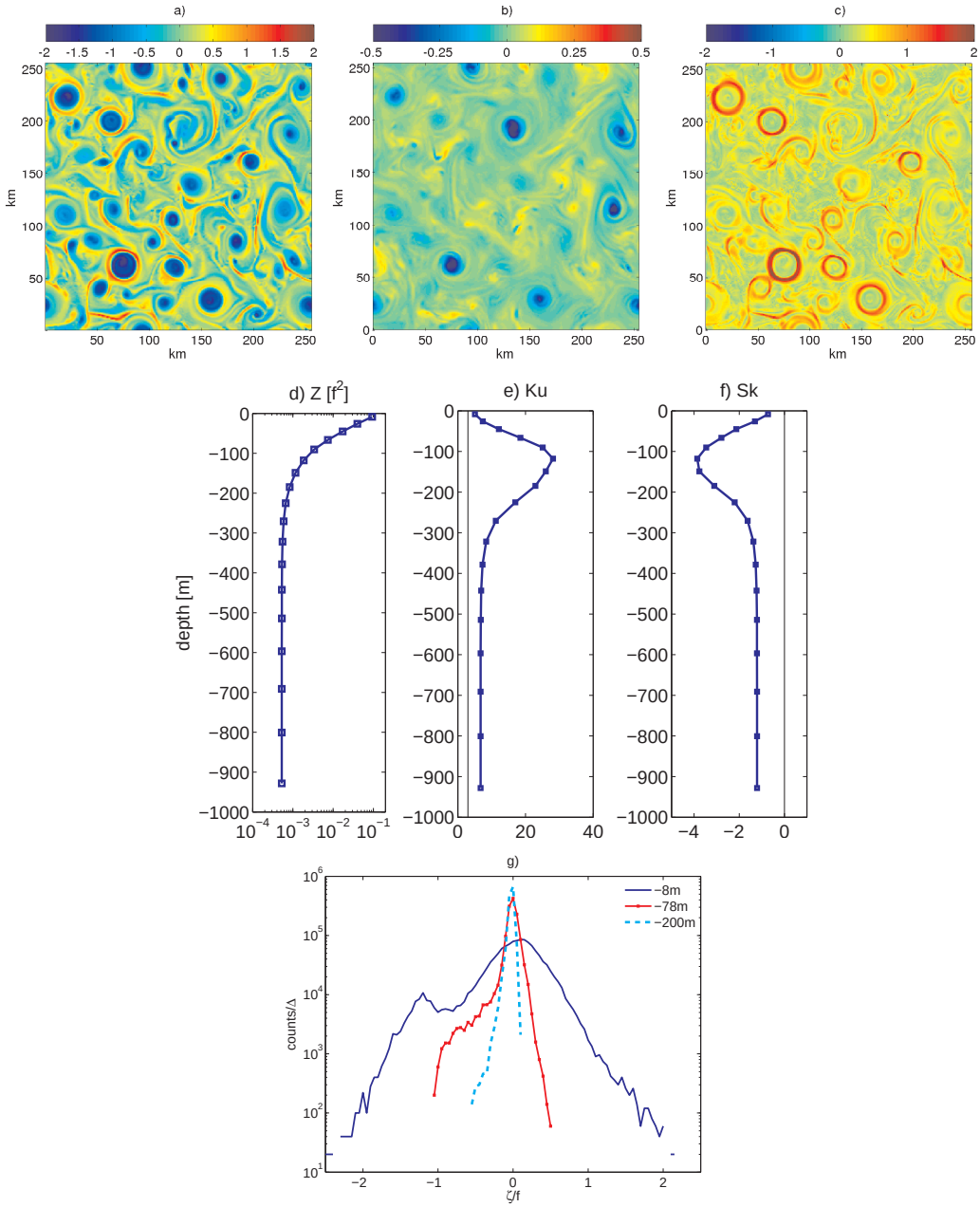

Figure 6.4: Instantaneous snapshot of relative vorticity at the surface in the statistically-stationary state in units of f (a), the corresponding snapshot of relative vorticity at 80m (b), and horizontal strain rate S in units of f (c); twenty-day averaged vorticity statistics: profile of horizontally-averaged enstrophy in units of f^2 and in the logarithmic scale (d), profile of kurtosis Ku (e) and skewness Sk (f); histograms of ζ/f at -8, -78 and -200m, normalized by the bin length Δ; the ordinate scale is logarithmic (g).

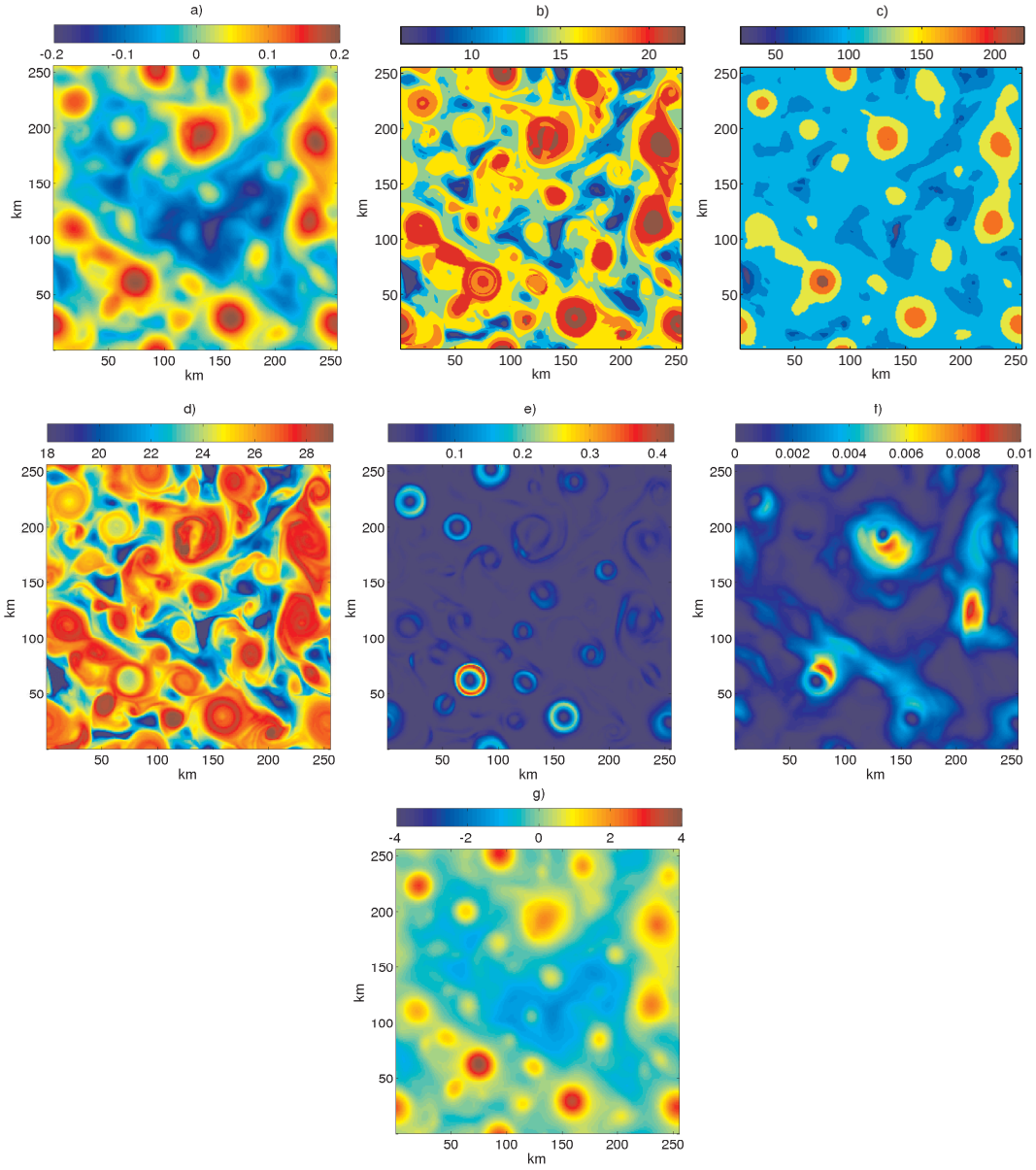

Figure 6.5: Instantaneous snapshots corresponding to the vorticity field in Fig. 6.4: (a) free-surface η (m); (b) the estimate of the internal Rossby radius of deformation λ_I (km); (c) the depth of the surface layer marked by the 1026.7 $kg\,m^{-3}$ isopycnal (m); (d) surface temperature (^{o} C), (e) surface horizontal kinetic energy (m/s); (f) barotropic kinetic energy (m/s). Baroclinic component of KE is not shown as it is visually identical to the map of total kinetic energy; (g) surface streamfunction ψ (units: $10^4\,m^2/s$).

the regime of a small λ_I, has been reported in the reduced gravity model (Sect. 2.6.2) by Cushman-Roisin and Tang (1990) and Polvani *et al.* (1994). Anticyclones (which for positive f are negative-vorticity eddies) tend to be more prevalent than cyclones on a f-plane (β=0) in flows that are not strongly influenced by horizontal and vertical boundaries. Noting the fact that they correspond to positive deformation of the free-surface (see 6.5a), Cushman-Roisin and Tang (1990) argued higher stability of anticyclones from the energy balance. Another heuristic argument has been advanced by Polvani *et al.* (1994) who, based on the value of the surface elevation η, deduced a larger range of influence of anticyclones relative to cyclonic eddies, favoring vortex merging leading to faster growth.

The physical rationale for the coherent-vortex asymmetry has been given by Graves *et al.* (2006) in the context of a weakly-nonlinear shallow-water model. They have demonstated that anticyclones become more robust than cyclones in a finite-Ro and small-λ_I regime under the strain-induced vortex Rossby waves (VRWs) in the vortex axisymmetrization process. These waves are vorticity perturbations that propagate outward while being sheared by the differential angular velocity of an eddy. During the phase-line rotation, VRWs eventually transfer their energy back to the vortex, thereby strengthening it relative to the mean flow; and this effect is stronger for anticyclones. The fact that anticyclone dominance is present also in freely-decaying simulations (Fig. 6.6), initialized with the same stratification (thus the value of λ_I) and Gaussian velocities (see Sect. 5.9.2), suggests that the FS effect is a dominant factor conditioning the persistence and growth of anticyclonic vortices in the present configuration. Still, the continually applied wind-stress is important in generating strong initial negative vorticity maxima and feeds on existing eddies; hence the flow appearance in Fig. 6.4 is a synergic operation of the two processes with possible contribution of ageostrophic instabilities discussed in the next Section.

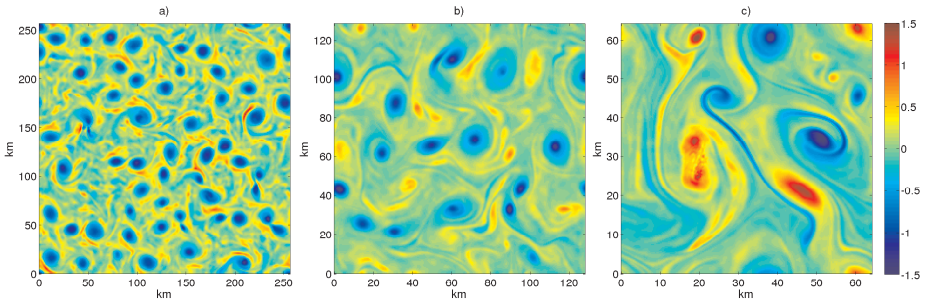

Figure 6.6: Instantaneous snapshot of normalized relative vorticity at the surface, ζ/f, on the 20th day in freely-decaying simulations with varying domain length L, for the same initial stratification and λ_I: (a) L=256km, (b) L=128km, (c) L=64km. The color scale is the same for all three images.

6.1.4 Quasigeostrophic eddies and ageostrophic effects

Negative-vorticity eddies correspond to convex free-surface curvature (Fig. 6.5a) and grossly to high temperature regions (Fig. 6.5d), thus to low density, which implies that their balance

is primarily geostrophic. Vortices correspond to high levels of total kinetic energy which accumulates at scale related to λ_I (Fig. 6.5e). They are mainly baroclinic structures: barotropic energy levels are low and carry signatures of only the largest and deepest eddies (Fig. 6.5f). Coherent anticyclones literally dominate the surface flows, as seen from a map of surface streamfunction ψ, defined as $u = -\partial_y\psi$, $v = \partial_x\psi$, which displays a vast positive anomaly (Fig. 6.5g).

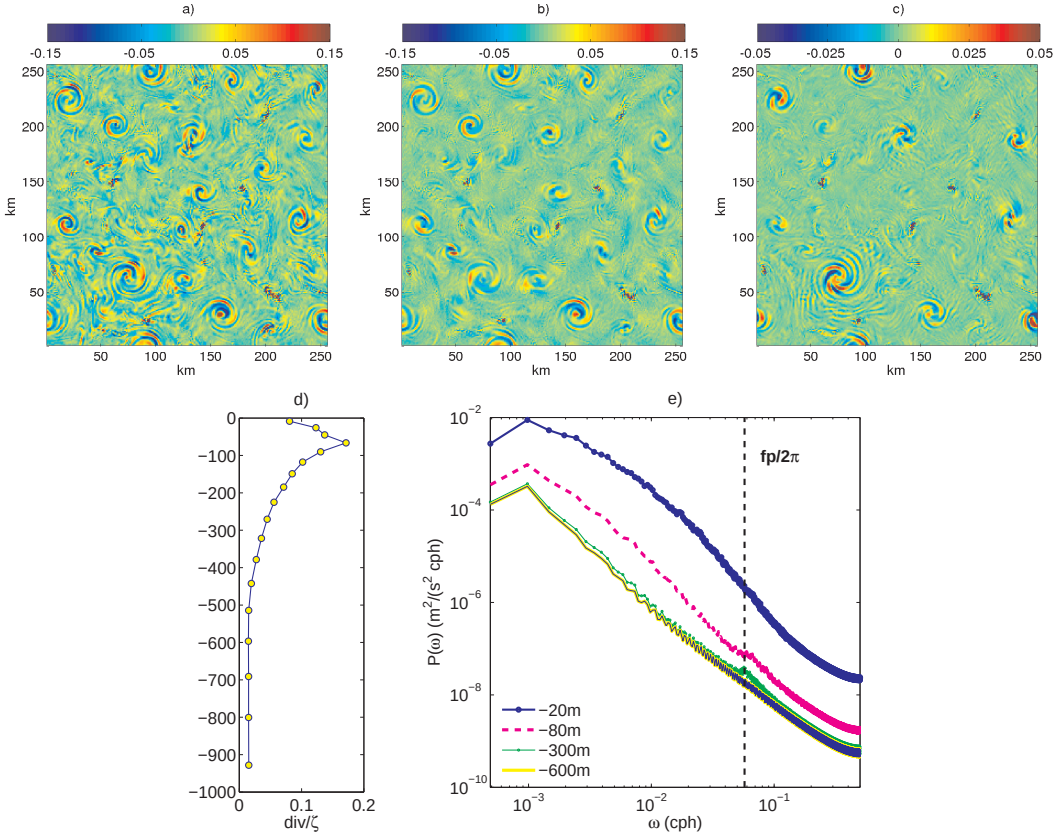

Figure 6.7: (a) Instantenous snapshot of horizontal flow divergence corresponding to Fig. 6.4a at 20m in units of f; (b) a snapshot of two-day-averaged divergence field at 20m (b) and at 80m (c). Ratio of one-day and horizontally-averaged divergence to relative vorticity as a function of depth; (e) Frequency power spectra of horizontal velocity at different depths, calculated over 60 days with a time step of 1h. The velocity signal has been linearly detrended. The dashed line marks the inertial frequency.

In general, a primitive-equation flow is divergent, while the quasi-geostrophic models assume a negligible divergence; thus it is instructive to verify this approximation in the case of simulated mesoscale turbulence. The divergent processes in this configuration include the Ekman circulation and wave motions. Wind stress is a source of near-inertial waves (e.g., Pollard, 1980; Gill, 1984); likewise, a perturbed vortex will excite gravity waves (Brown and Owens, 1981; Montgomery and Lu, 1997) and vortex Rossby waves (Graves *et al.*, 2006). The gravity waves possess frequencies greater than the inertial frequency measured by f,

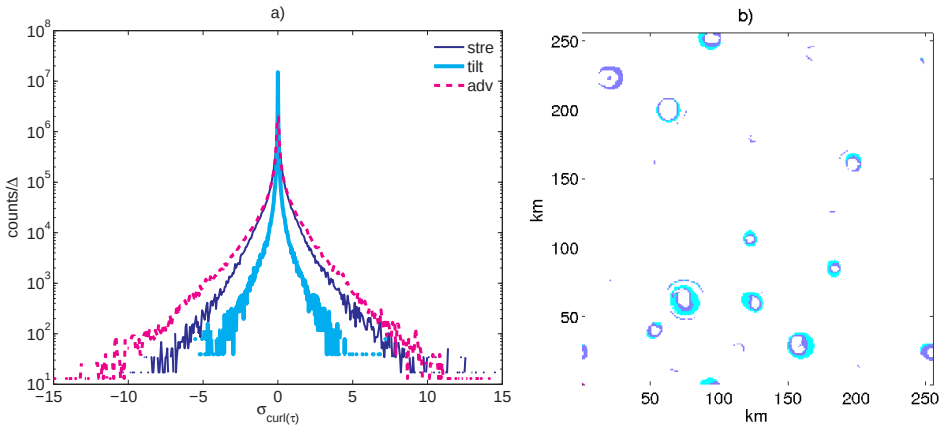

Figure 6.8: Histogram of the contributions of stretching, horizontal and vertical advection and tilting to the vorticity equation, eq. 4.6, in the upper 200m, normalized by the r.m.s of the wind-curl forcing at the surface and by the bin length Δ. All quantities are averaged over one day. The ordinate scale is logarithmic. The baroclinic and diffusion terms are several orders smaller and are not shown. (b) Map of instability-favorable conditions corresponding to Fig. 6.4a: cyan - symmetric centrifugal, dark blue - baroclinic ageostrophic. The stationary state does not support the development of Kelvin-Helmholtz instability, in contrast to the situation shown in Fig. 6.2e. White areas correspond to ($Ro < 1, Ri > 2$), that is, to the geostrophic baroclinic regime (see Sect. 6.1.1).

and are unbalanced (ageostrophic), radiating phenomena. VRWs evolve typically on time scales comparable to the advective scale and feel the background rotation, thus are largely geostrophically-balanced and captured by quasigeostrophic dynamics in a finite-Ro regime, even though they can carry order-one divergence (Montgomery and Lu, 1997; McWilliams *et al.*, 2003). In ageostrophic vortex cores, on the other hand, a well-defined timescale separation between the two types of oscillatory motion is not verified, and fast Rossby waves can exist (Montgomery and Lu, 1997). An instantenous snapshot of horizontal divergence, $u_x + v_y$, at 20m is shown in Fig. 6.7a. The spatial structure of the divergence field is strongly affected by the presence of vortices and filaments and its magnitude is one order smaller than the vorticity. Two-day averaged fields at the depth of 20m and 80m are shown in Figure 6.7 b and c respectively. By time averaging the gravity waves are filtered, hence the persistent wavy appearance related to the presence of vortices is indicative of VRWs, which feel the background rotation during their "slow" propagation, developing a characteristic spiral pattern (Montgomery and Lu, 1997; McWilliams *et al.*, 2003). Near-inertial waves, on the other hand, are hardly discernible on frequency spectra of horizontal velocity dominated by low-frequency motions (Fig. 6.7 d); they manifest themselves in the vertical velocity field, and will be discussed separately in Sect. 6.4. Throughout the fluid column, the magnitude of the one-day averaged divergent flow component is at least one order smaller compared to the vortical component (Fig. 6.7c). Its contribution is highest at the base of the surface layer where the vertical gradients of w are largest (see Sect. 6.4).

Divergence influences the evolution by the stretching of vortex tubes, which is the first

term in eq. (4.6). In frontal dynamics this is believed to be the main cause of preponderance of positive vorticity (Mahadevan and Tandon, 2006; Capet *et al.*, 2007c). In the simulations discussed here, in the absence of frontal divergence, the stretching term is only slightly skewed to the right and smaller in magnitude relative to the advection terms representing the nonlinear phenomena (Fig. 6.8a) which include interactions of the vortices with wind-induced circulation and VRWs. None of the studies of frontal dynamics evaluate systematically the importance of the various terms in eq. (4.6) and therefore a comparison of the significance of stretching in an eddy-dominated flow (as the one studied here) and in frontal circulation is not possible.

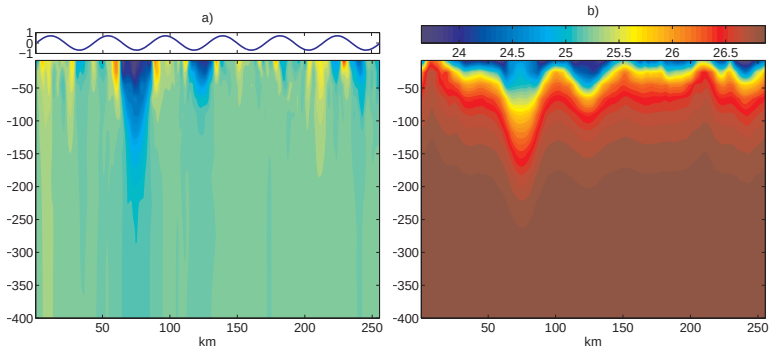

Figure 6.9: Vertical sections through $y = 62\,km$ (refer to Fig. 6.4a) of relative vorticity in units of f; the vorticity colorscale is the same as in Fig. 6.4a. (b) corresponding section of density, $(\rho - 1000)$ $kg\ m^3$. The top panel on the left shows the wind stress curl, $\partial_y \tau_x$, in units of f.

In the weakly-stratified and ageostrophic cores of the eddies, the conditions for development of ageostrophic baroclinic and centrifugal instabilities are favorable (Fig. 6.8b), potentially affecting the evolution of individual anticyclones. On the other hand, the background turbulence, where the formation of vortices takes place, is prone only to geostrophic baroclinic instability according to the classification presented in Sect. 6.1.1. To futher show local ageostrophic effects, I focus on a large, deep, more than two-month-old eddy centered at (80,60) km in Fig. 6.4a; the statistically-stationary flow typically features 3-5 such mature anticyclones inducing the most intense vertical velocities (see Sect. 6.4). Figure 6.9 shows vertical section of ζ and ρ passing through this structure. Concave isopycnals, characteristic of geostrophic anticyclonic vortices (like the small one at 120km) shoal slightly at the core of the big eddy. This might come from the fact that the geostrophic relation (eq. 2.12) does not strictly hold in such a core where the primary balance is expected to be cyclostrophic (beetwen the Coriolis force and the eddy rotation). The nonlinear Ekman dynamics, namely the change of sign of Ekman transport in $Ro < -1$ regions (eq. 6.3) might also contribute: The big vortex approached slowly from the north-west and found itself under a negative wind stress cell (Fig. 6.9a). Wind feeds positively on the vortex growth except at its very center where $\zeta < -f$ and the vorticity input to the vortex is positive. The divergence of Ekman transport results in positive vertical velocities which advect up the denser fluid leading to a small hummock in the isopycnals (Fig. 6.9b). Notably, the field of η does not capture these ageostrophic, submesoscale effects (Fig.

6.5a). From eq. (4.1), one derives that surface elevation η inherently evolves on scales larger than those of the three-dimensional momentum, and for η geostrophy prevails.

In sum, in the regime of small λ_I, which can be considered relevant for open ocean eddies (Cushman-Roisin and Tang, 1990), the simulated mesoscale flow evolves as in a weakly nonlinear shallow-water system with finite *Ro* and finite, though small, divergence. The anticyclone dominance can be explained by the free-surface effect, and it is physically related to the interaction of eddies with vortex Rossby waves in a straining flow. The asymmetry is further strengthened by nonlinear coupling with the wind-generated circulation. The configuration considered here is distinct from frontal mesoscale flows studied by Mahadevan and Tandon (2006) and Capet *et al.* (2007b), where VRWs are not observed and frontal vortex stretching causes the preponderance of positive vorticity. Here, both vortex stretching and ageostrophic instabilities do not dominate the dynamics, but their role is limited to the very core of the most intense vortices.

6.2 Horizontal circulation from an Eulerian viewpoint

In this section I will analyze the simulated horizontal flow and assess similarities and differences with QG turbulence.

6.2.1 Flow Topology

In order to determine whether there are significant differences in the topological properties of the flow related to the presence of vortices, an identification procedure is needed. Vortex-dominated turbulence can be partitioned into coherent structures and filamentary background by using a variety of techniques, including subjective census (McWilliams, 1990), wavelet analysis (Farge and Sadourny, 1989) and methods based on the pressure hessian and eigenvalues of the velocitygradient tensor (Jeong and Hussain, 1995). Here I adopt the Okubo-Weiss criterion to separate coherent structures from the background turbulence in horizontal sections at various depths of my model domain. This partitioning method has been widely used in analysis of 2D turbulence (Ohkitani, 1991; Elhmaidi *et al.*, 1993; Bracco *et al.*, 2000c; Babiano and Provenzale, 2007), 3D QG flow (Petersen *et al.*, 2006) and ocean satellite data (Isern-Fontanet *et al.*, 2006). The Okubo-Weiss (OW) parameter measures the relative contribution of the squared vorticity (ζ^2 in this study) and of the squared horizontal strain rate S^2 (Weiss, 1981):

$$Q = S^2 - \zeta^2, \tag{6.5}$$

Regions dominated by rotation have negative values of Q and are referred to as elliptic domains, while hyperbolic domains have $Q > 0$ and are characterized by strong deformation. The OW parameter has been developed in the context of 2D turbulence. [1]. Although Q is defined for non-divergent flows, a generally small value of divergence in the simulated system (Sect. 6.1.4) encourages its application for separating vorticity-dominated regions where $Q \ll 0$ and strain-dominated regions where $Q \gg 0$ (see Fig. 6.10a). Vortices, largely confined to the surface layer, are identified as connected regions where $Q < -\sigma_Q$, where σ_Q is the standard deviation of Q (Fig. 6.10b) at a given depth. Strongly positive values of Q correspond primarily

[1] Its 3D quasigeostrophic equivalent (the middle eigenvalue of the velocity gradient tensor) has been recently found by Petersen *et al.* (2006).

to edges of "circulation cells" surrounding the vortices, which can be identified by condition $Q > 2.5\sigma_Q$, see Fig. 6.10a and c.

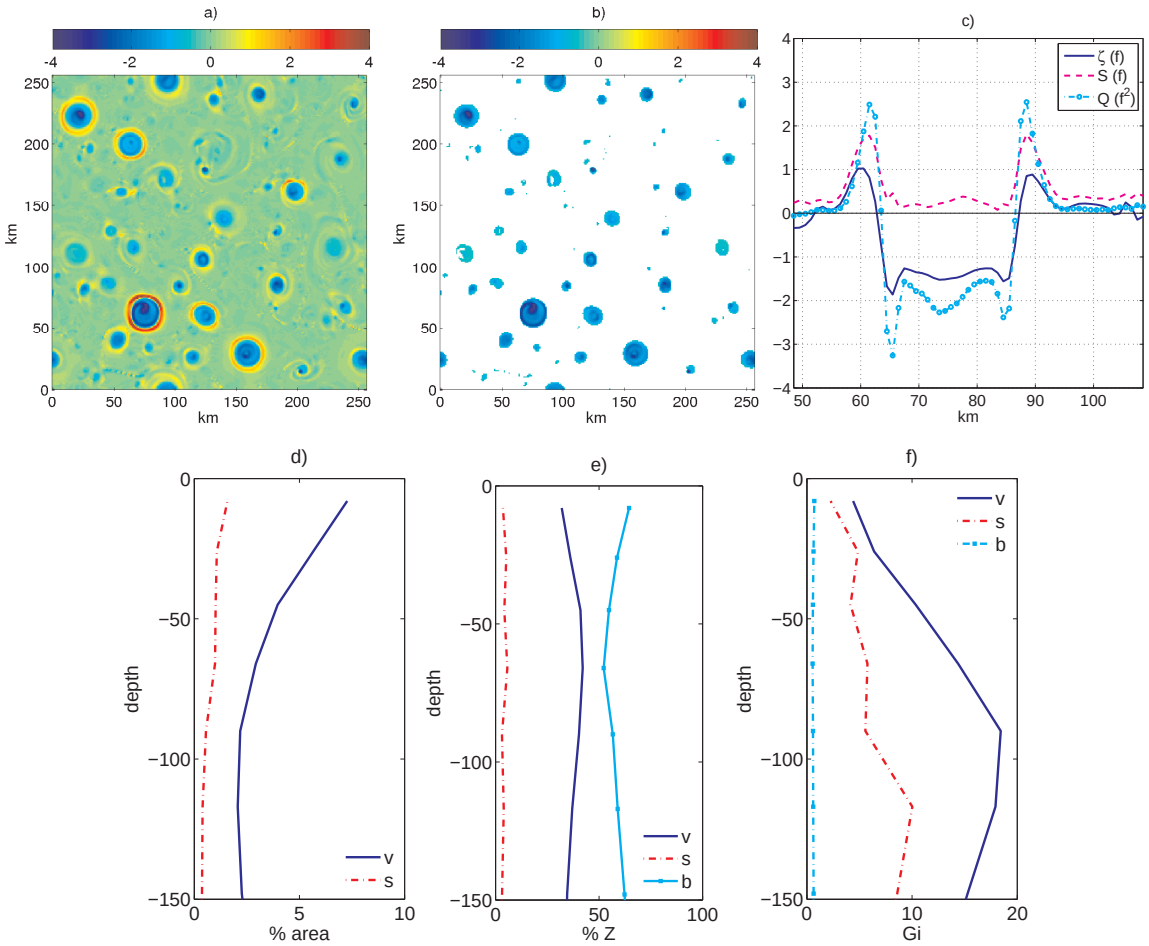

Figure 6.10: Snapshots corresponding to relative vorticity and strain rate fields at the surface, shown in Fig. 6.4a and c: (a) Okubo-Weiss (OW) parameter Q normalized by f^2, (b) the same but when only $Q < -\sigma_Q$ is drawn, the criterion for vortex identification, (c) A cross-section of the OW parameter, relative vorticity and horizontal strain rate across a large anticyclone centered approximately at location (80,60) km in Figure 6.4a. Conditional Eulerian statistics in the surface layer based on horizontal flow partition by means of Okubo-Weiss parameter (4-day averaged): (d) percentage of the horizontal area covered by circulation cells (s) and vortices (v); (e) percentage of total surface enstrophy contained in circulation cells (s), vortices (v) background (b); (f) a profile of the index Gi (s - circulation cells, v - vortices, b - background).

Conditional Eulerian statistics obtained by partitioning the horizontal flow in each model layer with the Okubo-Weiss parameter serves to assess the role of different topological domains in the overall dynamics in the surface layer. The circulation cells cover a very small percentage of the area, with the maximum of 1% at the surface. Vortex cores house up to 6% (Fig. 6.10d); the rest of domain is populated by background turbulence with weak vorticity filaments.

Vortices, however, account for as much as 50 % of the total enstrophy in the surface layer (Fig. 6.10e). To better measure their relative importance, I define the index *Gi* as

$$Gi = \frac{\textit{fraction of } Z}{\textit{fraction of area covered}}. \tag{6.6}$$

The vertical profile of *Gi* is displayed in Fig. 6.10f. The significance of the vortices relative to the background turbulence is striking, they dominate the dynamics with a distinct maximum at the depth of 100m (Fig. 6.10e) where only few deep vortices are able to penetrate and filaments are very weak (Fig. 6.10d-e, compare with Fig. 6.4 b).

6.2.2 Wavenumber spectra

Introduction

The spatial structure of the flow is further studied by analyzing the two-dimensional Fourier spectra, $\hat{E}(k,z)$, calculated on the horizontal plane as a function of depth and radial horizontal wavenumber $k = \sqrt{k_x^2 + k_y^2}$ (Pedlosky, 1987). Thus, $\hat{E}(k,z)$ is the horizontal kinetic energy density in the scalar wavenumber interval between k and $k + dk$ at a given depth z. The surface-layer spectra are compared with those obtained for QG dynamics. In a statistically stationary, forced-dissipative 2D turbulence, energy is transferred by the nonlinear terms in eq. (2.14) from one scale to another following the Kolmogorov-Kraichman's (KK) cascade scenario. This scenario predicts two regimes in the kinetic energy spectrum: a direct cascade of enstrophy from the forcing scale towards small scales obeying a k^{-3} law, and an inverse energy cascade towards large scales with a theoretical slope of $k^{-5/3}$ (Kraichnan and Montgomery, 1980; Pedlosky, 1987). These power laws arise from simultaneous conservation of energy and enstrophy in 2D turbulence, at variance with what happens in three dimensions, where enstrophy is not conserved and energy cascades from large to small scales. The KK prediction has been investigated numerically by many authors. The inverse cascade of energy induces important consequences on the dynamics of 2D turbulence, and it is related to the formation of eddies and self-organizing character of the turbulent flow. In particular, the merging of same-sign coherent vortices, the primary interaction responsible for the evolution of the vortex population, is one component of the inverse energy cascade at large scales. Conversely, the direct enstrophy cascade takes place mainly through filamentation events (von Hardenberg *et al.*, 2000). In numerical simulations of 2D turbulence, the spectra are found generally steeper than predicted by theory (Benzi *et al.*, 1986; Pierrehumbert *et al.*, 1994; Schorghofer, 2000), most likely due to inversion of enstrophy cascade in elliptic regions of the flow (Ohkitani, 1991; Babiano and Provenzale, 2007). Moreover, spectral behaviors differ depending on initial conditions (Santangelo *et al.*, 1989) or forcing; factors which determine the dynamics of energetic, long-lived coherent structures participating in spectral transfers (Babiano *et al.*, 1997). Spectra steeper than k^{-3} have been found also in the reduced-gravity model (Larichev and McWilliams, 1991), and shallow-water systems (Farge and Sadourny, 1989). In 3D QG turbulence, Charney (1971) predicted an inverse energy cascade in the inertial range in case of the uniform stratification and postulated isotropy of the 3D spectra. However, numerical simulations of 3D QG turbulence show that energy spectra are not isotropic even in the presence of constant stratification (McWilliams *et al.*, 1994).

Results

Figure 6.11a shows the wavenumber spectra evaluated at 20m, 78m, 120m and 204m below the surface. In the surface layer the direct enstrophy cascade for $k > k_f$ has a spectral slope steeper than k^{-3}, consistent with numerical studies of 2D turbulence. This is related to the presence of mesoscale vortices, and differs from spectra found in regions populated by submesoscale fronts, characterized by a flatter slope (k^{-2}) owing to the strong filamentation associated with frontogenesis (Capet *et al.*, 2007b). The inverse energy cascade in Fig. 6.11a is reduced. This is due to the presence of a small Rossby deformation radius λ_I as investigated in the reduced-gravity model by Larichev and McWilliams (1991), where the turbulent evolution and therefore the inverse cascade, slows down on scales larger than λ_I. For comparison, spectra of kinetic energy of freely-decaying flow are enclosed (Fig. 6.11b), and also in this case spectral transfers are "frozen" above λ_I. At larger depths, the kinetic energy is significantly lower and the spectra do not display a clear power-law, suggesting that the enstrophy cascade and the role of the vortices are much reduced. The lack of classical inverse cascade is characteristic also for the baroclinic component of the kinetic energy at various depths (Fig. 6.11c). In the direct enstrophy cascade regime, the surface baroclinic energy spectra are flatter than barotropic ones, presumably owing to the presence of numerous, small baroclinic eddies (Fig. 6.5e and f). For the barotropic spectra, the scale of relevance is the external Rossby deformation radius, which is about $\lambda_o \approx 1000\,km$ in my simulations (see eq. 2.16). The barotropic component of the flow is populated only by the largest and the deepest vortices (Fig. 6.5f). Relatively low values of barotropic energy, and the fact that energy transfer does not reach the domain scale, is most likely due to numerical relaxation to initial profiles, which, keeping approximately the same stratification, prevents the transfer from baroclinic to barotropic modes, i.e., the vertical homogenization of the flow, as discussed by (Smith and Vallis, 2001) in the context of numerical simulations of spectral transfers between baroclinic and barotropic modes in an idealized ocean. In this scenario, the steady-state ratio of baroclinic to barotropic energy is high, and the energy in the baroclinic mode is peaked near the first baroclinic deformation wavenumber. Also in the ocean, where large-scale processes maintain the stratification, the integral length scale of eddies is proportional to the first Rossby radius of deformation, as observed in satellite measurements (Stammer, 1997).

6.2.3 Velocity distributions

Introduction

Probability density functions (PDFs) of horizontal velocities are an important ingredient for modelling particle dispersion processes. Stochastic models used to describe particle transport in geophysical turbulence, including oceanographic applications (Griffa, 1996) are based on first and second order moments (mean and variance) and on the assumption of Gaussian velocity departures from the local mean velocities. However, analyses of subsurface floats in the ocean in regions of strong mesoscale activity (Bracco *et al.*, 2000d; LaCasce, 2005; Isern-Fontanet *et al.*, 2006), suggest that coherent structures may produce the type of flow organization that yields deviations from normal statistics.

The non-Gaussian shape of the velocity PDFs, associated to the presence of coherent vortices, has been explored thoroughly in studies of point-vortex systems (Jimenez, 1996;

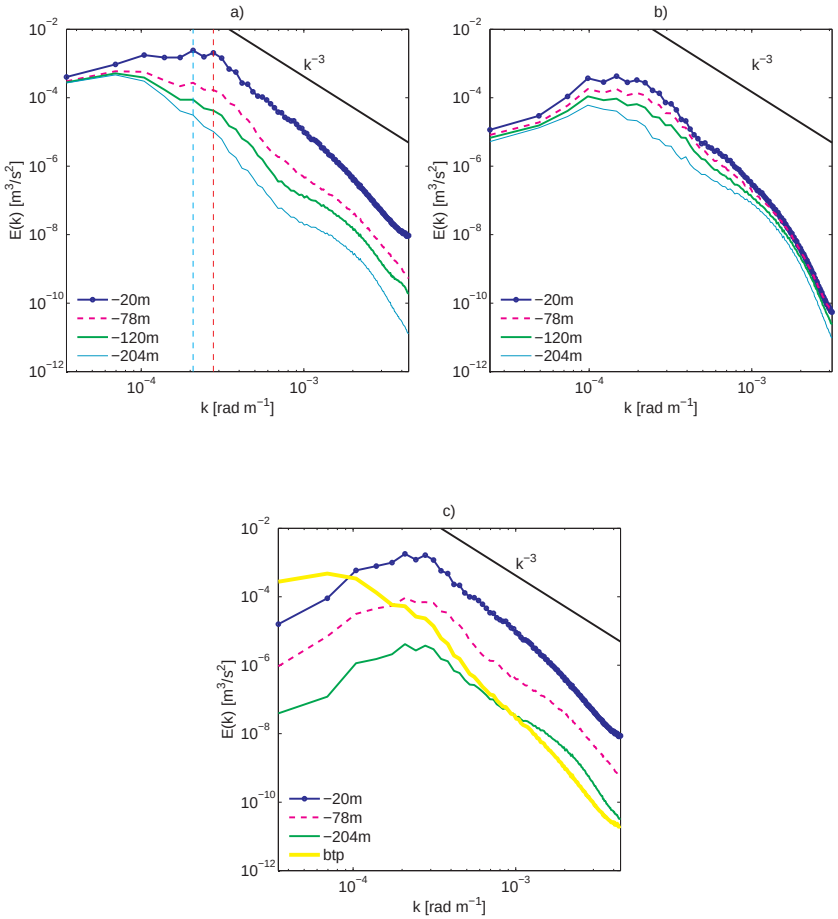

Figure 6.11: Spatial structure of the flow in the statistically stationary phase: (a) wavenumber spectra of total horizontal kinetic energy, averaged over 15 days; (b) wavenumber spectra of horizontal energy spectra for the freely-decaying simulations (Fig. 6.6a), averaged over 15 days; (c) wavenumber spectra of baroclinic (at different depths) and barotropic components (btp) of the kinetic energy, averaged over 15 days.

Min *et al.*, 1996; Weiss *et al.*, 1998), freely decaying (Bracco *et al.*, 2000c) and forced two-dimensional turbulence (Pasquero *et al.*, 2001). Owing to an excess of energetic events, velocity distributions are characterized by the presence of nearly exponential wings. Bracco *et al.* (2000c) studied the phenomenon by applying a separation into vortex-induced and backround-induced velocity field. They have concluded that the departure from Gaussianity of the total velocity field is non-locally generated by the far field induced by vortices. The velocity PDFs in the background field alone were Gaussian. This characteristics is observed provided the Reynolds number is high enough.

Given its importance for transport properties, it is worthwhile to explore shapes of velocity distributions for a stratified, forced eddy-dominated circulation to see whether the impact of QG vortices on flow statistics carry over to a more realistic situation.

Results

Since the velocity field is statistically isotropic, I have considered the distribution of the modulus of combined two horizontal components at different depths, normalized by the velocity r.m.s value. In the vigorous upper layers velocity PDFs deviate from Gaussian distribution (Fig. 6.12a), primarily due to pronounced tails, as it has been observed both for 2D-turbulence (Bracco *et al.*, 2000c) and oceanographic data alike (Bracco *et al.*, 2000d; LaCasce, 2005; Isern-Fontanet *et al.*, 2006). To pinpoint the source of non-Gaussianity, I will look at the velocity PDFs inside and outside vortices using Okubo-Weiss parameter (eq. 6.5). The analogy

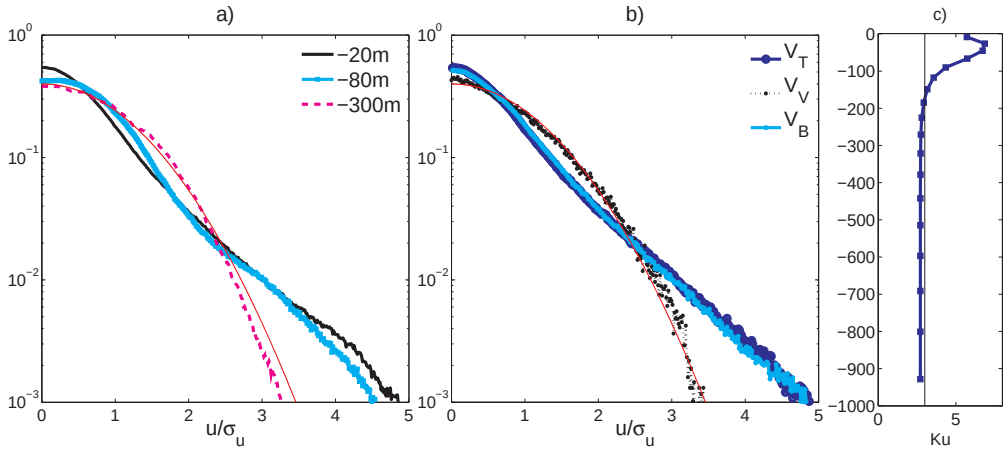

Figure 6.12: (a) Normalized PDFs of horizontal velocities at 20m, 80m and 300m averaged over 20 days. The thin line represents a Gaussian. (b) Normalized PDFs of horizontal velocities fat 20m depth, inside vortices (V_v), outside vortices (V_B), and in the whole domain (V_T). The thin line represents a Gaussian. (c) The profile of horizontal velocity kurtosis averaged over 20 days.

of the results for the surface flow with the 2D turbulence is evident (Fig. 6.12a-c). Inside vortices, PDFs of horizontal velocity are nearly Gaussian, while in the background turbulence they are almost identical to those calculated for the whole domain, with long non-Gaussian tails. These characteristics can be attributed to a far-field velocity induced by the vortices, as shown by Bracco *et al.* (2000c). This is likely because of the abundance of small and strong vortices (see Fig. 6.4a), which are believed to be responsible for the exponential tails at large velocities (Bracco *et al.*, 2000d; Isern-Fontanet *et al.*, 2006). The 2D turbulence analogy is constraint to the surface layer; below 200m, where the kinetic energy is much lower (Fig. 6.3d) and the role of surface-dominated vortices is weak, the shape of velocity PDFs become narrower than that of Gaussian (Fig. 6.12a) and the kurtosis is slightly smaller than 3 (Fig. 6.12 c). Faster-than-Gaussian decay of velocity distributions have been observed in numerical simulations of turbulent flows and explained by an interplay of the timescales of external forcing and nonlinear processes inherent in the system (see Falkovich and Lebedev, 1997, and references herein.).

6.3 Horizontal transport from a Lagrangian perspective

6.3.1 Introduction

A "natural" framework for studying mixing and dispersion in turbulent flows, dating back to the seminal work of Taylor (1921), is the Lagrangian one. The Lagrangian description is based on an observer following the trajectories of fluid particles, which are moving mathematical fluid points of infinitesimal size but large compared to molecular dimensions as required by continuum assumptions (Salmon, 1998). Each particle may be identified by its originating position $\mathbf{X}_o$ at a reference time t_o. Flow properties are expressed as functions of the initial particle position and current time t. The instantenous position is $\mathbf{X}(\mathbf{X}_o, t)$, which evolves as

$$\frac{\partial \mathbf{X}(\mathbf{X}_o, t)}{\partial t} = \mathbf{u}_L(\mathbf{X}_o, t), \tag{6.7}$$

where $\mathbf{u}_L$ is an instantenous (Lagrangian) velocity. A fundamental relationship between Eulerian and Lagrangian frames of reference is

$$\mathbf{u}_L(\mathbf{X}_o, t) = \mathbf{u}(\mathbf{X}(\mathbf{X}_o, t), t), \tag{6.8}$$

that is, the Lagrangian fluid particle velocity is given by the Eulerian velocity field $\mathbf{u}$ taken at the instantenous particle position. For a meaningful Lagrangian statistics, a sufficient number of particles with a high degree of statistical independence should be tracked and included in ensemble averages. Statistical independence is achieved only approximately as each particle evolves in the same velocity field. In the ocean, analysis is performed on velocity data from satellite-tracked drogue drifters designed to follow the currents near the surface or at depth; extensive information can be found online at the following Web sites: Drifting Buoy Data Assembly Center (Atlantic Oceanographic and Meteorological Laboratory, Miami, Florida), http://www.aom1.noaa.gov/phod/dac/dac.html; Subsurface Float Data Center (Woods Hole, Massachusetts), http:// wfdac.whoi.edu. Lagrangian data are used to characterize transport properties related to mesoscale turbulence and to test possible parameterization methods. Turbulence parameterizations are crucial for ocean general circulation models (OGCM's), especially when used in climate applications, where the size of the domain and the time span of interest are so large that vortices are usually not resolved and the results rely heavily upon the correct representation of their effects on the simulated large-scale circulation. A class of parameterization methods widely used in oceanography is based on Markovian stochastic models describing the motion of single particles in turbulent flows referred to as Lagrangian stochastic (LS) models (Griffa, 1996; Veneziani *et al.*, 2004). In the regions of low mesoscale variability transport can be modeled by using a simple, one-dimensional "random flight" (Orstein-Uhlenbeck) model, where the two velocity components of the fluctuation field are independent and the position $\mathbf{x}$ and velocity $\mathbf{u}'$ evolve jointly as a stationary, Gaussian, Markovian process with a finite memory (Rodean, 1996). In the presence of energetic and coherent mesoscale features this approach has been proven too simple and inadequate; suitable parameterizations of turbulent processes in such a case are still under debate. The problem has been approached with 2D turbulence considered as a suitable paradigm for the interpretation of oceanic turbulence (Elhmaidi *et al.*, 1993; Provenzale, 1999; Reynolds, 2002). The population of vortices and filaments

in 2D barotropic and 3D QG turbulence has been shown to cause non-Gaussianity of velocity field, non-exponential autocorrelation functions and anomalous dispersion of particles carried by the flow (Provenzale, 1999; Pasquero *et al.*, 2001; Bracco *et al.*, 2004). None of those properties is accounted for by Orstein-Uhlenbeck process. The problems of non-Gaussianity and the non-exponential shape of the velocity autocorrelation were addressed by (Pasquero *et al.*, 2001) by adopting a two-component model, one associated with the strong coherent vortices and the other related to the more quiescent background; this approach, however, does not reproduce the occurrence of anomalous diffusion. The latter might be captured by considering first-order Lagrangian stochastic models where the effective diffusivity depends upon Eulerian velocity distributions (Reynolds, 2002). Long-term positive correlations and oscillatory behavior of velocity covariances in mesoscale oceanic turbulence can be also represented by modifying Lagrangian stochastic models with the introduction of a spin parameter (Veneziani *et al.*, 2004). A definitive answer to which model of mesoscale turbulence is the most appropriate cannot be given at this stage because not enough evidence from the real-ocean data are too sparse. However, numerical simulations of three-dimensional mesoscale eddies allow to investigate whether transport properties of two-dimensional turbulence still hold in a flow, which is one step closer to reality.

In my simulation, once the flow has reached a stationary state, 3 sets of 4096 pairs of neutral Lagrangian particles (or "floats") have been deployed on a uniform horizontal grid with 4km spacing at z= 0.5m, z=78m and z=204m depth, respectively. At deployment, pair members were separated in the horizontal direction by 0.25 km. The particles were integrated for 180 days with a time step of 2 hours, passively carried by three-dimensional velocity field (Fig. 6.13a); the Lagrangian velocities are obtained from Eulerian values at adjacent grid points by bilinear interpolation. The three-dimensional evolution of the simulated floats makes them different from drifters commonly used in oceanography: The latter are constrained to stay at a constant depth and therefore do not follow vertical motions (e.g., Swenson and Niiler, 1996). The average vertical position of floats does not practically change for floats deployed at 78m and 204m while for the surface set it drops monotonically to a value of z=-35m after 180 days; hence it is assumed that the vertical motion of the particles does not jeopardize a general qualitative comparison of simulated results with oceanographic data.

6.3.2 Lagrangian autocorrelation time

The energy levels for particle ensembles are not stationary (Figure 6.13b), but rather slowly oscillate around typical Eulerian values for a mean float depth. For the estimation of autocorrelation functions, the Lagrangian time series have been normalized to have stationary covariance (with constant first and second moments) by subtracting the mean and dividing by the standard deviation. Time series have also been averaged over one day to remove any high-frequency inertial band wave energy from the low-frequency motion of interest in this study (the following results do not change whether a simple mean of low-pass filtering with one or two-day window is employed). The ensemble-averaged Lagrangian velocity autocorrelation is then estimated according to:

$$R(\tau) = \frac{1}{T}\left\langle \frac{1}{\sigma_U^i} \sum_{t=0}^{T} \mathbf{u}_L^i(t) \cdot \mathbf{u}_L^i(t+\tau) dt \right\rangle, \tag{6.9}$$

where $< ... >$ indicates average over the particle set with members denoted by i, T is the length of the time series, τ is a time-lag and σ_U^i is the Lagrangian velocity variance. The function (6.9) assumes the value of unity at τ=0 and falls to zero as $\tau \rightarrow \infty$, provided only that the process $[\mathbf{u}_L(t)]$ has a finite memory. Generally, except when $\mathbf{u}_L(t)$ is itself a time derivative of a stationary random function, the decay of $R(\tau)$ is monotonic, with the integral timescale defined by

$$T_L = \int_o^\infty R(\tau) d\tau, \tag{6.10}$$

measuring the memory time in $\mathbf{u}_L(t)$.

Figure 6.13c shows the aurocorrelation estimated for all three sets of floats. The surface flows decorrelate on scales of the order of one day, while correlations in the deeper layers persist for long times. The curves of the two deeper float families develop negative lobes, characteristic also of deep ocean float trajectories (Griffa, 1996) and indicative of subdiffusive processes (e.g., Mariano *et al.*, 2000). In practice, the integral in (6.10) is performed on a finite time T. The sequence of estimates for T_L where the upper limit of the integral increases in steps of one day is summarized in Figure 6.13 c. Estimates for deeper floats do not converge but after reaching a maximum corresponding to the zero-crossing in $R(\tau)$, fall down due to the contribution of negative lobes in Fig. 6.13a. These maximum values (that is, integration of $R(\tau)$ over positive lags only) will provide an estimate of T_L (Brink *et al.*, 2000), which gives 1.3, 5 and 7 days at floats released at 0.5, 78 and 204m respectively. The values for subsurface T_L obtained here fall in the range observed in the oceanic regions characterized by mesoscale activity, which is typically 1-7 days, and the magnitude of the derived eddy diffusion coefficient, $\kappa = \sigma^2 T_L \sim 5x10^7\ cm^2/s$ is also realistic; the longer integral timescales at depth are likewise consistent with oceanographic observations: Estimates of $T_L \approx$ 1-2 weeks were found for floats drifting at a depth of a few hundreds meters (Griffa, 1996; Brink *et al.*, 2000; Poulain, 2001).

6.3.3 Absolute dispersion

A first measure of transport properties is provided by horizontal absolute dispersion which describes the time evolution of the mean horizontal square distance travelled by each particle and is defined as:

$$A^2(t_o; t) = < |\mathbf{X}_i(t) - \mathbf{X}_i^o|^2 >, \tag{6.11}$$

where angular brackets indicate average over all the particles released at a given vertical level at t_o, and $\mathbf{X}_i(t)$ is the position of the i-th particle at time t after deployment. For statistically stationary flows, A^2 depends only on $t - t_o$, and if homogeneity is also satisfied, two characteristic regimes can be distinguished (Taylor, 1921). At sufficiently small times ($t \ll T_L$) absolute dispersion is ballistic, i.e., it depends quadratically on time: $A^2 = 2KE^L t^2$, where KE^L is the average kinetic energy of the particle ensemble during the time interval $[t_o, t]$. For sufficiently long times ($t \gg T_L$) the velocities of the particles become uncorrelated and particle dispersion is Brownian, $A^2 = 2\kappa t$, where κ is the (constant) dispersion coefficient. The absolute dispersion curves are shown in Fig. 6.14a. For the float set released at -0.5 m and travelling in the surface layer, the dispersion curve shows both ballistic and Brownian dispersion at short ($t <$ 2 day) and long ($t >$ 20 days) times respectively. However, for the

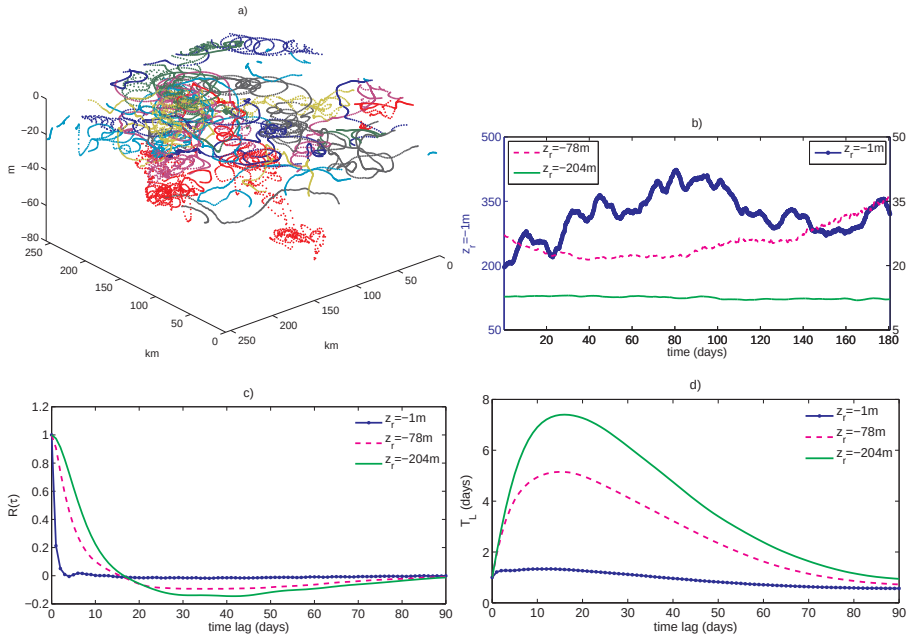

Figure 6.13: Example trajectories of floats deployed at the surface. Note the red tracks near 150km indicative of trapping phenomena. (b) Time trace of Lagrangian kinetic energy (m^2/s^2) for 3 float sets released at different depths. (c) Autocorrelation function estimate of one-day averaged horizontal float velocities. (d) Lagrangian autocorrelation time calculated from (eq. 6.10)

oceanographic applications, intermediate times are of major importance as the ballistic regime is often unresolved by sampling techniques and the Brownian one is rarely obtained due to spatial and temporal inhomogeneities of the large-scale circulation. At intermediate times, an anomalous dispersion of simulated surface floats appears, reminiscent of $A^2 \sim t^{5/4}$ law observed in vortex-dominated forced-dissipated barotropic (Elhmaidi *et al.*, 1993; Provenzale, 1999) and three-dimensional QG flow (Bracco *et al.*, 2004). Elhmaidi *et al.* (1993) related the presence of the anomalous regime to the presence of coherent structures: Owing to the strong vorticity gradients (or potential vorticity in stratified flows) at their edges, vortices act as transport barriers (Elhmaidi *et al.*, 1993; Provenzale, 1999). Particles can enter a vortex only during its formation phase, and can exit from it mainly during vortex merging and filamentation. Particles can thus be trapped in vortices for long periods of time, and their motion is characterized by a fast rotation inside a vortex and a longer-term displacement due to the motion of the vortex itself. At intermediate times particles are often found in the hyperbolic regions outside the vortices where they are subjected to long "flights" possibly responsible for $A^2 \sim t^{5/4}$ behavior (Elhmaidi *et al.*, 1993). A map of particle positions projected on the horizontal plane (Fig. 6.15 a) shows that indeed particles concentrate near circulation cells on timescales of several T_L. However, at later times particles tend to accumulate at the cores of the vortices (see also float tracks in Fig. 6.13a). This clustering is due to both the trapping properties of vortices and the divergent motion associated with the vertical velocity field (see Sect. 6.1.4 and Sect. 6.4). Such effects are absent in the non-divergent case of

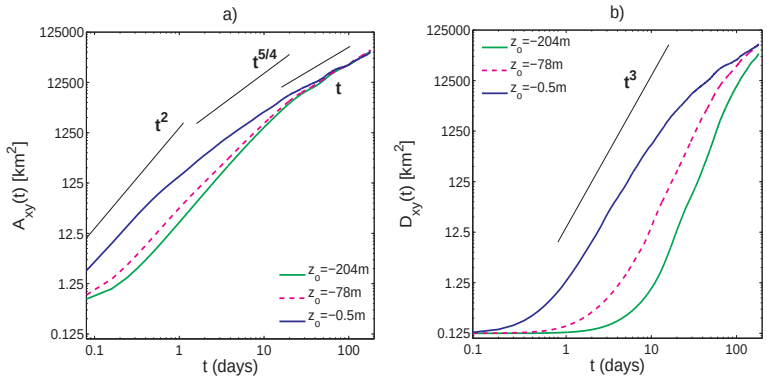

Figure 6.14: Absolute (a) and relative (b) dispersion of Lagrangian particles initially released at depths of 0.5m (blue solid line), 78m (red dashed line) and 204m (green solid line).

2D turbulence where the particles spread in homogeneous manner on time scales comparable to the typical lifetime of the vortices (Elhmaidi *et al.*, 1993; Provenzale, 1999). In sum, the transport properties of near-surface vortex dominated flows is very similar to that of 2D turbulence; thus the parameterizations built upon them (Pasquero *et al.*, 2001; Reynolds, 2002) can be considered relevant for a more realistic representation of oceanic turbulence obtained by integrating the primitive equations. On the other hand, the anomalous regime is practically absent at greater depths (Fig. 6.14a) where on longer times diffusive transport prevails (Fig. 6.14a) and the distribution of particles become homogeneous (Fig. 6.15b).

6.3.4 Relative dispersion

A measure of mixing properties is relative dispersion:

$$D^2(t; t_o, d_o) =< |\mathbf{X_i}(t) - \mathbf{X_i}'(t)|^2 >, \tag{6.12}$$

which describes the time evolution of the average separation of particle pairs. Here $\mathbf{X}$ and $\mathbf{X}'$ are the positions of two initially nearby pair members separated by d_o and the brackets indicate average over all independent pairs. For 2D turbulence, provided that d_o is not too large, classical dispersion theories predict $D^2(t) \sim t^3$ when the separation is in the energy cascade range (Richardson, 1926), exponential separation in the direct enstrophy cascade and diffusive regime on very long timescales. Figure 6.14b shows relative dispersion computed at different depths: all three curves display an intermediate Richardson regime after few days of exponential separation and converge to a diffusive regime at late times (after about 100 days), as in numerical simulations of 2D barotropic and QG flows (Babiano *et al.*, 1990; Bracco *et al.*, 2004). The presence of non-zero divergence does not seem to modify the mixing properties of the vortex-dominated simulated flow. Oscillatory internal wave field is inefficient at mixing tracers; dispersion by internal-inertial waves appears only as a second-order Stokes drift effect, due to wave-wave interactions (Polzin and Ferrari, 2004), and through the interaction of the vertical diffusion and vertical shear of the wave field, which can be described by an "effective horizontal diffusivity" (Young *et al.*, 1982). However, both theoretical estimates (Young *et al.*,

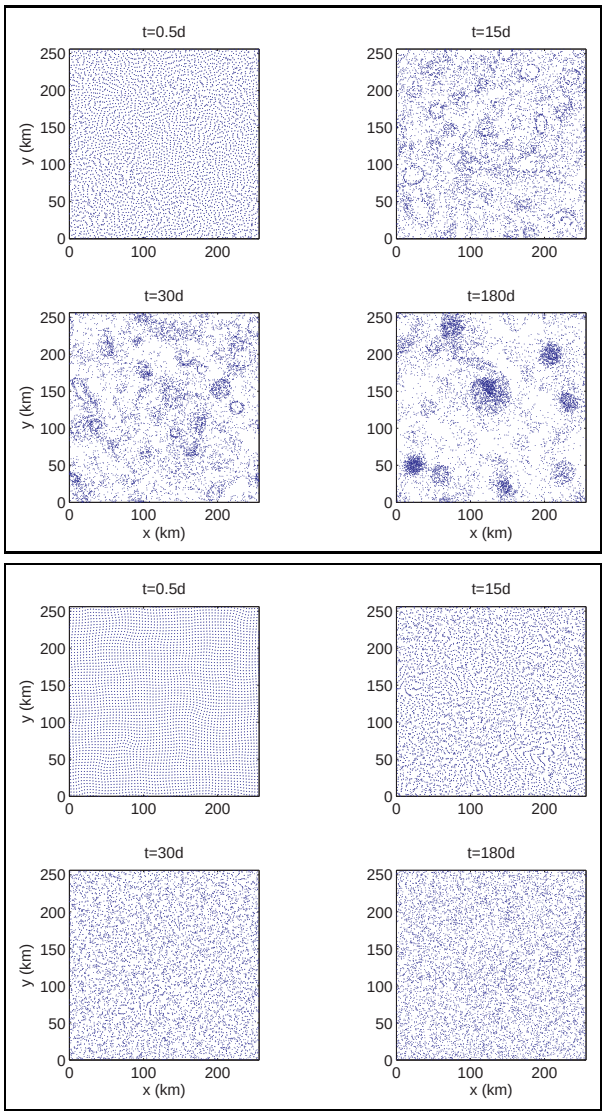

Figure 6.15: Particle positions projected on a horizontal plane at different instants of time: floats originated at the surface (top) and the depth of 204m (bottom) .

1982) and tracer-release experiments in the ocean (Polzin and Ferrari, 2004) suggest that internal wave dispersion is negligible on scales considered here and in the presence of vortical motions. Overall, the mixing properties of three-dimensional and divergent mesoscale flows in the numerical integrations discussed here appear to be analogous to those of 2D turbulence. This seems to be true also for ocean flows: An early exponential regime followed by power-laws with exponents of $2 - 3$ have also been reported for relative dispersion of surface ocean drifters (LaCasce and Ohlmann, 2003). This implies that the theoretical results obtained in the context of simpler 2D and QG turbulence can be extended to more realistic configurations. As pointed by LaCasce and Ohlmann (2003), this is most probably linked to the similarity of

wavenumber spectra (see Fig. 6.11a) - (Babiano *et al.*, 1997).

6.4 Vertical velocity and mesoscale eddies

6.4.1 Introduction

Observational estimates suggest that meso- and submesoscale fronts, eddies and filaments can drive significant vertical fluxes that affect local, regional and basin-scale biogeochemical budgets (Robinson *et al.*, 1993; McGillicuddy, 2001; Gargett and Marra, 2002). Indeed, mesoscale features can be the source of strong vertical velocities reaching 10^{-3} m/s, which correspond to excursions of the thermocline of 100 m/day, as found by using the omega equation (Sect. 4.4) and drifter measurements (Pollard and Regier, 1992; Allen and Smeed, 1996; Shearman *et al.*, 1999; V.-Belchi and Tintore, 2001; Barth *et al.*, 2004). The resulting vertical nutrient flux to the surface layers may be one order larger than in the highly-productive, coastal upwelling regions (Mann and Lazier, 1996). This has motivated a series of primitive-equation (thus vertical-velocity resolving, see Sect. 4.4) modelling studies focused on ocean fronts (Spall and Richards, 2000; Mahadevan and Archer, 2001; Levy *et al.*, 2001b; Mahadevan and Tandon, 2006). These works confirm that frontal vertical velocities can reach values up to 200 m/day in fronts (Levy *et al.*, 2001b; Mahadevan, 2006; Mahadevan and Tandon, 2006). In addition to mesoscale frontal meandering due to baroclinic instability (Levy *et al.*, 2001b), submesoscale processes such as frontogenesis, ageostrophic instabilities and nonlinear interaction of frontal dynamics with Ekman-induced circulation contribute to the generation of these strong vertical velocities (Mahadevan and Tandon, 2006; Capet *et al.*, 2007b,c). Notable asymmetry in the up- and downwelling velocities in favor of the latter were observed in both unforced and wind-forced fronts (Mahadevan, 2006; Mahadevan and Tandon, 2006; Capet *et al.*, 2007b). Frontal vertical velocities displayed a complex submesoscale structure (Levy *et al.*, 2001b; Mahadevan, 2006; Mahadevan and Tandon, 2006; Capet *et al.*, 2007b), more refined and concentrated near the surface when wind-forcing was applied (Mahadevan, 2006). These intense vertical circulations produced significant intensification of primary production: up to 30% at mesoscale front, depending on the degree of the initial nutrient depletion and its spatial distribution (Martin *et al.*, 2001) or even up to 100% when submesoscale and ageostrophic effects were accounted for (Levy *et al.*, 2001b).

All observational and modelling studies mentioned above focused on mesoscale fronts. The role of vortices, on the other hand, is understood only qualitatively; eddies are propagating features, and the spatio-temporal intermittency makes them elusive to shipborne sampling. Thus, the omega equation diagnosis of w, which requires synoptic maps of density for the calculation of geostrophic velocities is difficult to use. Moreover, the variability in time-series from moored Eulerian stations might be misleading due to interplay of spatial and temporal variations propagating in a given area (see the conclusions of Chapter 3). However, concurrent careful interpretation of Eulerian observations, drifting sediment traps, plankton recorders, ship transects and satellite data provide an observational evidence that eddies act to pump nutrients into the euphotic zone (McGillicuddy *et al.*, 1998; Sweeney *et al.*, 2003; Batten and Crawford, 2005; McGillicuddy *et al.*, 2007) and enhance the export of particulate organic carbon (POC) into deep layers and its futher sequestration in the sea bed (Siegel *et al.*, 1990; Sweeney *et al.*, 2003; Benitez-Nelson *et al.*, 2007). This has been explained with the eddy-pumping paradigm

(McGillicuddy *et al.*, 1998), schematized in Figure 1.3. According to this conceptual model, in the center of cyclonic eddies the pycnocline, and associated nutricline (a surface of strongest vertical nutrient gradient), may be several tens of meters closer to the ocean surface relative to the surrounding waters, injecting nutrients into the euphotic layer. Anticyclones, on the other hand, have no impact on biological productivity. A general tendency for an increased primary production in cyclonic eddies and weaker response in anticyclonic eddies has indeed been observed (Falkowski *et al.*, 1991; McGillicuddy *et al.*, 1998; Sweeney *et al.*, 2003), but the biological signal has appeared to be more intermittent than expected. The extention of this model involving a vortex life cycle and eddy-eddy interactions proved insufficient to explain the observed complexity of fixed-point biological response (Sweeney *et al.*, 2003) and submesoscale chlorophyll variability within mesoscale vortices (McGillicuddy *et al.*, 2007). On the other hand, a basin-wide estimate for the eddy-pumping fluxes (Martin and Pondaven, 2003) suggests that they cannot account for the nutrient flux required to sustain the observed levels of productivity in the subtropical gyres, vast open-ocean areas depleted in nutrients due to wind-induced, large-scale downwelling. These conundrums call for a more comprehensive study of eddy-induced vertical circulation. This is the goal of the present work.

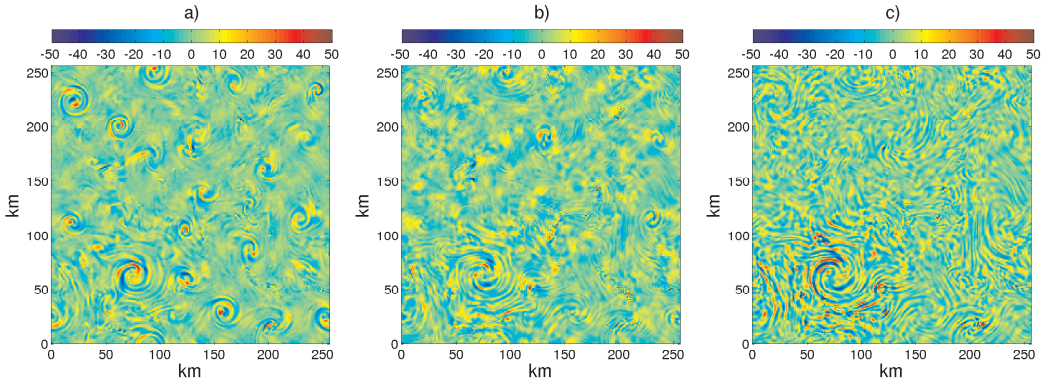

Figure 6.16: Instantaneous snapshot of the vertical velocity field corresponding to the vorticity field in Fig. 6.4a: at the depth of 20m (a), 80m (b) and 300m (c).

6.4.2 Vertical velocity field in the presence of vortices

The model vertical velocities in proximity of the wind-forced anticyclones are very intense, with typical values reaching several tens of meters per day (Fig. 6.16a-c, Fig. 6.17a-c and 6.18a) and absolute maxima of 100 m/day (Fig. 6.18b). These high values and fine structure persist despite a few-day time averaging is applied (one-day averaged fields are shown in Fig. 6.17). In vertical sections across vortices (Fig. 6.17c), upwelling and downwelling regions alternate. Two intensification depths are observed, one near the surface ($\approx$ 30m) and another at 350m (Fig. 6.18 a-b). A similar pattern of two-depth extrema of w has been reported in frontal simulations (Levy *et al.*, 2001b; Mahadevan and Tandon, 2006; Mahadevan, 2006), where the maximum near the surface was related to submesoscale processes, while the deeper one to the first baroclinic mode of instability of the meandering front.

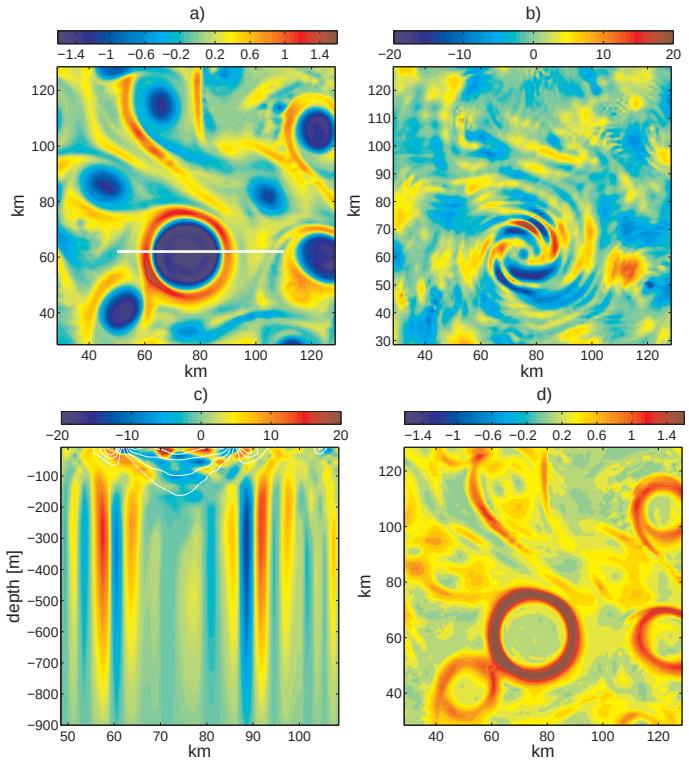

Figure 6.17: Structure of the vertical velocity field in the vicinity of a vortex: (a) Vertical component of the normalized relative vorticity at the surface, ζ/f (b) vertical velocity at a depth of 80 m in m/day; (c) vertical section of vertical velocity across the line indicated in panel (a). Isolines of ζ are superposed in white; (d) horizontal strain rate S in units of f. All fields are averaged over one day.

The distributions of vertical velocities are strongly non-Gaussian (Fig. 6.19a) in the surface layer, with the kurtosis reaching values up to $Ku \approx 40$ (Fig. 6.18c). Distributions remain non-Gaussian also inside the vortices (Fig. 6.19b). Exponential PDFs of vertical velocities have likewise been reported in simulations of submesoscale frontal dynamics by Capet *et al.* (2007b). Close to the surface p.d.f.s are skewed towards negative values (Fig. 6.18d), as observed in frontal circulations (Mahadevan and Tandon, 2006; Capet *et al.*, 2007b,c).

Although vortices are evidently the source of intense vertical circulation (Fig. 6.17a-c), the linear correlation coefficients between ζ, its vertical or horizontal gradients and w are less than 0.1 at all depths, indicative of the complexity of processes involved in generation of vertical motions. Moreover, I have found no strong correspondence between high magnitudes of w and the largest strain rates (see Fig.6.17 b and d) noted at ocean fronts by Mahadevan (2006); Mahadevan and Tandon (2006).

The vertical velocity field has a submesoscale structure evident both in physical space (Fig. 6.16 - 6.17) and wavenumber spectra presented in Figure 6.20a. This structure might result from ageostrophic centrifugal and anticyclonic ageostrophic instabilities at the cores of the vortices (Sect. 6.1.4), enhancing the fine complexity of the structure of w at fronts (Mahadevan

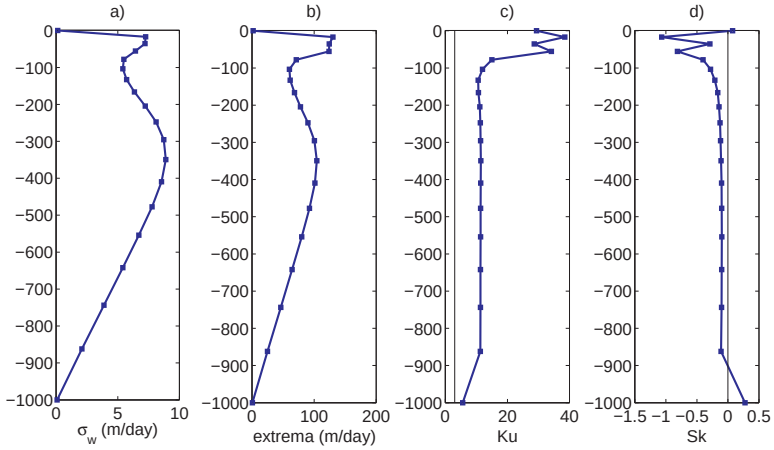

Figure 6.18: Vertical profiles of vertical velocity statistics, averaged over the horizontal domain and over a 20-day period: r.m.s fluctuation (a); absolute maximum (b); kurtosis (c); skewness (d).

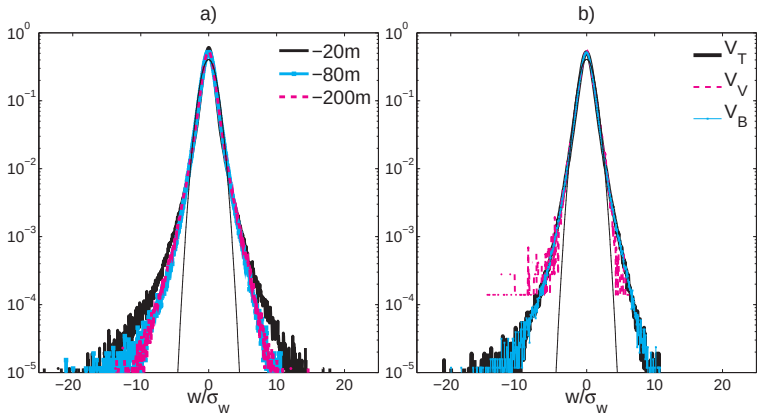

Figure 6.19: (a) Normalized p.d.f.s of vertical velocities at 20m, 80m and 200m averaged over 20 days. The thin line represents a Gaussian.(b) Normalized p.d.f.s of vertical velocities at 80m depth, inside vortices (V_v), outside vortices (V_B), and in the whole domain (V_T). The thin line represents a Gaussian.

and Tandon, 2006; Capet *et al.*, 2007c). Ekman circulation produces the symmetric pattern in Fig. 6.16a and the peak at k_f in spectral space (Fig. 6.20a); nonlinear interactions of mesoscale surface flow and Ekman transport, inducing a submesoscale pattern of w at wind-forced fronts (Mahadevan and Tandon, 2006) should be significant but they cannot be estimated easily in the present configuration. Vortex Rossby waves (VRWs) create spiral, alternating-sign w-features (Fig. 6.17 c and f), dipole-like structures in the cores of some vortices (top left of Fig. 6.16a), and tilted patches of w at the periphery of vortices as seen in the vertical sections shown in Fig. 6.17c (Montgomery and Lu, 1997; Wang, 2002).

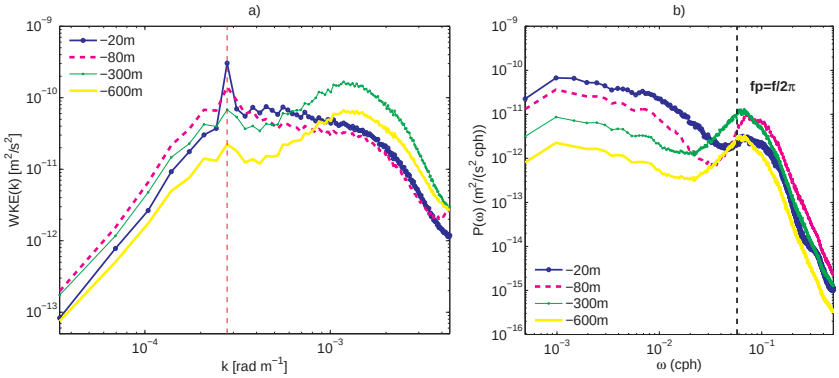

Figure 6.20: (a) Wavenumber spectra of vertical velocity at 20m, 80m, 300m and 600m, averaged over 20 days. The vertical dashed line marks the forcing wavenumber. (b) Frequency spectra at these depths, calculated over 60 days with a time step of 1h. The signal has been linearly detrended. The dashed line marks the inertial frequency.

Frequency spectra (Fig. 6.20b) suggest that near inertial-internal waves become a significant source of w in the interior, contributing to the deeper maximum in Fig. 6.18a-b. The inertial peak is shifted towards higher frequencies. The variability of the wave frequency has been addressed by Kunze (1985) in the context of weakly nonlinear wave-mean flow interactions. He has shown that the intrinsic frequency of inertial-internal waves propagating in a spatially inhomogeneous environment and in the presence of geostrophic shear adjusts locally according to the dispersion relation

$$\nu_o \approx f + \frac{\zeta}{2} + \frac{N^2 k_H^2}{2 f k_z^2} + \frac{1}{k_z}\left(\frac{\partial u}{\partial z} k_y - \frac{\partial v}{\partial z} k_x\right). \tag{6.13}$$

The most significant term in (6.13) is usually the first one, thus $\nu \approx f + \zeta/2 = f_{eff}$, which implies that alongside the planetary rotation, the waves experience advective rotation. Consequently, waves generated in anticyclonic regions have $\nu \approx f_{eff} < f$. These waves reflect at turning points in the horizontal direction as the horizontal component of wave vector approaches zero which occurs at boundaries of regions of negative ζ, and become trapped. On the other hand, waves generated in cyclonic regions where $f_{eff} > f$ and $\nu > f$ can easily propagate out and get recorded in uniformly distributed Eulerian stations.

The dispersion relation Eq. (6.13) is valid in a quasi-geostrophic regime ($Ro < 1$), thus the ageostrophic instabilities in vortex cores might introduce additional effects shifting the peak (by associated near-inertial motions, see Boccaletti *et al.*, 2007). Nonlinear wave-wave interactions and reflections from the bottom may also contribute (Rubenstein, 1984) as well as the surface flow divergence (Pollard, 1980). Moreover, the observed frequency might be further affected by the Doppler shift, which is a function of the wave incidence angle relative to the flow direction. A "blue shift" in the frequency spectra has been reported in both observational data (Pollard, 1980; Millot and Crepon, 1981; Kundu and Thomson, 1985) and numerical simulations (Klein and Hua, 1988). To visualize the vertical motions, space-time

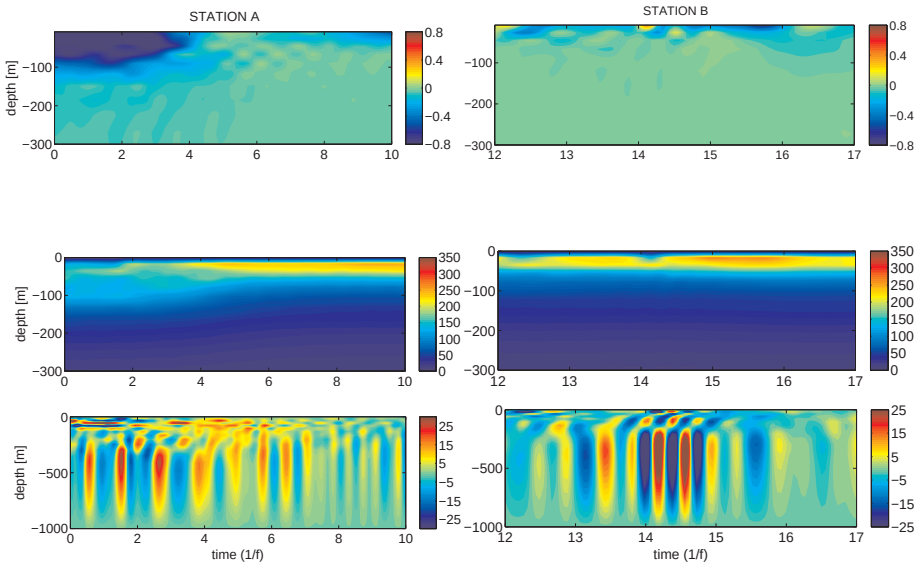

Figure 6.21: Hovmoller diagrams from two stations: one located in the core of a deep anticyclone (A) and another recording the passage of few shallow eddies (B). Time series were taken with 1h sampling interval. From top to bottom: relative vorticity ζ in units of f, Brunt-Väisäla frequency N in units of f and vertical velocity w (m/day).

$(z - t)$ plots (Hovmoller diagrams) of relative vorticity and vertical velocity are presented in Figure 6.21. Two stations are shown, A and B, where the passage of either large and deep, and small and shallow anticyclones has been recorded. The w-field in the interior shows signature of near-inertial phenomena. At the surface, it features variability on time scales approximately two times longer and attributable to VRWs and moving eddies. High amplitudes of near-inertial motions are associated with the vortices suggesting both generation, and wave-trapping observed in simulated mesoscale flows by Lee *et al.* (1994) and Klein *et al.* (2004). Significant momentum and energy transfer from mesoscale flows to the internal wave field has been inferred from oceanographic observations (Brown and Owens, 1981). In the presence of anticyclones, the stratification in the surface layer weakens and part of the kinetic energy leaks downward, providing a source for inertial-internal waves at mid-depths. Remarkably, shallow eddies (station B) generate strong vertical velocities far down in the interior. Divergence due to vortex Rossby waves can also modulate the transfer of near-inertial energy to the deeper layers (Gill, 1984). After the passage of coherent structures, near-inertial oscillations fade away within a few days, a typical time scale for the decay of inertial-internal waves in the ocean. The mechanisms for this decay are not yet well understood (Rubenstein, 1984; Rainville and Pinkel, 2005).

6.4.3 Vertical velocity dynamics

In the numerical model the vertical velocity field at a particular instant of time is calculated diagnostically from the flow divergence (see Sect. 4.4). Contributions from different dynamical

sources of w can be estimated by considering the following equation:

$$
\begin{aligned}
w(x,y,z) = & \overbrace{\frac{D\eta}{Dt}}^{\text{FREE-SURFACE}} - \\
& - \int_z^\eta \frac{1}{f+\zeta_1}\overbrace{\left[\frac{\partial\zeta_1}{\partial t} + u\frac{\partial\zeta_1}{\partial x} + v\frac{\partial\zeta_1}{\partial y} + w\frac{\partial\zeta_1}{\partial z}\right]}^{\text{AGEOSTROPHIC}} dz - \\
& - \int_z^\eta \frac{1}{f+\zeta_2}\overbrace{\left[\frac{\partial\zeta_2}{\partial t} + u\frac{\partial\zeta_2}{\partial x} + v\frac{\partial\zeta_2}{\partial y} + w\frac{\partial\zeta_2}{\partial z}\right]}^{\text{AGEOSTROPHIC}} dz - \\
& - \overbrace{\int_z^\eta \frac{1}{f+\zeta_1}\left[\chi_2\zeta_1\right] dz - \int_z^\eta \frac{1}{f+\zeta_2}\left[\chi_1\zeta_2\right] dz}^{\text{STRETCHING}} - \\
& - \overbrace{\int_z^\eta \frac{1}{f+\zeta_1}\left[\frac{\partial w}{\partial x}\frac{\partial v}{\partial z}\right] dz + \int_z^\eta \frac{1}{f+\zeta_2}\left[\frac{\partial w}{\partial y}\frac{\partial u}{\partial z}\right] dz}^{\text{TILTING}} + \\
& + \overbrace{\int_z^\eta \frac{1}{\rho_o(f+\zeta_2)}\left[-\frac{\partial}{\partial y}\frac{\partial\tau_x}{\partial z}\right] dz}^{\text{WIND STRESS}} + \\
& + \overbrace{\int_z^\eta \frac{A_H}{f+\zeta_1}\left(\frac{\partial^4\zeta_1}{\partial x^4} + \frac{\partial^4\zeta_1}{\partial y^4}\right) dz + \int_z^\eta \frac{A_H}{f+\zeta_2}\left(\frac{\partial^4\zeta_2}{\partial x^4} + \frac{\partial^4\zeta_2}{\partial y^4}\right) dz}^{\text{HORIZ MIXING}} + \\
& + \overbrace{\int_z^\eta \frac{1}{f+\zeta_1}\frac{\partial}{\partial x}\frac{\partial}{\partial z}\left(K_v\frac{\partial v}{\partial z}\right) dz - \int_z^\eta \frac{1}{f+\zeta_2}\frac{\partial}{\partial y}\frac{\partial}{\partial z}\left(K_v\frac{\partial u}{\partial z}\right) dz}^{\text{VERT MIXING}},
\end{aligned}
\tag{6.14}
$$

where for convenience I used a simplified notation $\zeta_1 = \partial v/\partial x$, $\zeta_2 = -\partial u/\partial y$, $\chi_1 = \partial u/\partial x$, $\chi_2 = \partial v/\partial y$. All components of eq. (6.14) are modulated by $(f+\zeta)^{-1}$, which can be large inside anticyclones where $|\zeta| \sim f$ and ageostrophic effects can get into play, generating the fine scale structure shown in Figure 6.17c-d. This explains why there is no simple correlation between w and ζ or its spatial gradients. I have estimated various contributions to eq. (6.14) using one-day averaged fields to filter near-inertial motions. Horizontal maps corresponding to Figure 6.16 at 17m are shown in Figure 6.22 and vertical sections corresponding to Fig. 6.17 are shown in Figure 6.23; the r.m.s fluctuations of the different terms as a function of depth are shown in Fig. 6.23f. The ageostrophic contribution, i.e., instantaneous vorticity changes and the advection of ζ (Fig. 6.22c and Fig. 6.23c), can reach 100m/day; and seem to be largely balanced by stretching (Fig. 6.22d and Fig. 6.23d), so the net horizontal pattern of vertical velocity (Fig. 6.16a) resembles the tilting term (Fig. 6.22e), the third largest term (Fig. 6.23f). Both the ageostrophic and stretching terms bear the structure of an azimuthal-wavenumber-four Rossby wave (Montgomery and Lu, 1997). The spiral pattern of the tilting terms can be related to the outward propagation of these waves (Graves *et al.*, 2006). Contribution of the free-surface reaches 1 m/s at most (Fig. 6.22a). The Ekman vertical velocity in a finite-Ro regime and for a spatially varying surface vorticity field has been obtained by Niiler (1969). Recalling his result, in case of spatially varying wind stress and relative vorticity, the nonlinear

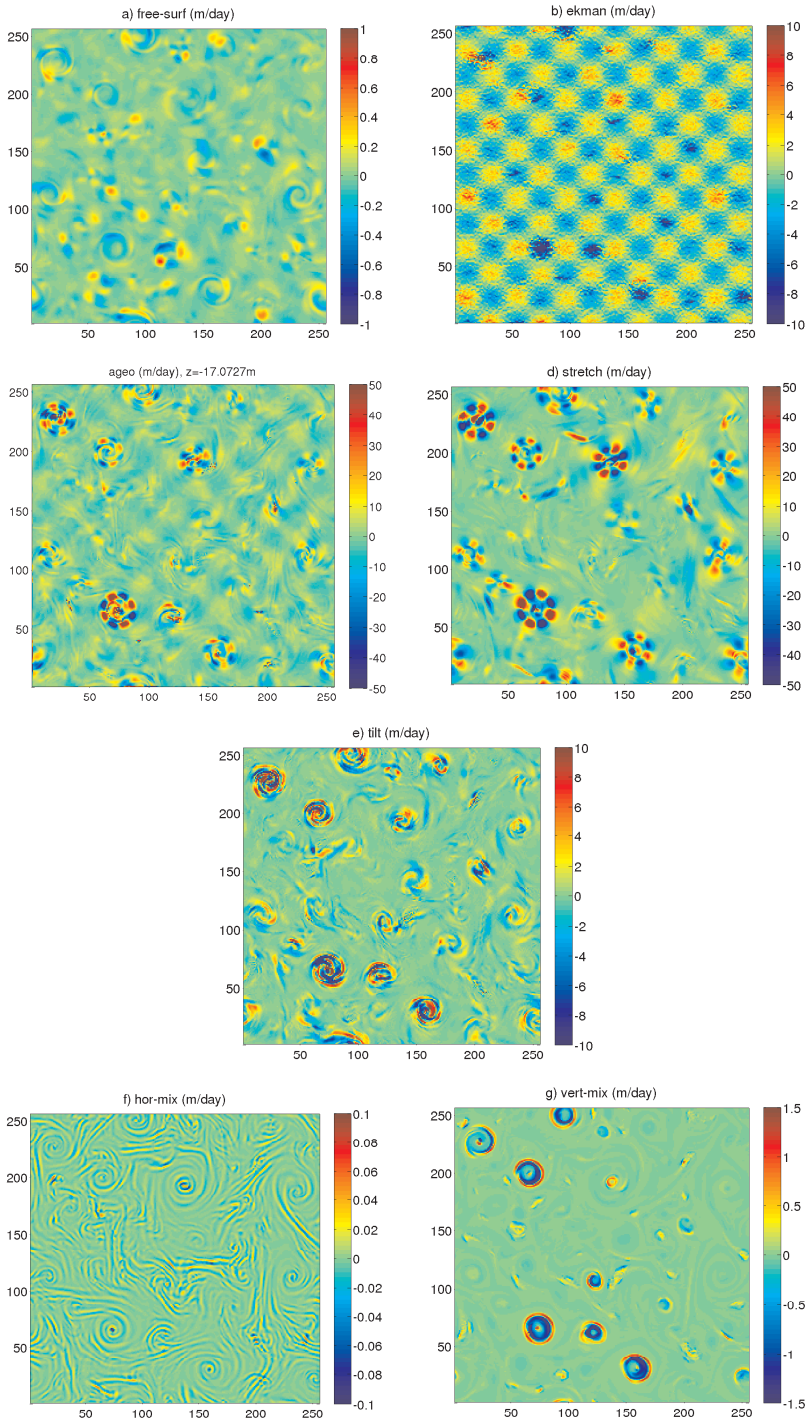

Figure 6.22: Maps of the terms in (6.14): (a) free-surface ($D\eta/Dt$), (b) surface and bottom stress curl (the latter is one order smaller than the first), (c) ageostrophic term at 17m, (d) stretching at 17m, (e) tilting at 17m, (f) horizontal mixing at 17m, (g) vertical mixing at 17m.

Ekman pumping/suction gives,

$$w_E = \int_z^\eta \frac{1}{\rho_o(f+\zeta_2)}\left[-\frac{\partial}{\partial y}\frac{\partial \tau_x}{\partial z}\right] dz - \int_z^\eta \frac{1}{(f+\zeta)}\left[\mathbf{u}_E \frac{\partial \zeta}{\partial \mathbf{x}}\right] dz \qquad (6.15)$$

where $\mathbf{u}_E = (u_E, v_E)$ is the Ekman flow. The first term in eq. (6.15) is explicit in eq. (6.14), and is mainly responsible for the positive feedback with negative vorticity regions (Thomas and Rhines, 2002). In fact, the negative contribution of wind-stress curl is strongest in the vicinity of vortices (Fig. 6.22a). The second term in eq. (6.15) is hidden in the advective part of the ageostrophic term and it has been found to be an important factor in generating upper submesoscale structures of w in the frontal simulations of Klein and Hua (1988) and Mahadevan and Tandon (2006) in case of spatially uniform wind stress. The horizontal mixing term (Fig. 6.22f) is three to four orders of magnitude smaller than the leading terms depending on depth (Fig. 6.23f). The vertical mixing, on the other hand, do reach the values of 1.5 m/s, but only locally at the centers of vortices (Fig. 6.22f and Fig. 6.23d) where stratification is lower and enhanced mixing occurs, parameterized by the KPP scheme (Sect. 5.7). The vertical mixing contribution is further discussed in Section 6.5.3.

6.4.4 Lagrangian view of vertical motion

Vertical velocities have significant impact on the motion of Lagrangian particles. Sample Lagrangian trajectories, released at a depth of 78 m and at the surface, are plotted in Figure 6.24a and b. Figure 6.25 shows the distributions of the vertical positions of particles released at the depth of 0.5m , 78m and 204m, at different instants of time, indicating that particles undergo large vertical excursions. Notably, the fraction of particles released at 78m that experience upwelling relative to the deployment depth grows with time. This result has interesting consequences for modelling marine ecosystem dynamics. Assuming that in the open ocean the euphotic layer depth is about 70m, over 50% of floats released at 78m reach 40m depth (where the subsurface maximum of phytoplankton concentration is often located) at least once during any 100-day period. The distribution of durations of each visit is shown in Figure 6.25d. Visits take 10 days on average, and two days (the modal value of the distribution) may be already enough to make upwelled nutrients available to phytoplankton (given that a typical phytoplankton growth rate is 1-2 day^{-1}, see e.g., Fasham, 1995) and possibly trigger a subsurface bloom. During the 180-day long integration, these particles perform 3 visits on average; the histogram of the number of visits is shown in Fig. 6.25d. Assuming that the results presented here are representative of open-ocean conditions, they may indeed rationalize the submesoscale pattern of extraordinary intense and sustained plankton blooms observed in eddies near Bermuda (McGillicuddy *et al.*, 2007). The role of vortices in float upwelling is largely confined to the surface layer. Out of 8192 floats released at $z = -204$m, only 46 upwelled above -100m and only 5 crossed the -70m isobath during their 180-day long integration. However, the configuration discussed here is idealized, while the real ocean is populated by coherent vortices also at depth, generated by other mechanisms with respect to those considered here (Tokos and Rossby, 1991; Gasparini *et al.*, 1999; Testor and Gascard, 2003; Thomas, 2007). These vortices might provide transport of nutrients under the surface layer where they can get captured and further upwelled by surface eddies, thus amplifying their effect.

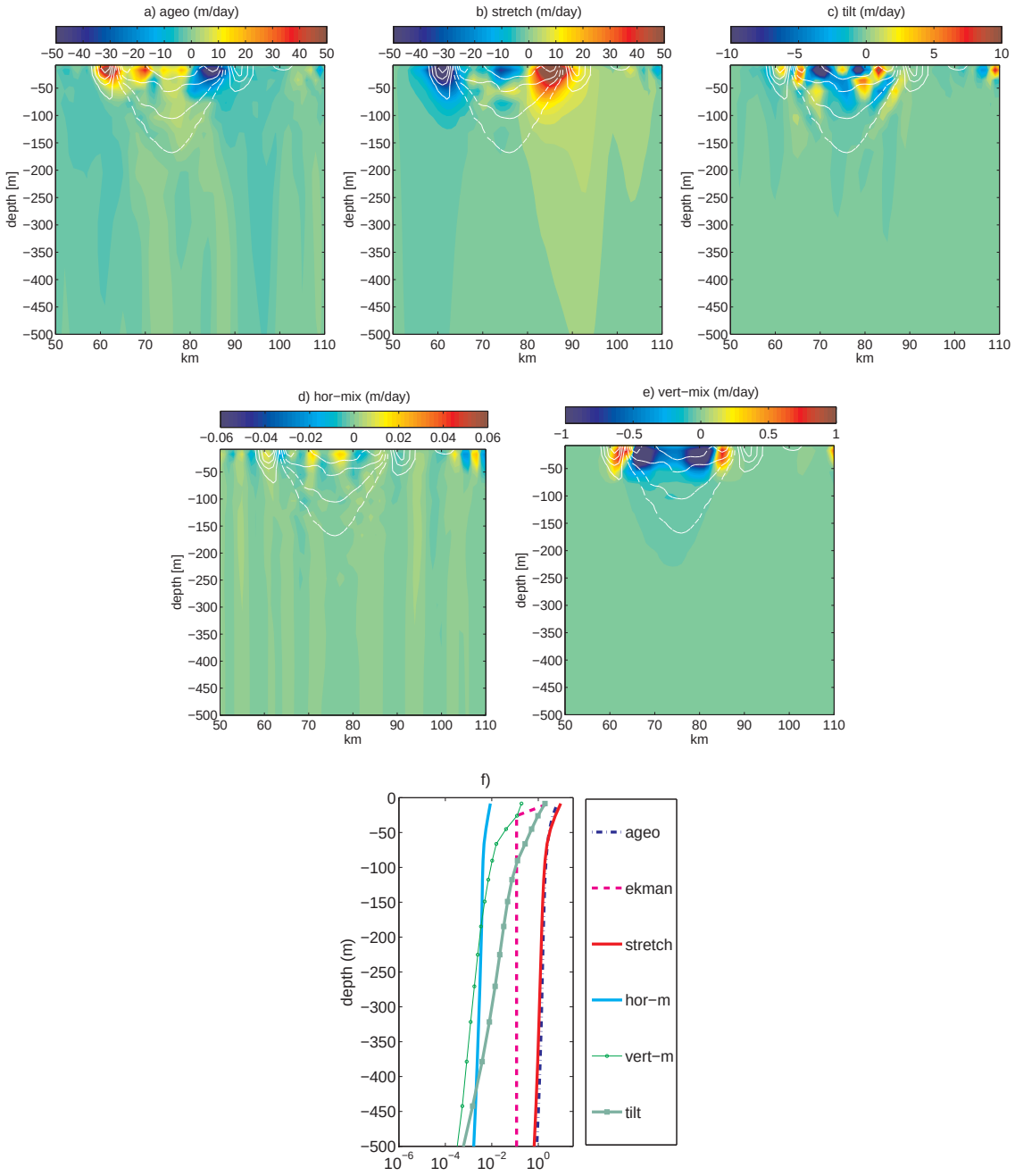

Figure 6.23: Sections of the terms in (6.14) in the vicinity of a vortex: (a) ageostrophic term, (b) stretching, (c) tilting, (d) horizontal mixing, (e) vertical mixing. (f) A vertical profile of the r.m.s contribution of the terms in eq. (6.14). For clarity, only the upper 500m are shown. Note the logarithmic scale.

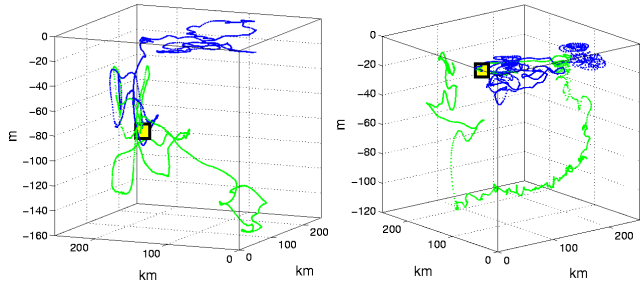

Figure 6.24: Example trajectories of initially close-by particle pairs released at 78m (left) and at the surface (right). Release positions are marked with squares.

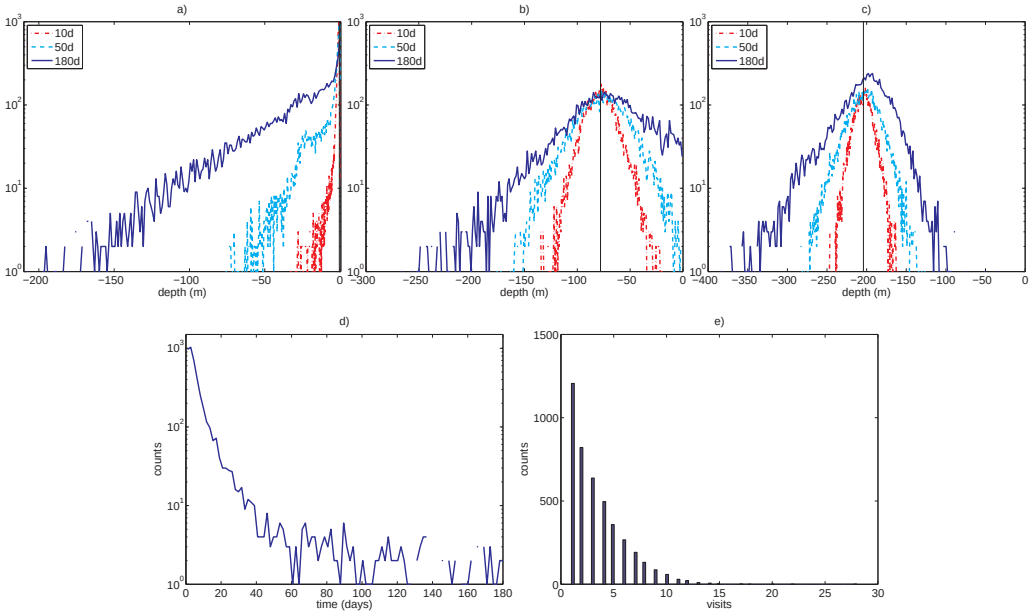

Figure 6.25: Histograms of vertical positions of floats released at 0.5m (c), at 78m (d) and 204m (c) at different times after release. The vertical line in each panel marks the depth of deployment. (d) Histogram of lengths of visits in the layer above 40m for the floats released at 78m. (e) Number of visits in the layer above 40m for the floats released at 78m.

6.5 Sensitivity study: mixed layer and vertical resolution

So far I have investigated an idealized set-up without a mixed layer at the top of the water column. In this section I will analyze how the presence of a mixed layer impact the dynamics and study the role of vertical resolution in the model. Three supplementary runs have been performed, V80-128, V20ML-128 and V80ML-128, as described in Section 5.9. In all of them the horizontal domain is reduced to 128x128 km^2, while the value of the internal Rossby radius of deformation is approximately the same as in the original simulation, that is $\lambda_I \approx$ 15-16km. Consequently, the free-surface (FS) effect, whose strength is inversely proportional to the ratio between λ_I and the horizontal domain size L, is expected to weaken. Nevertheless, the formation and evolution of the eddy field is qualitatively similar in all four experiments (Fig. 6.26). The wavenumber spectra of the horizontal kinetic energy are almost identical for the V80-128, V80ML-128 and V20ML-128 simulations (spectrum of V80ML-128 is shown in Fig. 6.27a). The weaker FS effect manifests itself in a well developed inverse cascade range, while in the enstrophy cascade the spectra are similar to the ones for V18-256 (Fig. 6.11a). The conclusions regarding the submesoscale vertical velocity structure (Fig. 6.27b) and its relation to eddies hold also for the other runs. The statistical differences between the various

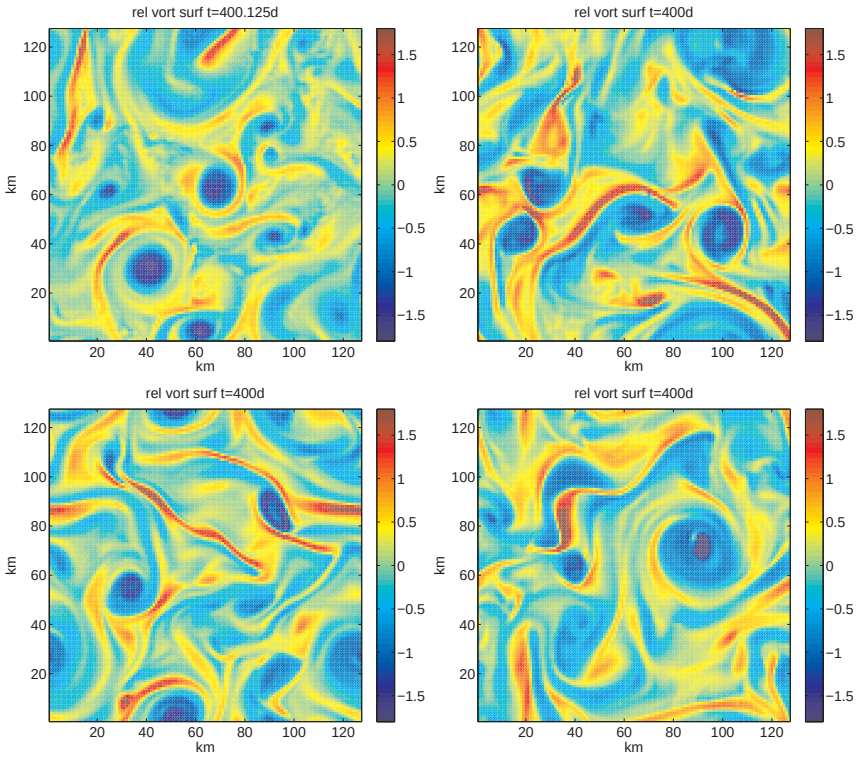

Figure 6.26: Instantaneous snapshots of the vertical vorticity field at -10m on the 400th day of the simulation: a cut-off piece of 128km x 128km domain of V18-256, (top left), V80-128 (top right), V20ML-128 (bottom left), V80ML-128 (bottom right).

flow configurations are discussed below.

6.5.1 Mixed layer

In the ocean, a homogeneous mixed layer (ML) in the ocean form primarily due to wind waves or convection generated by the loss of heat at the surface. At the base of ML, a density gradient (a pycnocline) separates the warmer and therefore lighter water of the upper layer from the denser water below. The buoyancy force that needs to be balanced to displace water particles from from one side of the pycnocline to another is proportional to the density difference across it, and energy must be supplied for vertical mixing to occur. Thus the pycnocline presents a barrier to vertical transport and the effectiveness of the barrier increases with increasing density difference (Gill, 1982). The reduced transport hinders transmission of surface momentum to the fluid interior, and it is illuminating to examine how the introduction of the mixed layer influences dynamics of simulated eddies and associated vertical velocities. Additionally, the pycnocline barrier causes near-surface depletion of the nitrate used by the plankton for its growth, while the nutrient values are higher in the zone below it.

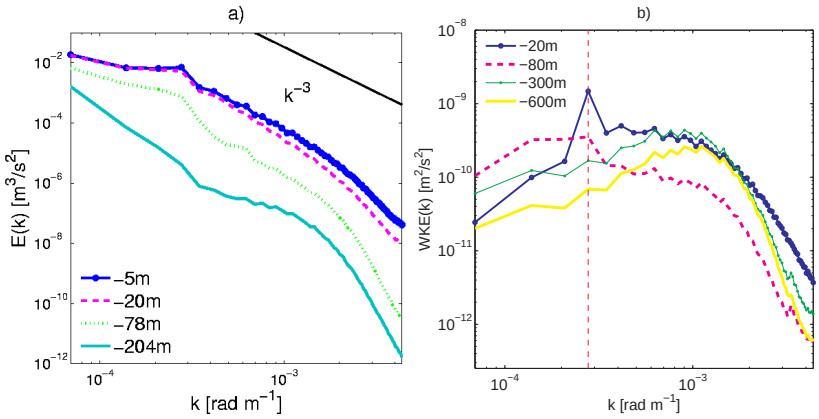

Figure 6.27: (a) Wavenumber spectra of total horizontal kinetic energy at 5m, 20m, 78m and 204m depth averaged over 20 days in the statistically stationary phase in the V80ML-128 simulation (compare with Fig. 6.11a); (b) Wavenumber spectra of vertical velocity at 20m, 80m, 300m and 600m depth for V80ML-128, averaged over 20 days. The vertical dashed line corresponds to the forcing wavenumber.

The two configurations, V80ML-128 and V80-128, allow for studying the dynamics with and without a 20-m mixed layer at the top of the water column (20m is a typical value of tropical water and mid-latitudes in the summer, Mann and Lazier, 1996, chpt. 3.2). A diurnal cycle in radiative fluxes has also been introduced. Stationary state profiles of temperature, salinity and density are shown in Fig. 6.28a-c, respectively, and the Brunt-Väisäla frequency is plotted in Fig. 6.28d. Below 20m the stratification is close to that used before (see Fig. 6.3) thus keeping the same value of $\lambda_I \approx 16$km. The temperature and salinity values are kept constant above 20m depth by relaxation to the initial profiles.

Introduction of the ML in V80ML-128 has caused a two-fold drop in the subsurface stratification compared to V80-128. This causes a redistribution of the horizontal momentum

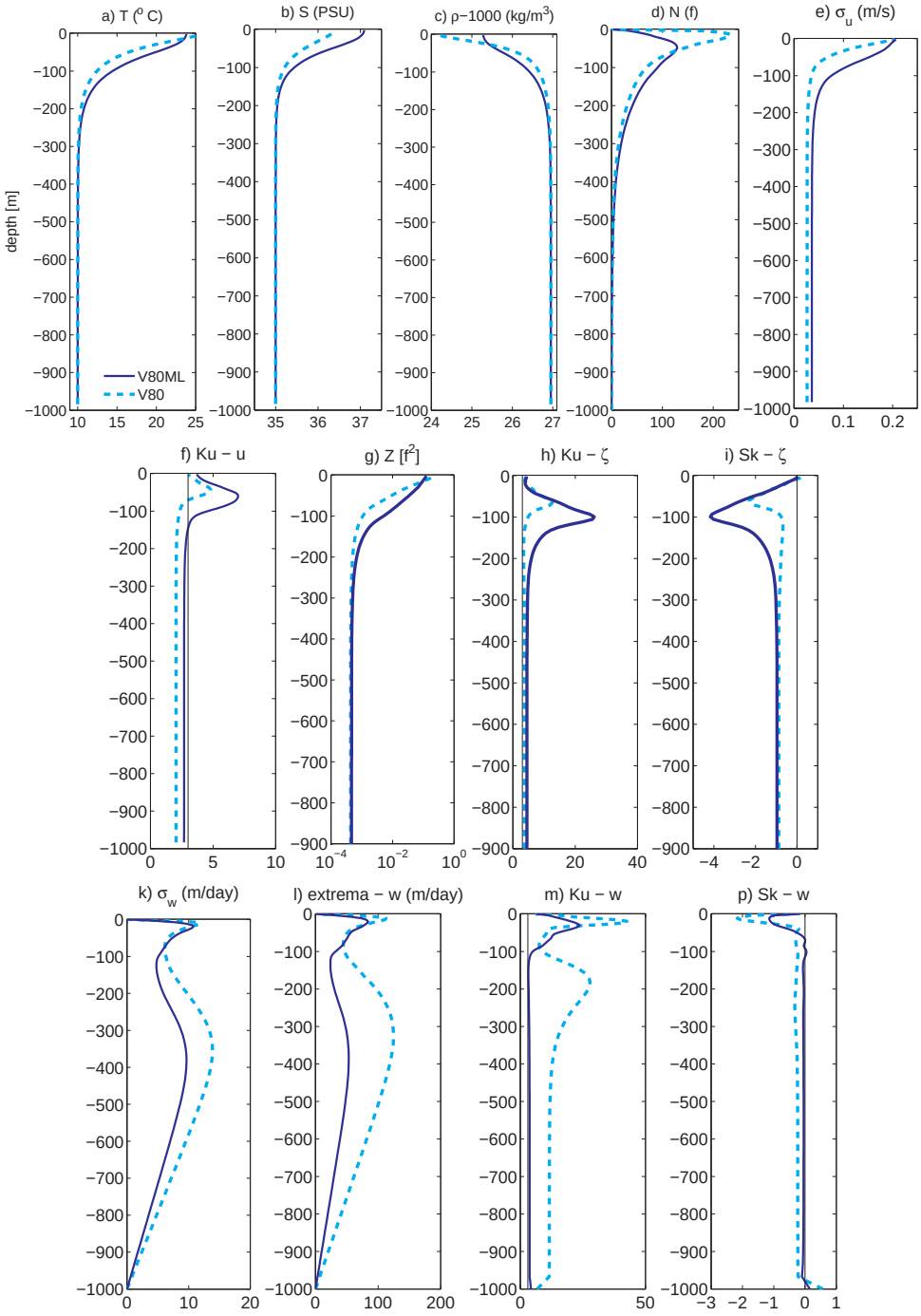

Figure 6.28: Vertical profiles of temperature for V80ML-128 (dark blue line) and V80-128 (dashed cyan line) (a), salinity (b), density (c) and Brunt-Väisäla frequency in units of f (d), r.m.s of the horizontal velocity (e) and kurtosis of the horizontal velocity (f), average enstrophy in units of f^2(g), relative vorticity kurtosis (h), vertical vorticity skewness (i), r.m.s of the vertical velocity (k), absolute extrema of w (l), kurtosis of vertical velocity (m) and its skewness (p). All profiles are obtained from averages over the horizontal directions and over 20-day period in the statistically-stationary phase.

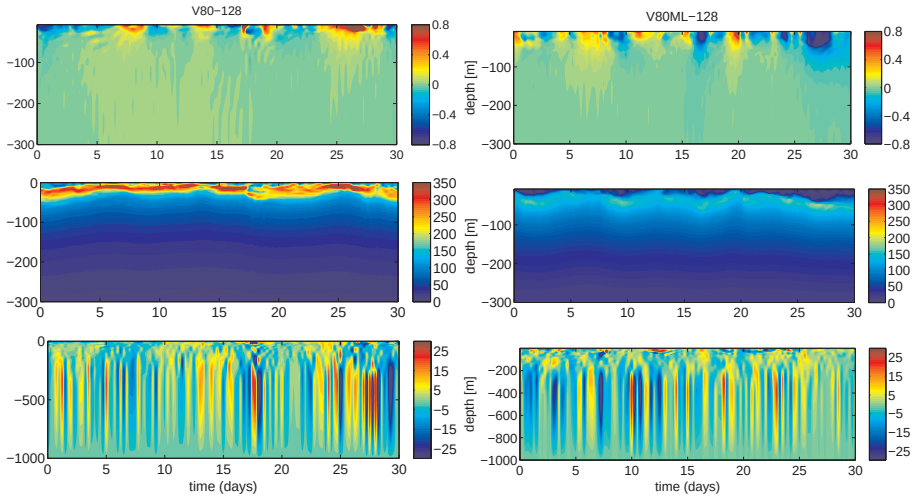

Figure 6.29: Hovmoller diagrams in the V80-128 and V80ML simulations recorded with 6h sampling intervals. From top to bottom: relative vorticity ζ in units of f in the upper 300m, Brunt-Väisäla frequency in units of f in the upper 300m, and vertical velocity w (m/day).

through the fluid column: subsurface horizontal circulation and relative vorticity penetrate deeper in V80ML-128 relative to V80-128. The flow in the latter case is indeed confined to a thinner layer by the strong stratification (Fig. 6.28e and g). Additionally, the presence of the mixed layer makes the surface horizontal flow strongly non-Gaussian and extends this non-Gaussianity to 120m depth, with respect to 100m in case of V80-128 simulation (Fig. 6.28f). With a mixed layer, the maximum of kurtosis occurs at 100m, 30m deeper relative to V80-128, and reaches much higher values: 28 versus 12 (Fig. 6.28h). The relative vorticity skewness is more negative when the mixed layer is present (Fig.6.28i). In the presence of the mixed layer the interior vertical velocities are weaker (Fig. 6.28k-l) and more Gaussian, while in the V80-128 simulation the kurtosis is still around 10 at 200m depth (Fig. 6.28m). In the presence of a mixed layer, vertical velocities are also less skewed towards negative values (Fig. 6.28p).

In order to better investigate these differences, I show Hovmoller diagrams of relative vorticity, Brunt-Väisäla frequency and vertical velocity in Fig. 6.29, obtained over a 30-day period with a sampling time interval of 6h. Coherent structures in the V80-128 simulation appear to be shallower relative to the situation when the mixed layer is present, consistent with the profiles of enstrophy and its kurtosis (Fig. 6.28g-h). The differences in the vertical velocity statistics are hardly visible; the temporal pattern of w is similar in the two cases. In sum, the main consequences of the introduction of a 20m-deep mixed layer is to extend the depth of penetration of the surface horizontal flow, to build up its intermittency and skewness at the base of the surface layer (around 100m depth) and to limit the deep vertical circulation. The question remains how the deepening of the mixed layer, either transient (as occurring in the ocean after a passage of a storm), or seasonal (as the mixed-layer depth can reach 200m depth in mid-latitudes during the winter) can influence the emergence of anticyclones, vorticity and vertical velocity statistics, and the structure of the flow.

6.5.2 Vertical resolution

Recent numerical works on mesoscale dynamics in the ocean have focused on the role of horizontal resolution (Levy *et al.*, 2001b; Mahadevan and Tandon, 2006; Capet *et al.*, 2007a). From these studies, a general conclusion is that the magnitude of the simulated vertical velocity varies inversely with the grid spacing, and that horizontal resolution of 0.5 - 1km is sufficient to resolve fine submesoscale patterns of w. However, the role of the vertical resolution on simulated submesoscale vertical velocities is yet to be explored. Notably, general circulation models, or even regional and eddy-resolving ocean models run in realistic configurations never have more than 20 layers in the first 1000m of the water column (e.g., Veneziani *et al.*, 2005; Chang *et al.*, 2006; Fennel *et al.*, 2006; Smedsrud *et al.*, 2006; Penven *et al.*, 2006, see also http://www.cara.psu.edu/climate/models-details.asp). I do address this problem by performing two experiments with the mixed layer and vertical resolution increased from 20 to 80 vertical layers, as described in Section 5.9.

The averaged stratification profiles for the numerical experiments V20ML-128 and V80ML-128 are visually identical (Fig. 6.30a-d). Yet, they are more finely resolved by the V80ML-128 simulation with respect to V20ML-128 and the exchange processes at the base of the mixed layer and between the surface layer and the interior are better represented. Increasing the vertical resolution in this range does not perceptibly alter the magnitudes and shape of the

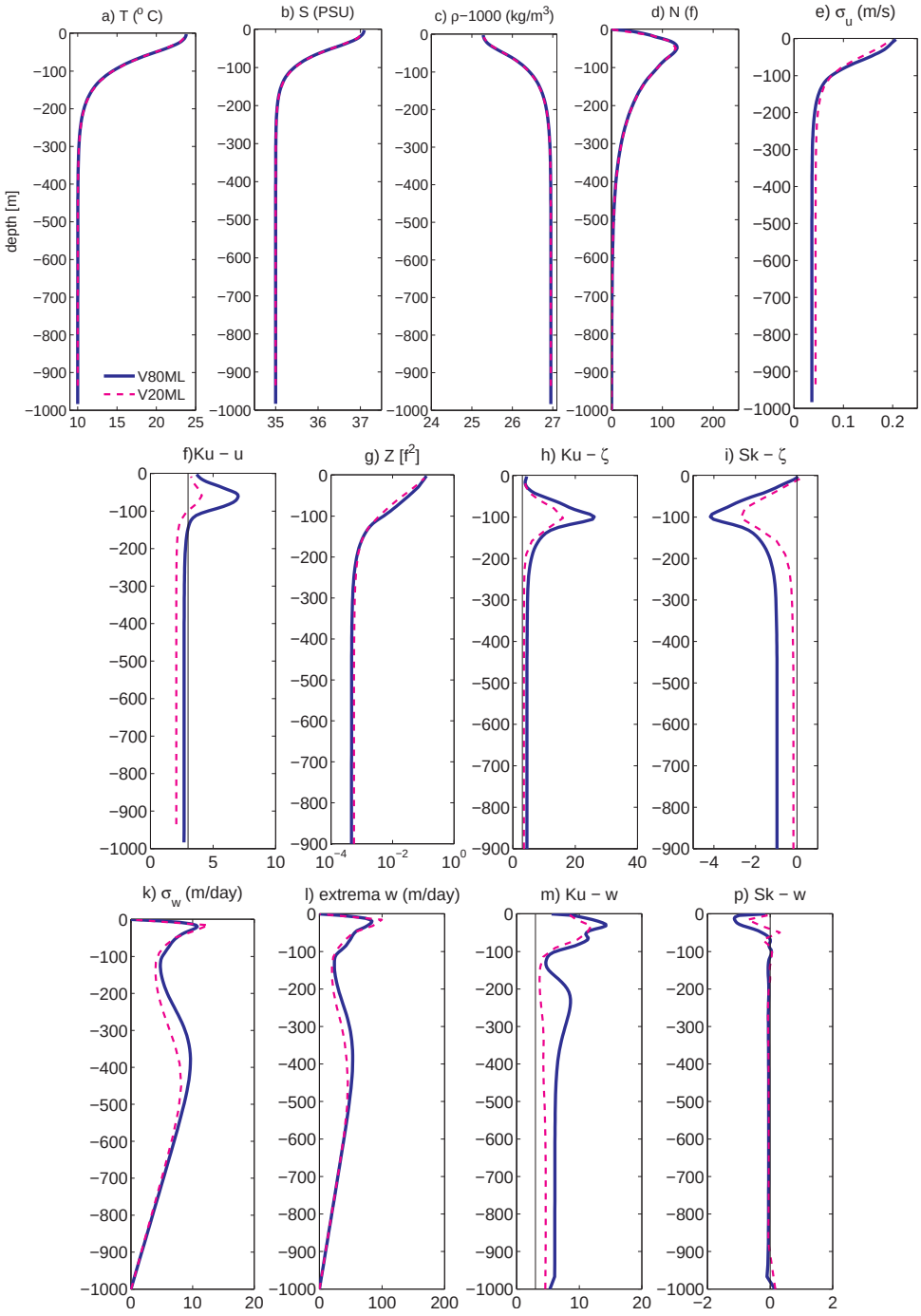

Figure 6.30: Vertical profiles of temperature for V80ML-128 (dark blue line) and V20ML-128 (dashed magenta line) (a), salinity (b), density (c) and Brunt-Väisäla frequency in units of f (d), r.m.s of the horizontal velocity (e) and kurtosis of the horizontal velocity (f), average enstrophy in units of f^2(g), relative vorticity kurtosis (h), vertical vorticity skewness (i), r.m.s of the vertical velocity (k), absolute extrema of w (l), kurtosis of vertical velocity (m) and its skewness (p). All profiles are obtained from averages over the horizontal directions and over 20-day period in the statistically-stationary phase.

profile of the horizontal circulation (Fig. 6.30e) but increases the kurtosis of (u, v) in the surface layer (Fig. 6.30f) as well as the kurtosis and negative skewness of the relative vorticity (Fig. 6.30h and i). Vertical motions display slightly larger magnitudes in the interior (Fig. 6.30h and i), have twofold increased kurtosis (Fig. 6.30m) and more pronounced skewness (Fig. 6.30p). Hovmoller diagrams for the V20ML-128 simulation are not presented as they are qualitatively identical to those for V80ML-128 (Fig. 6.29). In sum, the four-fold increased resolution does not introduce any significant changes in the flow behavior except for the increase of flow kurtosis and negative skewness. The impact on subsurface vertical mixing is discussed separately in the next section.

6.5.3 The problem of mixing

One significant difference between the different configurations concerns the strength of vertical mixing, parameterized by the KPP scheme described in Section 5.7. The problem will be discussed for the mixing of momentum (the conclusions for the mixing of tracers are analogous). The averaged profiles of vertical mixing coefficient of momentum, Kv, in m^2/s^2, for all forced simulations are shown in Figure 6.31a. The background value, K_v^o=10^{-6} m^2/s^2, has been augmented by the mixing scheme by three orders of magnitude; nevertheless the maximum value, $K_v \approx 5 \cdot 10^{-3}$ m^2/s^2, is still realistic for oceanic conditions (Large *et al.*, 1994). The increase in mixing in the interior is almost the same in all simulations and it is largely due to the internal wave contribution according to $K_v^w = \frac{10^{-6}}{N}$ $m^2\, s^{-1}$ (the interior value of N is approximately $10^{-5}\, s^{-1}$, that is 0.1 f, see Fig. 6.3d). Note however a drastic change of the near-surface values of K_v (Fig. 6.31b) in function of either the presence or absence of the mixed layer and the vertical resolution. Introduction of the mixed layer has increased the depth of the boundary layer d_B in eq. (5.16) and the diurnal cycle resulted in buoyancy fluxes negative for part of the day, thus activating the non-local transport in eq. (5.15). The increased resolution, on the other hand, represents more adequately these buoyancy fluxes through the water column as well as the momentum fluxes in the Ekman layer through the functions $G(\sigma)$ and w^* in eq. (5.16) as designed by Large *et al.* (1994, see his Fig. 2). From the analysis it appears that the only perceptible consequence of this is the increased importance of the vertical mixing contribution in eq. (6.14) for the V80ML-128 flow. The structure of all the terms in eq. (6.14) is very similar to the one presented in Fig. 6.22, except that the vertical mixing term at the vortex centers, which can account for vertical motions as large as 10 m/day, is one order higher than in V18-256.

The intensified subsurface vertical mixing in simulations involving the KPP scheme has also been noted by Mahadevan and Tandon (2006), though also in their case the general flow structure and behavior remained unaltered. Nagai *et al.* (2006), using a similar Ri-dependent scheme found vertical frontal velocities due to vertical mixing of 10 m/day, while Lee *et al.* (1994) have found that in general the vertical circulation at wind-forced fronts scales with both horizontal, and vertical mixing coefficients. The fact that the mixing contribution to w can be as high as 10m/day in the ML (and almost as large in the V80-128 simulation due to increased resolution) rises the question of how much of the differences between the simulations discussed in the two preceding sections can be a direct consequence of that, and whether and how it can be balanced by the ageostrophic and stretching or tilting contributions to w. Similar questions

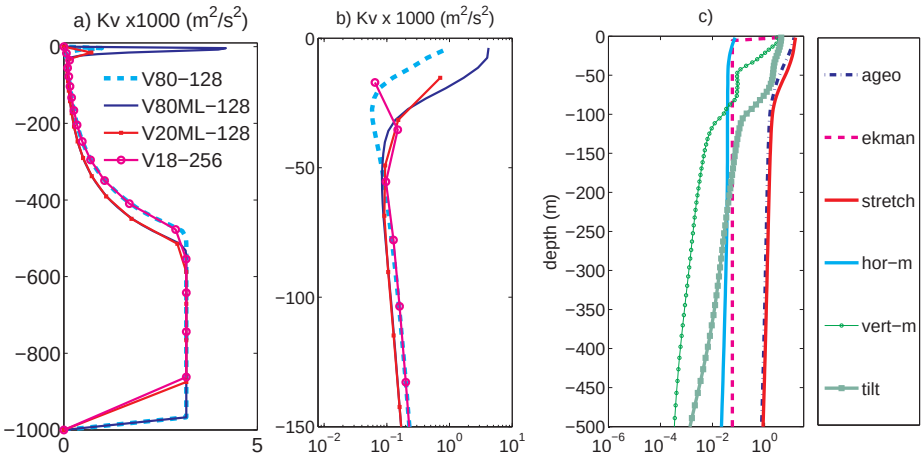

Figure 6.31: Vertical profiles of the vertical mixing coefficient, averaged over the horizontal domain and over a 20-day ensamble (a); and a surface close-up in the upper 150m (b). A vertical profile of r.m.s contribution of vertically integrated terms in eq. (6.14) in V80ML-128 simulation (c). For clarity, only upper 500m is shown.

have been posed by authors of the three cited works, but it is difficult (if possible) to answer this question due to the complexity of the nonlinear dynamics involved.

Thus, the computation of w is strongly affected by the numerical diffusivity. The magnitude of vertical diffusivities obtained in the simulations presented here are realistic for oceanic conditions (Large *et al.*, 1994) and the numerical scheme attempts at the best possible representation of the physical processes in action. There is a critical moment in the spin-up phase in all configurations used here, when instability of the stratified Ekman flow occurs, characterized by very strong vertical and lateral gradients in momentum and tracer fields. This phase is very liable to numerical blow-up. Switching off the KPP scheme implies using the high values of $K_v \approx 10^{-3}\ m^2/s^2$ in the entire water column, which is certainly less optimal and less realistic as the quiescent regions become too diffusive. On the other hand, it was not possible to achieve numerical stability with an alternative Mellor-Yamada scheme.

Chapter 7

Discussion

Coherent vortices densely populate many oceanic regions (Stammer, 1997) and play a relevant role in oceanic transport processes (Ferrari and Paparella, 2003; Cessi and Fantini, 2004), induce nutrient supply from the deeper to the surface layers and in consequence stimulate primary production, as well as export of organic matter to the sea bed (Sweeney *et al.*, 2003; McGillicuddy *et al.*, 2007; Benitez-Nelson *et al.*, 2007). However, the three-dimensional dynamics of open-ocean eddies as well as the details of their interactions with the marine ecosystem, are still largely unknown. In this thesis I have addressed some of these issues.

7.1 Mesoscale eddies and marine ecosystem behavior

In Chapter 3 I have shown an example of how horizontal advection can modify the behavior of ecosystem models. In case of a homogeneous ecosystem model displaying a limit cycle (self-sustained oscillations of biologocal and nutrient fields occurring for constant parameter values), inhomogeneity of environmental parameters combined with horizontal advection by a 2D vortex-dominated flow results in 1) masking of oscillatory behavior in Lagrangian time series of plankton abundance and 2) complete obliteration of limit cycles in Eulerian measurements. In the case of Lagrangian time series, the passage of the fluid parcel through areas with varying environmental conditions (mimicked by different values of the model parameters) leads to a modulation of the amplitude of the oscillations. In the case of Eulerian measurements, different fluid parcels pass by the measurement site. Even though each particle could have a remnant of self-sustained oscillations, different particles have a different history of alternance between regions with high and low exchange rates and thus reach the limit-cycle behavior with a different phase, making the oscillations undetectable. Notably, the variations induced in a fluid parcel due to alternance between different regions in space generate a temporal variation of the parameters in the homogeneous ecosystem model inside the fluid parcel itself.

This result is quite general, independent of which parameter of the model is spatially variable and of a particular formulation of the ecological model used. However, the degree to which the limit cycle is masked in Lagrangian time series depends on the degree of inhomogeneity of the environment through which the particles travel, as well as the ratio between the characteristic advection time and the rates of the biological processes involved. Notably, horizontal advection by mesoscale eddies features time scales (typically, few days) that allow it to strongly impact the biological processes.

Clearly, the fact that limit-cycle behavior can be disguised by advection does not imply that self-sustained oscillations are a real property of plankton dynamics in homogeneous conditions. A central conclusion of the work reported here is that the behavior of a homogeneous model and that of the same model in the presence of advection can differ significantly. Thus, inferences drawn from the analysis of homogeneous ecosystems should be taken with caution, and the

role of horizontal advection and dispersion should be taken into account as an important actor in ecosystem dynamics.

7.2 Three-dimensional dynamics of open-ocean vortices

In past years, vortex dynamics has been subject to intense investigation, usually in the framework of barotropic (2D), quasigeostrophic (QG) (e.g. McWilliams, 1990; Provenzale, 1999; Bracco *et al.*, 2004), or shallow-water (SW) turbulence (Polvani *et al.*, 1994; Graves *et al.*, 2006). However, 2D and QG flows fail to capture local ageostrophic effects (Giordani *et al.*, 2006) and all three approximations neglect the complex structure of the vertical velocity field. This is a cornerstone for this work and its main original aspect.

7.2.1 Problem setup

I employ the Regional Ocean Modelling System (ROMS) to study ocean mesoscale vortices in a configuration that is the closest I could find to the case of forced-dissipated 2D or QG turbulence - an idealized portion of the wind-forced open ocean - with the aim of highlighting similarities and differences between those simpler models and a more realistic, fully three-dimensional setting, and in particular to study vertical motions associated with the presence of vortices. The primitive-equation formulation employed is a reasonable approximation to oceanic flows at meso- and submesoscales (Salmon, 1998); The neglected nonhydrostatic effects (relative and Coriolis accelerations in the vertical momentum equation) do not contribute substantially to the average vertical fluxes at the mesoscales, as shown through comparative numerical experiments by Mahadevan (2006). Differential rotation is neglected at the scales of question (100-250km), as are the topographic effects, often unimportant far from land boundaries. The initial stratification was obtained by exponential fitting to sample oceanic profiles and a more realistic version with a surface mixed layer was also considered. Estimate of the first internal Rossby radius of deformation yielded $\lambda_I \approx$ 15-16km. The narrow-band wind-forcing I have used was a very idealized approximation to the ocean surface wind-stress field, however the formation of eddies did not seem to depend on a particular form of forcing used (vortices emerge also in a freely-decaying version of the configuration starting from random initial conditions).

7.2.2 General properties of simulated flow

The simulated flow in the statistically stationary phase is surface-intensified in the upper 100-150m where the average Rossby number is $R_o = \zeta/f \approx 0.3$. The flow is quasi-two dimensional and vertical velocities are typically three orders smaller than horizontal velocities. The dynamics is dominated by coherent anticyclonic vortices surrounded by positive-vorticity circulation cells, and immersed in a filamental background turbulence. Locally at the vortex cores and in the strong filaments $|R_o| \approx 2$. The vortical motion dominates the divergent component by one order of magnitude, near-inertial waves are undetectable in frequency spectra of horizontal kinetic energy but slow vortex Rossby waves (VRWs) with time scales of a few days, are conspicuous in the divergence field in the vicinity of coherent structures. The anticyclone dominance in the regime of a small internal Rossby deformation radius is related to the presence of these waves which induce net anticyclone strengthening in the straining flow, as indicated by studies formulated in a shallow-water framework (Graves *et al.*, 2006), a

phenomenon captured also by the reduced-gravity model as "free-surface effect" (Cushman-Roisin and Tang, 1990). The preponderance of anticyclonic eddies is observed also in the freely-decaying version of my simulations. To my knowledge, it is the only primitive-equation study that addresses the vorticity asymmetry property. The nonlinear, positive feedback between Ekman transport and negative vorticity regions (Niiler, 1969; Thomas and Rhines, 2002) further strengthens anticyclone dominance. Ageostrophic and weakly-stratified vortex cores are prone to ageostrophic instabilities (Molemaker and McWilliams, 2005), however, this fact do not hinder the formation of vortices from background turbulence. Ageostrophic instabilities have length scales of typically 1-10km, thus they are only marginally resolved in my configuration (Molemaker and McWilliams, 2005; Boccaletti *et al.*, 2007). On the other hand, the simulated regime lacks a strong divergence and stretching responsible for the preponderance of cyclonic vorticity at ocean fronts (Mahadevan and Tandon, 2006; Capet *et al.*, 2007a). Additionally, frontal circulations lack VRWs and the related anticyclone strengthening leading to anticyclone dominance present in the configuration studied here.

7.2.3 Horizontal dynamics and transport of primitive-equation eddies

The surface quasi-twodimensional dynamics of simulated eddies is similar to their barotropic and quasigeostrophic counterparts. The horizontal flow topology is captured by the Okubo-Weiss criterion, measuring the relative strength of vorticity and strain, which allows identification of vortex cores similarly to what is done in 2D turbulence (Elhmaidi *et al.*, 1993; Bracco *et al.*, 2000d; Babiano and Provenzale, 2007). Although they cover only up to 6% area of the surface flow, vortices house as much as 50% of the surface enstrophy and thus they practically control the overall circulation.

The wavenumber spectra of surface horizontal kinetic energy are reminiscent of those calculated for the reduced-gravity model in the regime of small λ_I, where the inverse energy cascade on scales larger than λ_I is undetectable (Larichev and McWilliams, 1991). The slope in the direct enstrophy cascade is steeper than k^{-3}, consistently with numerical studies of 2D turbulence (see e.g., Pierrehumbert *et al.*, 1994; Schorghofer, 2000; Babiano and Provenzale, 2007), of the reduced-gravity model (Larichev and McWilliams, 1991), and of shallow-water systems (Farge and Sadourny, 1989).

In the vigorous upper layers velocity PDFs deviate from Gaussian distribution, due to pronounced tails, as has been observed both for 2D-turbulence (Bracco *et al.*, 2000c) and oceanographic data (Bracco *et al.*, 2000d; LaCasce, 2005; Isern-Fontanet *et al.*, 2006). Inside vortices, distributions of horizontal velocity are nearly Gaussian, while in the background turbulence they are almost identical to those calculated for the whole domain. These characteristics can be attributed to a far-field velocity induced by the vortices, as shown by Bracco *et al.* (2000c) for a barotropic turbulent flow.

The Lagrangian integral timescale $T_L \approx 1$ day for floats released at the surface, and the magnitude of derived eddy diffusion coefficient, $\kappa = \sigma^2 T_L \sim 5x10^7\ cm^2/s$, falls in the range of observed oceanic values (Griffa, 1996). Absolute dispersion displays both ballistic and Brownian regimes at short ($t < 2$ day) and long ($t > 20$ days) times respectively. At intermediate times, an anomalous dispersion regime appears, reminiscent of $A^2 \sim t^{5/4}$ law observed in vortex-dominated forced-dissipated barotropic (Elhmaidi *et al.*, 1993; Provenzale, 1999) and three-dimensional QG flows (Bracco *et al.*, 2004). This feature is related the presence of

coherent structures since, owing to the strong vorticity gradients at their edges, vortices act as transport barriers (Elhmaidi *et al.*, 1993; Provenzale, 1999). On the other hand, due to the trapping effect of vortices and/or to non-zero divergence, at later times ($\sim$ 100 days) particles tend to accumulate at the vortex cores; such clustering phenomena are absent in nondivergent quasigeostrophic models.

Relative dispersion laws have proved to be robust: after a few days of exponential separation, an intermediate Richardson regime follows, and pair separation at late times converge to a diffusive regime, as in numerical simulations of 2D barotropic and QG flows (Babiano *et al.*, 1990; Bracco *et al.*, 2004), and similarly to oceanic flows sampled by surface ocean drifters (LaCasce and Ohlmann, 2003).

In sum, the transport properties of near-surface vortex dominated flows is very similar to those of 2D turbulence, though this analogy is constraint to the surface layer. At larger depths ($<$ 200m), the kinetic energy is significantly lower and vortices are much weaker. However, the vortex Rossby waves are still visible at these depths, likely generated by the overlying vortices. At these larger depths, horizontal kinetic energy spectra do not display a clear power-law, suggesting that the enstrophy cascade and the role of the vortices are much reduced, and the velocity PDFs lack the exponential tails. The correlations in horizontal velocities for floats released at 78m and 204m depths persist for long times and the autocorrelation curves of these deeper float ensembles develop negative lobes, characteristic also for deep ocean flows (Griffa, 1996) and indicative of subdiffusive processes (e.g., Mariano *et al.*, 2000). Estimates of T_L yield longer timescales of about seven days, a value typical for ocean drifters at depths of a few hundred meters (Griffa, 1996; Poulain, 2001).

7.2.4 Vertical velocity

Contrary to what would be expected from a simple "eddy-pumping" mechanism (McGillicuddy *et al.*, 1998), the vertical motions associated with the presence of vortices feature submesoscale intricacy as well as remarkable intensity.

Coherent anticyclones, filaments, vortex Rossby waves, as well as their interactions with Ekman circulation and inertial-internal waves generate a vertical velocity field with a complexity inaccessible to quasigeostrophic and shallow-water approximations. In the proximity of eddies, vertical velocities reach instantaneous values up to $\sim$100 m/day, that is one order of magnitude larger than in upwelling areas, and display a fine spatial horizontal structure (that is, high vertical kinetic energy occurs at scales smaller than vortex scales), similarly to what has been reported for oceanic fronts (Mahadevan and Tandon, 2006; Mahadevan, 2006; Capet *et al.*, 2007c). There are two depths of intensified vertical circulation: one near the surface ($\approx$ 30m) and another at 350m. The deeper maximum coincides with higher near-inertial wave activity, but the high values (several tens of m/day) and the fine structure of w persist even after temporal averaging over a few days, indicating a pronounced role of slow-time processes. Vertical velocity is not linearly correlated with relative vorticity, though clearly related to the presence of eddies. The PDFs of vertical velocities are non-Gaussian and they are characterized by long exponential tails as noted for submesoscale vertical circulations at fronts (Capet *et al.*, 2007c). The vertical velocity distributions are skewed towards negative values, which does not seem to be straightforwardly related to the prevalence of anticyclones; similar tendencies were reported for submesoscale frontal dynamics dominated by positive vorticity (Mahadevan, 2006;

Capet *et al.*, 2007c), and for both unforced fronts and fronts subjected to wind-stress. The mechanism for this negative skewness of w needs yet to be explained.

To elucidate the mechanisms generating the observed vertical motions, I have estimated various terms contributing to the flow divergence from which the w field is calculated in a primitive-equation framework. It appears that ageostrophic effects are important and vertical circulations result from the interplay of advection (including nonlinear interactions of vortices with Ekman flow), instantaneous vorticity changes, stretching and tilting, with an evident signature of vortex Rossby waves. Thus, the intense vertical circulation with fine three-dimensional structure is linked to ageostrophic motions and cannot be captured by simpler models like QG or SW turbulence.

These strong vertical velocities are responsible for large vertical excursions of Lagrangian tracers. In particular, frequent and sufficiently long excursions of particles released at 78m into subsurface layers suggest an important role of eddies in the communication between surface and deeper layers and thus in the establishment of vertical nutrient fluxes. The results of this thesis may indeed help to rationalize the chlorophyll maxima identified at the periphery of a warm-core ring in the Gulf Stream region (Hitchcock *et al.*, 1993), the observed intermittency of the biological response to the presence of eddies in the Sargasso Sea (Sweeney *et al.*, 2003) and the submesoscale variability noted in extraordinary intense and sustained plankton blooms observed in mode-water eddies near Bermuda (McGillicuddy *et al.*, 2007), which have proved elusive to the "eddy-pumping" explanation. In addition, the vertical distances covered by particles released at all depths reach several tens of meters in both (up and down) directions during the first ten days. Thus, one can expect also the export of organic matter to be strongly influenced by the vortices, as suggested by observations (Siegel *et al.*, 1990; Benitez-Nelson *et al.*, 2007). To quantify this effect, however, a study concerning finite-weight particles is needed.

7.2.5 Numerical issues

Much of the past numerical work has been carried out to assess the sensitivity of the mesoscale and submesoscale circulation to horizontal resolution (Levy *et al.*, 2001b; Mahadevan and Tandon, 2006; Capet *et al.*, 2007a). The effect of vertical resolution, on the other hand, has not been rigorously explored yet. I performed such a study here, and found that a resolution four times higher (from 20 to 80 vertical layers) does not introduce any significant change in the statistics of the flow and its structure, although it results in an increase of kurtosis and negative skewness of horizontal and vertical flow components.

One significant difference between the simulated flow in the different configurations concerns the vertical mixing parameterized by the KPP scheme. Both the presence of the mixed layer and the enhanced vertical resolution induce high values of the vertical mixing coefficient in subsurface layers. The resulting mixing rates are consistent with the model solution and they are realistic for oceanic conditions (Large *et al.*, 1994). I observe an increased vertical mixing contribution to the vertical velocity, which can reach 10m/day at the vortex centers, that is one order higher than in the original simulation. The dependence of simulated vertical circulation on vertical mixing parameterizations has also been noted in frontal simulations of Mahadevan and Tandon (2006), Nagai *et al.* (2006) and Lee *et al.* (1994) whenever the numerical scheme used was Ri-dependent. Still, the KPP scheme attempts at the best possible representation

of the physical processes in action and it is regarded as the most reliable among the schemes available in the ocean modelling community (e.g., Li *et al.*, 2001). For the configurations discussed here it was impossible to achieve numerical stability with an alternative Mellor-Yamada scheme during the flow spin-up; and from my experience, switching off the KPP scheme would imply necessity for setting elevated values of K_v in the entire water column, and in consequence the quiescent regions of the fluid would become too diffusive.

7.3 Concluding remarks

The motivation for this work has been the lack of a three-dimensional and high-resolution study of mesoscale ocean eddies and their role in the marine ecosystem, an unfortunate situation given the need of its adequate parameterization in global circulation models.

In this work I begin with showing an example of the interplay between horizontal advection and a plankton model which can lead to misinterpretation of ecosystem behavior as recorded by an Eulerian measurement of plankton abundance, thus highlighting the importance of the understanding of mesoscale eddy dynamics and of their impact in marine biophysical processes.

In the remaining part of the thesis, I address the problem of three-dimensional mesoscale vortex dynamics with a numerical study in the primitive-equation, idealized setup of a wind-forced open ocean. The flow is dominated by coherent anticyclones which have topological structure, appearance in wavenumber space, effects on horizontal velocity distributions and Lagrangian transport properties similar to quasigeostrophic turbulence.

On the other hand, the vertical velocity field associated with the presence of vortices, filaments, vortex Rossby waves, as well as their interactions with Ekman circulation and inertial-internal waves, displays a complexity inaccessible to quasigeostrophic and shallow-water approximations. This finding is the main innovative aspect of this thesis. Eddy-induced vertical velocities reach instantaneous values up to 100 m/day, that is one order of magnitude larger than in upwelling areas, display a fine three-dimensional spatial structure, and are responsible for large vertical excursions of Lagrangian tracers.

In light of recent observations on the critical role played by mesoscale eddies in increasing nutrient supply, primary production, and the modulating efficiency of the biological pump (McGillicuddy *et al.*, 2007; Benitez-Nelson *et al.*, 2007), the present results emphasize the complexity of submesoscale variability of wind-driven vortices and of the vertical velocity field and suggest that open-ocean eddies may exercise a higher degree of dynamical control over the marine ecosystem evolution than previously estimated. They suggest some topics for future work, namely:

- Interaction between plankton patchiness and mesoscale eddies. To rationalize the phenomenon, Abraham (1998) proposed a scenario based on horizontal stirring by mesoscale eddies leading to a direct tracer cascade of biological fields. In his explanation, the spectral slope of biochemical tracer variance depended on how fast reaction rates were with respect to the characteristic advection time scale. On the other hand, the primitive-equation, vertical-velocity resolving studies at fronts provide a different viewpoint. When nutrient injection within the euphotic layer occurs at submesoscale vertical circulation features, a related submesoscale nutrient and plankton variability emerges (Levy *et al.*, 2001b). It

would be interesting to determine the impact of three-dimensional mesoscale ocean eddies, and associated horizontal and vertical motions, on plankton distribution.

- A related question ensues: what is the relative role of horizontal and vertical transport by these eddies in maintaining and modulating biological productivity?
- Observations indicate differences in the phytoplankton community structure associated with different types of eddies (Sweeney *et al.*, 2003; Batten and Crawford, 2005). The impact of horizontal eddy transport on the plankton species composition has been addressed by Bracco *et al.* (2000b). It would be instructive to include the vertical dimension to this problem, which would elucidate the role of eddies in the export of particle organic matter to deeper layers, which is a function of the taxonomical structure of the marine ecosystem.

Bibliography

Abraham, E. (1998). The generation of plankton patchiness by turbulent stirring. *Nature*, **391**, 577–580.

Allen, J. S. (1973). Upwelling and coastal jets in a continously stratified ocean. *J. Phys. Ocean.*, **3**, 245–257.

Allen, J. T. and Smeed, D. A. (1996). Potential vorticity and vertical velocity at the Iceland-Faeroes Front. *J. Phys. Ocean.*, **26**, 2611–2634.

Allen, J. T., Smeed, D. A., Nurser, A. J. G., Zhang, J. W., and Rixen, M. (2001). Diagnosis of vertical velocities with the QG omega equation: an examination of the errors due to sampling strategy. *Deep-Sea Res. I*, **48**, 315–346.

Arakawa, A. and Lamb, V. R. (1977). Computational design of the basic dynamical processes of the ucla general circulation model. *Methods Comput. Phys.*, **17**, 174–267.

Babiano, A. and Provenzale, A. (2007). Coherent vortices and tracer cascades in two-dimensional turbulence. *J. Fluid Mech.*, **576**, 429–448.

Babiano, A., Basdevant, C., Legras, B., and Sadourny, R. (1987). Vorticity and passive-scalar dynamics in two-dimensional turbulence. *J. Fluid Mech.*, **197**, 241–257.

Babiano, A., Basdevant, C., Roy, P., and Sadourny, R. (1990). Relative dispersion in two-dimensional turbulence. *J. Fluid Mech.*, **214**, 535–557.

Babiano, A., Dubrulle, B., and Frick, P. (1997). Some properties of two-dimensional inverse energy cascade dynamics. *Phys. Rev. E*, **55(3)**, 2693–2706.

Barth, J. A., Hebert, D., Dale, A. C., and Ullman, D. S. (2004). Direct observations of along-isopycnal upwelling and diapycnal velocity at a shelfbreak front. *J. Phys. Ocean.*, **34**, 543–565.

Batten, S. D. and Crawford, W. R. (2005). The influence of coastal origin eddies on oceanic plankton distributions in the eastern Gulf of Alaska. *Deep-Sea Res II.*, **52**, 991–1009.

Beckmann, A., Boning, C. W., Brugge, B., and Stammer, D. (1994). On the generation and role of eddy variability in the central North Atlantic Ocean. *J. Geophys. Res.*, **99(C10)**, 20381–20291.

Benitez-Nelson, C. R., Bidigare, R. R., Dickey, T. D., Landry, M. R., Leonard, C. L., Brown, S. L., Nencioli, F., Rii, Y. M., Maiti, K., Becker, J. W., Bibby, T. S., Black, W., Cai, W.-J., Carlson, C. A., Chen, F., Kuwahara, V. S., Mahaffey, C., McAndrew, P. M., Quay, P. D., Rappe, M. S., Selph, K. E., Simmons, M. P., and Yang, E. J. (2007). Mesoscale eddies drive increased silica export in the subtropical Pacific Ocean. *Science*, **316**, 1017–1021.

Benzi, R., Paladin, G., Patarnello, S., Santangelo, P., and Vulpiani, A. (1986). Intermittency and coherent structures in two-dimensional turbulence. *J. Phys. A.*, **19**, 3771–3784.

Bigg, G. R. (2003). *The Oceans and Climate*. Cambridge University Press, Cambridge, UK.

Boccaletti, G., Ferrari, R., and Fox-Kemper, B. (2007). Mixed layer instabilities and restratification. *J. Phys. Ocean.*, page in press.

Bracco, A. and Pedlosky, J. (2003). Vortex generation by topography in locally unstable baroclinic flows. *J. Phys. Ocean.*, **33**, 207–219.

Bracco, A., Provenzale, A., and Scheuring, I. (2000a). Mesoscale vortices and the paradox of the plankton. *Proc. Roy. Soc. London B*, **267**, 1795–1800.

Bracco, A., Provenzale, A., and Scheuring, I. (2000b). Mesoscale vortices and the paradox of the plankton. *Proc. Roy. Soc. London B*, **267**, 1795–1800.

Bracco, A., LaCasce, J. H., Pasquero, C., and Provenzale, A. (2000c). The velocity distribution of barotropic turbulence. *Phys. Fluids*, **12(10)**, 2478–2488.

Bracco, A., LaCasce, J. H., and Provenzale, A. (2000d). Velocity probability density functions for oceanic floats. *J. Phys. Ocean.*, **30**, 461–474.

Bracco, A., von Hardenberg, J., Provenzale, A., Weiss, J. B., and McWilliams, J. C. (2004). Dispersion and mixing in quasigeostrophic turbulence. *Phys. Rev. Lett.*, **92(9)**, 084501–1–4.

Brink, K. H., Breadsley, R. C., J.Paduan, R.Limeburner, Caruso, M., and Sires, J. G. (2000). A view of the 1993-1994 California Current based on surface drifters, floats, and remotely sensed data. *J. Geophys. Res.*, **105(C4)**, 8575–8604.

Brown, E. D. and Owens, W. B. (1981). Observations of the horizontal interactions between the internal wave field and the mesoscale flow. *J. Phys. Ocean.*, **11**, 1474–1479.

Bruce, J. G., Johnson, D. R., and Kindle, J. C. (1994). Evidence for eddy formation in the eastern arabian sea during the northeast monsoon. *J. Geophys. Res.*, **99(C4)**, 7651–7664.

Canuto, C., Hussaini, M. Y., Quarteroni, A., and Zang, T. A. (1988). *Spectral methods in fluid dynamics*. Springer-Verlag, Michigan, U. S.

Capet, X., McWilliams, J. C., Molemaker, M. J., and Shchepetkin, A. F. (2007a). Mesoscale to submesoscale transition in the California Current System: Energy balance and flux. *J. Phys. Ocean.*, page submitted.

Capet, X., McWilliams, J. C., Molemaker, M. J., and Shchepetkin, A. F. (2007b). Mesoscale to submesoscale transition in the California Current System: Flow structure, eddy flux and observational tests. *J. Phys. Ocean.*, page submitted.

Capet, X., McWilliams, J. C., Molemaker, M. J., and Shchepetkin, A. F. (2007c). Mesoscale to submesoscale transition in the California Current System: Frontal processes. *J. Phys. Ocean.*, page submitted.

Cessi, P. and Fantini, M. (2004). The eddy-driven thermocline. *J. Phys. Ocean.*, **34**, 2642–2658.

Chang, P., Fang, Y., Saravanan, R., Ji, L., and Seidel, H. (2006). The cause of the fragile relationship between the Pacific El Nino and the Atlantic Nino. *Nature*, **443**, 324–328.

Chao, S.-Y. and Shaw, P.-T. (1996). Inizialization, asymetry and spindown of Arctic eddies. *J. Phys. Ocean.*, **26**, 2076–2092.

Charney, J. G. (1971). Geostrophic turbulence. *J. Atmos. Sci.*, **28**, 1087–1095.

Conkright, M. E., Locarnini, R. A., and coauthors (2002). World ocean atlas 2001. In D. L. Evans, C. C. Lautenbacher, and G. W. Withee, editors, *NOAA Data Center Internal Report 17*. NODC, http://www.nodc.noaa.gov/OC5/WOA01.

Cushman-Roisin, B. and Tang, B. (1990). Geostrophic turbulence and emergence of eddies beyond the radius of deformation. *J. Phys. Ocean.*, **20**, 97–113.

Davey, M. K. and Killworth, P. D. (1984). Isolated waves abd eddies in a shallow water model. *J. Phys. Ocean.*, **14**, 1047–1064.

Eady, E. T. (1949). Long waves and cyclone waves. *Tellus*, **1**, 33–52.

Edwards, A. M. and Brindley, J. (1996). Oscillatory behavior in a three-component plankton population model. *Dyn. Stabil. Syst.*, **11(4)**, 347–370.

Edwards, A. M. and Brindley, J. (1999). Zooplankton mortality and the dynamical behavior of plankton population models. *Bull. Math. Biol.*, **61**, 303–339.

Edwards, A. M. and Yool, A. (2000). The role of higher predation in plankton population models. *J. Plankton. Res.*, **22(6)**, 1085–1112.

Elhmaidi, D., Provenzale, A., and Babiano, A. (1993). Elementary topology of two-dimensional turbulence from a Lagrangian viewpoint and single-particle dispersion. *J. Fluid Mech.*, **257**, 533–558.

Ertel, H. (1942). Ein neuer hydrodynamischer wirbelsatz (translation by W. Schubert). *Meteorolol. Z.*, **59**, 277–281.

Ezer, T., Arango, H., and Shchepetkin, A. (2002). Developments in terrain-following ocean models: intercomparisons of numerical aspects. *Ocean Modelling*, **4**, 249–267.

Falkovich, G. and Lebedev, V. (1997). Single-point velocity distribution in turbulence. *prl*, **79(21)**, 4159–4161.

Falkowski, P. G., Ziemann, D., Kolber, Z., and Bienfang, P. K. (1991). The role of eddy pumping in enhancing promary production in the ocean. *Nature*, **352**, 55–58.

Farge, M. and Sadourny, R. (1989). Wave-vortex dynamics in rotating shallow water. *J. Fluid Mech.*, **206**, 433–462.

Fasham, M. J. R. (1995). Variations in the seasonal cycle of biological production in subarctic oceans: A model sensitivity analysis. *Deep-Sea Res I.*, **42(7)**, 1111–1149.

Fennel, K., Wilkin, J., J.Levin, Moisan, J., O'Reilly, J., and Haidvogeland, D. (2006). Nitrogen cycling in the Middle Atlantic Bight: Results from a three-dimensional model and implications for the North Atlantic nitrogen budget. *Global Biogeochem. Cycles*, **20**, doi:10.1029/2005GB002456.

Ferrari, R. and Paparella, F. (2003). Compensation and alignment of thermohaline gradients in the ocean mixed layer. *J. Phys. Ocean.*, **33**, 2214–2223.

Flierl, G. and McGillicuddy, D. (2002). Mesoscale and sub-mesoscale physical-biological interactions. In A. R. Robinson, J. J. McCarthy, and B. J. Rothschild, editors, *The Sea*, volume 12, pages 113–185. Harvard University Press.

Franks, P. J. S. (2002). NPZ models of plankton dynamics: their construction, coupling to physics and application. *J. Oceanogr.*, **58**, 379–387.

Gargett, A. and Marra, J. (2002). Effects of upper ocean physical processes (turbulence, advection, and air-sea interaction) on oceanic primary production. In A. R. Robinson, J. J. McCarthy, and B. J. Rothschild, editors, *The Sea*, volume 12, pages 19–49. Harvard University Press.

Gasparini, G. P., Zodiatis, G., Astraldi, M., Galli, C., and Sparnocchia, S. (1999). Winter intermediate water lenses in the Ligurian Sea. *J. Mar. Syst.*, **20**, 319–332.

Gent, P. R. and McWilliams, J. C. (1995). Isopycnal mixing in ocean circulation models. *J. Phys. Ocean.*, **20**, 150–155.

Gibson, G. A., Musgrave, D. L., and Hinckley, S. (2005). Non-linear dynamics of a pelagic ecosystem model with multiple predator and prey types. *J. Plankton. Res.*, **27(5)**, 427–447.

Gill (1982). *Atmosphere-Ocean Dynamics*. Academic Press, New York, US.

Gill, A. E. (1984). On the behavior of internal waves in the wakes of storms. *J. Phys. Ocean.*, **14**, 1129–1151.

Giordani, H., Prieur, L., and Caniaux, G. (2006). Advanced insights into sources of vertical velocity in the ocean. *Ocean Dynamics*, **56**, 513–524.

Granata, T., Wiggert, J., and Dickey, T. (1995). Trapped, near-inertial waves and enhanced chlorophyll distributions. *J. Geophys. Res.*, **100(10)**, 20793–20804.

Graves, L. P., McWilliams, J. C., and Montgomery, M. T. (2006). Vortex evolution due to straining: a mechanism for dominance of strong, interior anticyclones. *Geophys. Astrophys. Fluid Dyn.*, **100 (3)**, 151–183.

Griffa, A. (1996). Applications of stochastic particle models to oceanographical problems. In R. Adler, P.Muller, and B. Rozovskii, editors, *Stochastic Modelling in Physical Oceanography*, pages 114–140. Birkhauser.

Griffies, S. M., Boning, C., Bryan, F. O., Chassignet, E. P., Gerdes, R., Hasumi, H., Hirst, A., Treguier, A. M., and Webb, D. (2000). Development in ocean climate modelling. *Ocean Modelling*, **2**, 123–192.

Haidvogel, D. B., Arango, H., Hedstrom, K., Beckmann, A., Malanotte-Rizzoli, P., and Shchepetkin, A. (2000). Model evaluation experiments in the North Atlantic Basin: simulations in nonlinear terrain-following coordinates. *Dyn. Atmos. Oceans*, **32**, 239–281.

Hatzianastassiou, N., Matsoukas, C., Fotiadi, A., Pavlakis, K. G., Drakakis, E., Hatzidimitriou, D., and Vardavas, I. (2005). Global distribution of Earth's surface shortwave radiation budget. *Atmos. Chem. Phys.*, **5**, 2847–2867.

Herring, J. R. (1980). Statistical theory of quasi-geostrophic turbulence. *J. Atmos. Sci.*, **37**, 965–977.

Hitchcock, G. L., Mariano, A. J., and Rossby, T. (1993). Mesoscale pigment fields in the gulf stream: observations in a meander creast and trough. *J. Geophys. Res.*, **98**, 8425–8445.

Hoskins, B. J. and Bretherton, F. P. (1972). Atmospheric frontogenesis models: mathematical formulation and solution. *J. Atmos. Sci.*, **29**, 11–37.

Isern-Fontanet, J., Garcia-Ladona, E., Font, J., and Garcia-Olivares, A. (2006). Non-Gaussian velocity probability density functions: An altimetric perspective of the Mediterranean Sea. *J. Phys. Ocean.*, **36**, 2153–2164.

Ivanov, A. Y. and Ginzburg, A. I. (2002). Oceanic eddies in synthetic aperture radar images. *Proc. Indian Acad. Sci*, **111(3)**, 281–295.

Jackett, D. R. and McDougall, T. J. (1995). Minimal adjustment of hydrostatic profiles to achieve static stability. *J. Atmos. and Ocean. Tech.*, **12**, 381–389.

Jeong, J. and Hussain, F. (1995). On the indentification of a vortex. *J. Fluid Mech.*, **285**, 69–94.

Jerlov, N. G. (1976). *Marine Optics*. Elsevier Scientific Publishing Company, Amsterdam.

Jimenez, J. (1996). Algebraic probability density tails in decaying isotropic two-dimensional turbulence. *J. Fluid Mech.*, **313**, 223–240.

Killworth, P. D. (1998). Eddy parameterization in large scale flow. In E. P. Chassignet and J. Verron, editors, *Ocean Modelling and Parameterization*, pages 253–268. NATO Advanced Study Institute, Kluwer Academic Publishers.

Klein, P. and Hua, B. L. (1988). Mesoscale heterogeneity of the wind-driven mixed layer: Influence of a quasigeostrophic flow. *J. Mar. Res.*, **46**, 495–525.

Klein, P., Lapeyre, G., and Large, W. G. (2004). Wind ringing of the ocean in presence of mesoscale eddies. *Geophys. Res. Lett.*, **31**, L15306.

Koszalka, I., Bracco, A., and Provenzale, A. (2007b). Dynamics of anticyclonic eddies in the open ocean. *Phys. Lett*, in preparation.

Koszalka, I., Bracco, A., Pasquero, C., and Provenzale, A. (2007a). Plankton cycles disguised by turbulent advection. *Theoretical Population Biology*, **72(1)**, 1–6.

Kraichnan, R. and Montgomery, D. (1980). Two-dimensional turbulence. *Rep. Prog. Phys.*, **43**, 548–619.

Kundu, P. K. and Thomson, R. E. (1985). Inertial oscillations due to a moving front. *J. Phys. Ocean.*, **15**, 1076–1084.

Kunze, E. (1985). Near-inertial wave propagation in geostrophic shear. *J. Phys. Ocean.*, **15**, 544–565.

LaCasce, J. H. (2005). On the Eulerian and Lagrangian velocity distributions in the North Atlantic. *J. Phys. Ocean.*, **35**, 2327–2336.

LaCasce, J. H. and Ohlmann, C. (2003). Relative dispersion at the surface of the Gulf of Mexico. *J. Mar. Res.*, **61**, 285–312.

Large, W. G. and Gent, P. (1999). Validation of vertical mixing in an equatorial ocean model using large eddy simulations and observations. *J. Phys. Ocean.*, **29**, 449–464.

Large, W. G., McWilliams, J. C., and Doney, S. (1994). Oceanic vertical mixing: a review and a model with a non-local K-profile boundary layer parameterization. *Rev. Geophys.*, **32(4)**, 363–403.

Larichev, V. D. and McWilliams, J. C. (1991). Weakly decaying turbulence in an equivalent-barotropic fluid. *Phys. Fluids*, **3(5)**, 938–950.

Lee, D.-K., Niiler, P., Warn-Varnas, A., and Piacsek, S. (1994). Wind-driven secondary circulation in ocean mesoscale. *J. Mar. Res.*, **52**, 371–396.

Levy, M., Estublier, A., and Madec, G. (2001a). Choice of an advection scheme for biogeochemical models. *Geophys. Res. Lett.*, **28(19)**, 3725–3728.

Levy, M., Klein, P., and Treguier, A.-M. (2001b). Impact of sub-mesoscale physics on production and subduction of phytoplankton in an oligotrophic regime. *J. Mar. Res.*, **59**, 535–565.

Li, X., Chao, Y., McWilliams, J. C., and Fu, L.-L. (2001). A comparison of two vertical-mixing schemes in a Pacific Ocean general circulation model. *J. Clim.*, **14**, 1377–1398.

Mahadevan, A. (2006). Modelling vertical motion at ocean fronts: Are nonhydrostatic effects relevant at mesoscales? *Ocean Modelling*, **14**, 222–240.

Mahadevan, A. and Archer, D. (2001). Modelling the impact of fronts and mesoscale circulation on the nutrient supply and biogeochemistry in the upper ocean. *J. Mar. Res.*, **59**, 535–565.

Mahadevan, A. and Campbell, J. W. (2002). Biogeochemical patchiness at the sea surface. *Geophys. Res. Lett.*, **29(19)**, 1926–1930.

Mahadevan, A. and Tandon, A. (2006). An analysis of mechanisms for submesoscale vertical motion at ocean fronts. *Ocean Modelling*, **14**, 241–256.

Mann, K. H. and Lazier, J. R. N. (1996). *Dynamics of marine ecosystems*. Blackwell Sci., Malden, Mass., U.S.

Marchesiello, P., McWilliams, J. C., and Shchepetkin, A. (2003). Equilibrum structure and dynamics of the California Current system. *J. Phys. Ocean.*, **33**, 753–783.

Mariano, A., Griffa, A., Ozgokmen, T. M., and Zambianchi, E. (2000). Lagrangian statistics and predictability of coastal and ocean dynamics 2000. *J. Atmos. and Ocean. Tech.*, **19**, 1114–1126.

Martin, A. P. and Pondaven, P. (2003). On estimates for the vertical nitrate flux due to eddy pumping. *J. Geophys. Res.*, **108 (C11)**, doi:10.1029/2003JC001841.

Martin, A. P., Richards, K. J., and Fasham, M. J. R. (2001). Phytoplankton production and community structure in an unstable frontal region. *J. Mar. Syst.*, **28**, 65–89.

Martin, A. P., Richards, K. J., Bracco, A., and Provenzale, A. (2002). Patchy productivity in the open ocean. *Global Biogeochem. Cycles*, **16(2)**, 1025.

McGillicuddy, D. J. (2001). Models of small-scale patchiness. In J. H. Steele, K. K. Turekian, and S. Thorpe, editors, *Encyclopedia of Ocean Sciences*, volume 5, pages 2820–2833. Academic Press.

McGillicuddy, D. J., Kosnyrev, V. K., Ryan, J. P., and Yoder, J. A. (1997). Covariation of mesoscale ocean color and sea-surface temperature patterns in the Sargasso Sea. *Deep-Sea Res I.*, **44(8)**, 1427–1450.

McGillicuddy, D. J., Robinson, A. R., and coauthors (1998). Influence of mesoscale eddies on new production in the Sargasso Sea. *Nature*, **394**, 263–266.

McGillicuddy, D. J., Anderson, L. A., Bates, N. R., Bibby, T., Buesseler, K. O., Carlson, C. A., Davis, C. S., Ewart, C., Falkowski, P. G., Goldhwait, S. A., Hansell, D. A., Jenkins, W. J., Johnson, R., Kosnyrev, V. K., Ledwell, J. R., Li, Q. P., Siegel, D. A., and Steinberg, D. K. (2007). Eddy/wind interactions stimulate extraordinary mid-ocean plankton blooms. *Science*, **316**, 1021–1026.

McWilliams, J. C. (1984). The emergence of isolated coherent vortices in turbulent flow. *J. Fluid Mech.*, **146**, 21–43.

McWilliams, J. C. (1990). The vortices of two-dimensional turbulence. *J. Fluid Mech.*, **219**, 361–385.

McWilliams, J. C. (1998). Oceanic general circulation models. In E. P. Chassignet and J. Verron, editors, *Ocean Modelling and Parameterization*, pages 1–44. NATO Advanced Study Institute, Kluwer Academic Publishers.

McWilliams, J. C. and Weiss, J. B. (1994). Anisotropic geophysical vortices. *Chaos*, **4(2)**, 305–311.

McWilliams, J. C., Weiss, J. B., and Yavneh, I. (1994). Anisotropy and coherent vortex structures in planetary turbulence. *Science*, **264**, 410–413.

McWilliams, J. C., Graves, L., and T.Montgomery, M. (2003). A formal theory for vortex Rossby waves and vortex evolution. *Geophys. Astrophys. Fluid Dyn.*, **97(4)**, 275–309.

Mellor, G., Hakkinen, S., Ezer, T., and Patchen, R. (2002). A generalization of a sigma coordinate ocean model and an intercomparison of model vertical grids. In N. Pinardi and J. Woods, editors, *Ocean forecasting: conceptual basis and applications*, pages 55–72. Springer.

Mesinger, F. and Arakawa, A. (1976). *Numerical methods used in atmospheric models. GARP Publication Series no. 17. Vol. 1.* World Meteorological Organization International Council of Scientific Unions.

Millot, C. and Crepon, M. (1981). Inertial oscillations on the continetal shelf of the Gulf of Lions - observations and theory. *J. Phys. Ocean.*, **11**, 639–657.

Millot, C. and Taupier-Letage, I. (2005). Additional evidence of LIW entrainment across the Algerian subbasin by mesoscale eddies and not by permament westward flow. *J. Phys. Ocean.*, **66**, 231–250.

Min, I. A., Mezic, I., and Leonard, A. (1996). Levy stable distributions for velocity and velocity difference in systems of vortex elements. *Phys. Fluids*, **8**, 1169–1180.

Molemaker, M. J. and McWilliams, J. C. (2005). Baroclinic instability and loss of balance. *J. Phys. Ocean.*, **35 (9)**, 1505–1517.

Montgomery, M. T. and Lu, C. (1997). Free waves on barotropic vortices. part I: Eigenmode structure. *J. Atmos. Sci.*, **54**, 1868–1885.

Muller, P. and Frankignoul, C. (1981). Direct atmospheric forcing of geostrophic eddies. *J. Phys. Ocean.*, **11**, 287–308.

Munk, W., Armi, L., Fisher, K., and Zachariasen, F. (2000). Spirals on the sea. *Proc. Roy. Soc. London*, **456**, 1217–1280.

Nagai, T., Tandon, A., and Rudnick, D. L. (2006). Two-dimensional ageostrophic secondary circulation at ocean fronts due to vertical mixing and large-scale deformation. *J. Geophys. Res.*, **111**, C09038.

Nihoul, J. C. J. (1975). *Modelling of marine systems*. Elsevier, Amsterdam, The Netherlands.

Niiler, P. (1969). On the Ekman divergence in an oceanic jet. *J. Geophys. Res.*, **74**, 7048–7052.

Ohkitani, K. (1991). Wave number space dynamics of enstrophy cascade in a forced two-dimensional turbulence. *Phys. Fluids A*, **3(6)**, 1598–1611.

Oschlies, A. and Garcon, V. (1998). Eddy-induced enhancement of primary production in a model of the north atlantic ocean. *Nature*, **394**, 266–267.

Pasquero, C., Provenzale, A., and Babiano, A. (2001). Parameterization of dispersion in two-dimensional turbulence. *J. Fluid Mech.*, **439**, 279–303.

Pasquero, C., Bracco, A., and Provenzale, A. (2004). Coherent vortices, Lagrangian particles and the marine ecosystem. In G. H. Jirka and W. S. J. Uijttewaal, editors, *Shallow Flows*, pages 339–412. A. A. Balkema Publishers.

Pasquero, C., Bracco, A., and Provenzale, A. (2005). Impact of the spatiotemporal variability of the nutrient flux on primary productivity in the ocean. *J. Geophys. Res.*, **11**, 1–13.

Paulson, C. A. and Simpson, J. J. (1977). Irradiance measurements in the upper ocean. *J. Phys. Ocean.*, **7**, 952–956.

Pedlosky, J. (1987). *Geophysical Fluid Dynamics*. Springer Verlag, New York, US, second edition.

Penven, P., Lutjeharms, J. R. E., Marchesiello, P., Roy, C., and Weeks, S. J. (2001). Generation of cyclonic eddies by the Agulhas Current in the lee of the Agulhas Bank. *Geophys. Res. Lett.*, **27**, 1055–1058.

Penven, P., Debreu, L., Marchesiello, P., and McWilliams, J. C. (2006). Evaluation and application of the ROMS 1-way embedding procedure to the central california upwelling system. *Ocean Modelling*, **12**, 157–187.

Petersen, M. R., Julien, K., and Weiss, J. B. (2006). Vortex cores, strain cells, and filaments in quasigeostrophic turbulence. *Phys. Fluids*, **18**, 026601.

Pierrehumbert, R. T., Held, I. M., and Swanson, K. L. (1994). Spectra of local and nonlocal two-dimensional turbulence. *Chaos, Solitons & Fractals*, **4(6)**, 1111–1116.

Pinot, J.-M., Tintore, J., and Wang, D.-P. (1996). A study of the omega equation for diagnosing vertical motions at ocean fronts. *J. Mar. Res.*, **54**, 239–259.

Pollard, R. T. (1980). Properties of near-surface inertial oscillations. *J. Phys. Ocean.*, **10**, 385–398.

Pollard, R. T. and Regier, L. A. (1992). Vorticity and vertical circulation at an ocean front. *J. Phys. Ocean.*, **22**, 609–625.

Polvani, L. M., McWilliams, J. C., Spall, M. A., and Ford, R. (1994). The coherent structures of shallow-water turbulence: deformation radius effects, cyclon/anticyclone asymmetry and gravity-wave generation. *Chaos*, **4(2)**, 177–186.

Polzin, K. and Ferrari, R. (2004). Isopycnal dispersion in NATRE. *J. Phys. Ocean.*, **34**, 247–257.

Poulain, P.-M. (2001). Adriatic Sea surface circulation as derived from drifter data between 1990 and 1999. *J. Mar. Syst.*, **29**, 3–32.

Powell, T. M. and Okubo, A. (1994). Turbulence, diffusion and patchiness in the sea. *Phil. Trans. Roy. Soc. London B*, **343**, 11–18.

Provenzale, A. (1999). Transport by coherent barotropic vortices. *Ann. Rev. Fluid Mech.*, **31**, 55–93.

Rabinovich, A. B., Thomson, R. E., and Bograd, S. J. (2002). Drifter observations of anticyclonic eddies near Bussol' Strait, the kuril islands. *J. Ocean.*, **58**, 661–671.

Rainville, L. and Pinkel, R. (2005). Propagation of low-mode internal waves through the ocean. *J. Phys. Ocean.*, page submitted.

Reynolds, A. M. (2002). Lagrangian stochastic modelling of anomalous diffusion in two-dimensional turbulence. *Phys. Fluids*, **14(4)**, 1142–1449.

Richardson, L. F. (1926). Atmospheric diffusion shown on a distance-neighbor graph. *Proc. Roy. Soc. London A*, **110**, 709–737.

Roberts, M. and Marshall, D. (1998). Do we require adiabatic dissipation schemes in eddy-resolving ocean models? *J. Phys. Ocean.*, **28**, 2050–2063.

Robinson, A., McGillicuddy, D. J., Calman, J., Ducklow, H. W., Fasham, M. J. R., Hoge, F. E., Leslie, W. G., McCarthy, J. J., Podewski, S., and Porter, D. L. (1993). Mesoscale and upper ocean variabilities during the 1989 JGOFS bloom study. *Deep-Sea Res II.*, **40(1-2)**, 9–35.

Rodean, H. C. (1996). *Stochastic Lagrangian models of turbulent diffusion*. Americal Meteorological Society, Boston, Massachusetts, US.

Rubenstein, D. M. (1984). Vertical dispersion of inertial waves in the upper ocean. *J. Geophys. Res.*, **88(C7)**, 4368–4380.

Ryabchenko, V. A., Fasham, M. J. R., Kagan, B. A., and Popova, E. E. (1997). What causes short-term oscillations in ecosystem models of the ocean mixed layer? *J. Mar. Syst.*, **13**, 33–50.

Salmon, R. (1998). *Lectures On Geophysical Fluid Dynamics*. Oxford University Press, New York, US.

Santangelo, P., Benzi, R., and Legras, B. (1989). The generation of vortices in high-resolution, two-dimensional decaying turbulence and the influence of initial conditions on the breaking of self-similarity. *Phys. Fluids*, **1(6)**, 1027–1034.

Schorghofer, N. (2000). Energy spectra of steady two-dimensional turbulent flows. *Phys. Rev. E*, **61(6)**, 6572–6577.

Serra, N., Ambar, I., and Kase, R. H. (2005). Observations and numerical modelling of the Mediterranean outflow splitting and eddy generation. *Deep-Sea Res. II*, **52**, 383–408.

Shchepetkin, A. (October 18-20, 2004). Overview of evolution of computational kernel of ROMS: how different things add up to make an ocean model. *ROMS/TOMS European Workshop, Venice, Palazzo Papadopoli*.

Shchepetkin, A. and McWilliams, J. C. (1998). Quasi-momotone advection schemes based on explicit locally adaptive dissipation. *Mon. Weath. Rev.*, **126**, 1541–1580.

Shchepetkin, A. and McWilliams, J. C. (2005). The regional oceanic modelling system (ROMS): a split-explicit, free-surface, topography-following-coordinate oceanic model. *Ocean Modelling*, **9**, 347–404.

Shearman, R. K., Barth, J. A., and Kosro, P. M. (1999). Diagnosis of the three-dimensional circulation associated with mesoscale motion in the California Current. *J. Phys. Ocean.*, **29**, 651–670.

Siegel, D. A., Granata, T. C., Michaelis, A. F., and Dickey, T. D. (1990). Mesoscale eddy diffusion, particle sinking, and the interpretation of sediment trap data. *J. Geophys. Res.*, **95(C4)**, 5305–5311.

Smedsrud, L. H., Budgell, W. P., Jenkins, A. D., and Adlandsvik, B. (2006). Fine-scale sea-ice modelling of the Storfjorden polynya. *Annals Glaciol.*, **44**, 73–79.

Smith, C. L., Richards, K. J., and Fasham, M. J. R. (1996). The impact of mesoscale jet activity on plankton dynamics in the upper ocean. *Deep-Sea Res I.*, **4311-12)**, 1807–1832.

Smith, K. S. and Vallis, G. K. (2001). The scales and equilibration of midocean eddies: freely evolving flow. *J. Phys. Ocean.*, **31**, 554–571.

Song, Y. T. and Haidvogel, D. (1994). A semi-implicit ocean circulation model using a generalized topography following coordinate coordinate system. *J. Comp. Phys.*, **115**, 228–248.

Spall, M. A., Pickart, R. S., Fratantoni, P. S., and Plueddeman, A. J. (2007). Western Arctic shelfbreak eddies: formation and transport. *J. Phys. Ocean.*, page submitted.

Spall, S. A. and Richards, K. J. (2000). A numerical model of mesoscale frontal instabilities and plankton dynamics: I. Model formulation and initial experiments. *Deep-Sea Res.*, **47**, 1261–1301.

Srokosz, M. A. (2000). Biological oceanography by remote sensing. In R. A. Meyers, editor, *Encyclopedia of Analytical Chemistry*, pages 8506–8533. John Wiley & Sons Ltd.

Stammer, D. (1997). Global characteristics of ocean variability estimated from regional TOPEX/POSEIDON altimeter measurements. *J. Phys. Ocean.*, **27**, 1743–1769.

Steele, J. H. and Henderson, W. (1981). A simple plankton model. *Am. Nat.*, **117**, 676–691.

Steele, J. H. and Henderson, W. (1992). The role of predation in plankton models. *J. Plankton. Res.*, **14(1)**, 152–172.

Stone, P. H. (1966). On non-geostrophic baroclinic instability. *J. Atmos. Sci.*, **23**, 390–400.

Sweeney, E. N., McGillicuddy, D. J., and Buesseler, K. O. (2003). Biogeochemical impacts due to mesoscale eddy activity in the Sargasso Sea as measured at the Bermuda Atlantic Time-series Study (BATS). *Deep-Sea Res II.*, **50**, 3017–3039.

Swenson, M. S. and Niiler, P. P. (1996). Statistical analysis of the surface circulation of the california current. *J. Geophys. Res.*, **101(C10)**, 22631–22645.

Taylor, G. I. (1921). Diffusion by continuous mouvements. *Proc. Lond. Math. Soc*, **20**, 196–212.

Testor, P. and Gascard, J.-C. (2003). Large-scale spreading of deep waters in the Western Mediterranean Sea by submesoscale coherent eddies. *J. Phys. Ocean.*, **33 (1)**, 75–87.

Thomas, L. N. (2005). Destruction of potential vorticity by winds. *J. Phys. Ocean.*, **35**, 2457–2466.

Thomas, L. N. (2007). Formation of intrathermocline eddies at ocean fronts by wind-driven destruction of potential vorticity. *Dyn. Atmos. Ocean*, **accepted**.

Thomas, L. N. and Rhines, P. B. (2002). Nonlinear stratified spin-up. *J. Fluid Mech.*, **473**, 211–214.

Thomas, L. N., Tandon, A., and Mahadevan, A. (2007). Submesoscale processes and dynamics. *In: M. Hecht, H. Hasumi (Eds.),Eddy Resolving Ocean Modeling. AGU, Washington, DC*, page submitted.

Tintore, J., Gomis, D., Alonso, S., and Porrilla, G. (1991). Mesoscale dynamics and vertical motion in the Alboran Sea. *J. Phys. Ocean.*, **21**, 811–823.

Tokos, K. S. and Rossby, T. (1991). Kinematics and dynamics of a Mediterranean salt lense. *jpo*, **21**, 879–892.

Truscott, J. E. and Brindley, J. (1994). Equilibra, stability and excitability in a general class of plankton population models. *Phil. Trans. Roy. Soc. London A*, **347**, 703–718.

Tung, K. K. and Welch, W. T. (2001). Remarks on Charney's note on geostrophic turbulence. *J. Atmos. Sci.*, **58**, 2009–2012.

V.-Belchi, P. and Tintore, J. (2001). Vertical velocities at an ocean front. *Scientia Marine*, **65(1)**, 291–300.

Vallis, G. (2006). *Atmospheric and oceanic fluid dynamics*. Cambridge University Press, New York, US.

Vandermeer, J. H. and Goldberg, D. E. (2003). *Population ecology: first principles*. Princeton University Press, New Yersey.

Veneziani, M., Griffa, A., Reynolds, A. M., and Mariano, A. J. (2004). Oceanic turbulence and stochastic models from subsurface Lagrangian data for the Northwest Atlantic Ocean. *J. Phys. Ocean.*, **34**, 1884–1906.

Veneziani, M., Griffa, A., Garraffo, Z. D., and Chassignet, E. P. (2005). Lagrangian spin parameter and coherent structures from trajectories released in a high-resolution ocean model. *J. Mar. Res.*, **63**, 753–788.

Visbeck, M., Marshall, J., Haine, T., and Spall, M. (1997). Specification of eddy transfer coefficients in coarse-resolution ocean circulation models. *J. Phys. Ocean.*, **27**, 381–402.

von Hardenberg, J., McWilliams, J. C., Provenzale, A., Shchepetkin, A., and Weiss, J. B. (2000). Vortex merging in quasi-geostrophic flows. *J. Fluid Mech.*, **412**, 331–353.

Wakatsuchi, M. and Ohshima, K. I. (1990). Observations of ice-ocean eddy streets in the Sea of Okhotks off the Hokkaido coast using radar images. *J. Phys. Ocean.*, **20**, 585–595.

Wang, Y. (2002). Vortex rossby waves in a numerically simulated tropical cyclone. Part I: Overall structure, potential vorticity and kinetic energy budgets. *J. Atmos. Sci.*, **59**, 1213–1237.

Weiss, J. (1981). The dynamics of enstrophy transfer in two-dimensional turbulence. *Physica D*, **48**, 273–294.

Weiss, J. B., Provenzale, A., and McWilliams, J. C. (1998). Lagrangian dynamics in high-dimensional point-vortex systems. *Phys. Fluids*, **10**, 1929–1941.

Wiggert, J. D., Hood, R. R., Banse, K., and Kindle, J. C. (2005). Monsoon-driven biogeochemical processes in the arabian sea. *Progr. Oceanogr*, **65**, 176–213.

Williams, R. G. and Follows, M. J. (2003). Physical transport of nutrients and the maintenance of biological production. In M. J. R. Fasham, editor, *Ocean Biogeochemistry: The role of the ocean carbon cycle in global change*, pages 19–51. Springer. ISBN: 3-540-42398-2.

Young, W. R., Rhines, P. B., and Garrett, C. J. R. (1982). Shear-flow dispersion, internal waves and horizontal mixing in the ocean. *J. Phys. Ocean.*, **12**, 515–527.

Chapter A-1

Appendix

A-1 Time-stepping technique

A-1 .1 Barotropic time stepping

Each baroclinic time step corresponds to m=$(1, \ldots M)$ barotropic time steps. In practice however, the barotropic time-stepping is performed after the first baroclinic substep (described in the section A-1 .3). At time index $m = 0$, before integration starts, the barotropic momenta are set to the values of the vertical average of the baroclinic momenta at n. During the first barotropic time step $m = 1$, the predictor step is Forward-Euler and the corrector step is Background-Euler. Otherwise, the predictor step is Leap-Frog and the corrector step is third-order Adams-Moulton with Adams-Bashforth interpolation. The LF/AM3 time-marching procedure for barotropic equations can be summarized below.

I. Predictor Leap-Frog Substep:

1. Compute total depth $h^m = H + \eta^m$ and vertically integrated mass fluxes $h^m(\tilde{u}^m dy,\ \tilde{v}^m dx)$.

2. Leap-Frog free-surface η from the divergence of vertically integrated barotropic mass flux:

$$\eta^{m+1/2} = \eta^m - 2\delta t\, \nabla \cdot (h^m \tilde{u}^m dy,\ h^m \tilde{v}^m dx). \tag{A-1}$$

3. Calculate time-interpolated free-surface for barotropic pressure gradient:

$$\eta_G = (1 - 2\gamma)\eta^{m-1} + \gamma\eta^m + \eta^{m+1/2}, \quad \gamma = \frac{4}{25}.$$

4. Update total depth $h^{m+1/2} = H + \eta^{m+1/2}$.

5. Calculate the r.h.s for barotropic momentum with fast contribution due to pressure gradient $\nabla p^*(\eta_G)$ and vertically integrated baroclinic terms $rhs(\tilde{\mathbf{u}})^*$ which will be held fixed during barotropic time marching.

6. Calculate the r.h.s for intermediate time momentum by AB3 interpolation:

$$rhs(\tilde{\mathbf{u}})^{m+1/2} = \nabla p^*(\eta_G) + \frac{23}{12} rhs(\tilde{\mathbf{u}})^* - \frac{16}{12} rhs(\tilde{\mathbf{u}})^{m-1} + \frac{5}{12} rhs(\tilde{\mathbf{u}})^{m-2}.$$

7. Leap-Frog barotropic momentum $\tilde{\mathbf{u}}$:

$$\tilde{\mathbf{u}}^{m+1/2} = \frac{1}{h^{m+1/2}} \left(h^m \tilde{\mathbf{u}}^m + \delta t\, rhs(\tilde{\mathbf{u}})^{m+1/2} \right).$$

II. Corrector Adams-Molton Substep:

1. Update s-coordinate by eq. (5.10) and vertically integrated mass fluxes $h^{m+1/2}(\tilde{u}^{m+1/2} dy,\ \tilde{v}^{m+1/2} dx)$.

2. Sub-step free-surface η using AM3 method:

$$\eta^{m+1} = \eta^m - \delta t \left(\frac{5}{12} \nabla \cdot (\tilde{\mathbf{u}}^{m+1/2}) + \frac{8}{12} \nabla \cdot (\tilde{\mathbf{u}}^m) - \frac{1}{12} \nabla \cdot (\tilde{\mathbf{u}}^{m-1}) \right).$$

3. Calculate time interpolated free-surface for barotropic pressure gradient:

$$\eta_G = \frac{3}{5}\eta^{m+1} + \frac{2}{5}\eta^{m+1/2}.$$

4. Update total depth $h^{m+1} = H + \eta^{m+1}$.

5. Sub-step barotropic momentum $\tilde{\mathbf{u}}$ using AM3 method:

$$\tilde{\mathbf{u}}^{m+1} = \frac{h^m}{h^{m+1}}\tilde{\mathbf{u}}^m + \frac{\delta t}{h^{m+1}}\left(\frac{5}{12}\left(\nabla p^*(\eta_G) + rhs(\tilde{\mathbf{u}})^*\right) + \frac{8}{12}rhs(\tilde{\mathbf{u}})^m - \frac{1}{12}rhs(\tilde{\mathbf{u}})^{m-1}\right).$$

The spatial discretization of the Coriolis term $h^{m+1}\left(-fu^{m+1}, fv^{m+1}\right)$ ensures no contribution to the kinetic energy integral: the velocity components (u, v) are interpolated first to the location of r-points on the "C" grid, where they are multiplied by the Coriolis parameter f and total depth h. The products are then interpolated futher to the locations of the partner component and multiplied.

A-1 .2 Barotropic/baroclinic mode coupling

The velocity fluxes in the model are defined in *finite volume* and *finite time* senses. This means that during a time interval Δt the sum of baroclinic fluxes across the moving facets of the grid element $\Delta\mathcal{V}$ produce a change in the volume of fluid inside that is equivalent to the difference of $\Delta\mathcal{V}^{n+1}_{i,j,k}$ -$\Delta\mathcal{V}^{n}_{i,j,k}$. By the eq. (5.10) this difference is determined by a fast variable, the free-surface which is advanced in time separately. In order to avoid the errors associated with the aliasing of frequencies resolved by the barotropic steps but unresolved by the baroclinic step, the barotropic fields are time-averaged before they replace those values obtained with a longer baroclinic step. The model employs a power-law time

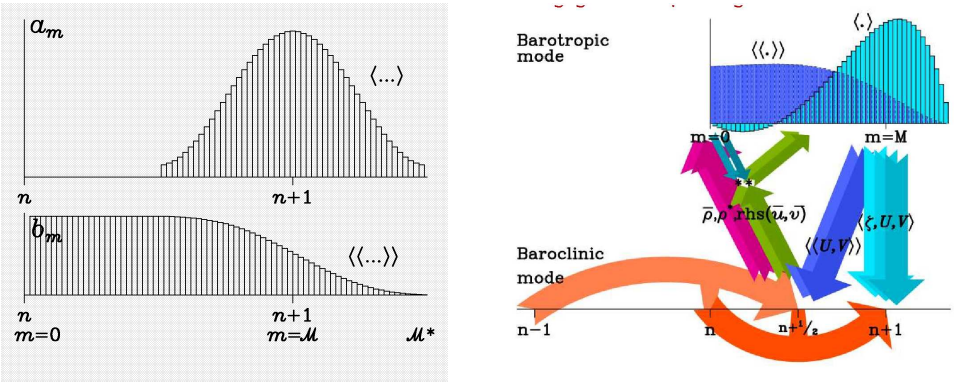

Figure A-1 .1: Details on time-stepping procedure of ROMS. (a) Structure of the fast-time-averaging filter: primary weights (top) and corresponding secondary weights (bottom). Small tickmarks symbolize the fast (barotropic) time steps, and large ones labeled by n and n+1 are the old and new baroclinic steps. (b) Barotropic – baroclinic mode data exchange: Curved horizontal arrows symbolize the predictor LF step combined with AM3 half-step-back interpolation of the result (light shading) and corrector substep (dark shading). The four ascending arrows denote the n-step densities and forcing terms for barotropic mode used during the baroclinic corrector substep during the barotropic time stepping. The five large descending arrows symbolize fast-time averaged barotropic variables for backward coupling. Each arrow originates at the time when the data is logically available. From Shchepetkin and McWilliams (2005).

filter to average the barotropic fields. The filter function is characterized by a set of primary weights

a^m which satisfy:

$$\sum_{m=1}^{M^*} \mathsf{a}^m \equiv 1, \quad \sum_{m=1}^{M^*} \frac{m}{M} \mathsf{a}^m \equiv 1, \quad m = 1, \ldots, M^*, \tag{A-2}$$

where m and n are fast and slow time indices: $m = 0$ corresponds to the baroclinic step n, while $m = M = \Delta t/\delta t$ corresponds to the step $n+1$ and M^* is the last index at which $\mathsf{a}^m \neq 0$. The number M is chosen by the modeler. Too small values of M may result in non-negligible start-up effects during each baroclinic time-step and the ROMS community "cooking experience" suggests the value of $M = 50 - 60$. During the initialization phase of the simulation the weights and M^* are found interactively so that the normalization condition (eq. A-2) is satisfied and the center of gravity of the shape function is exactly M; Thus barotropic time marching overshoots the $n+1$ baroclinic time step (Shchepetkin and McWilliams, 2005). The weights of the power-law filter employed in the ROMS version 2.2 are determined in the iteraction procedure as:

$$\begin{aligned} \mathsf{a}^m =& \mu_i^{c_1} \cdot (1 - \mu_i^{c_2}) - c_3 \cdot \mu_i, \quad \mu_i = \varepsilon \cdot i/M \\ \varepsilon =& \frac{(c_1 + 1.0)(c_1 + c_2 + 1.0)}{(c_1 + 2.0)(c_1 + c_2 + 2.0) \cdot M}, \quad i = 1, \ldots, 2M \end{aligned} \tag{A-3}$$

where $c_1 = 2.0$, $c_2 = 4.0$ and $c_3 = 0.284$ are default values are chosen to yield second-order temporal accuracy for time-averaged barotropic motions resolved by baroclinic time-step. Additionally, the value of c_3 assures the best stability properties unless the M is not too small. Once the set of primary weights a^m is specified, the slow-time quantities are defined:

$$< \eta >^{n+1} = \sum_{m=1}^{M^*} \mathsf{a}^m \eta^m, \quad < U >^{n+1} = \sum_{m=1}^{M^*} \mathsf{a}^m U^m, \tag{A-4}$$

where η^m, U^m are "instantenous" barotropic variables. From the procedure described in Sect. A-1 .1 one has:

$$< \eta >^{n+1} = < \eta >^n - \Delta t \, \nabla \cdot \Big(\sum_{m'=1}^{M^*} b_{m'} U^{m'-1/2} \Big) \;\; \text{where} \;\; b_{m'} = \frac{1}{M} \sum_{m=m'}^{M^*} \mathsf{a}^m \tag{A-5}$$

are the secondary weights (Fig. A-1 .1 a). The barotropic mode *restarts* at every baroclinic time step; that is at every baroclinic step the instantenous values of η and U are replaced with their fast-time averages in the sense of eq. (A-4), which assures that:

$$<< U >>^{n+1} = \sum_{m=1}^{M^*} b_m U^{m-1/2}, \tag{A-6}$$

which is exact slow-time volume conservation (Shchepetkin and McWilliams, 2005).

A-1 .3 Baroclinic time stepping

The baroclinic mode uses a generalized trapezoidal rule for LF/AM3 (Shchepetkin, 2004) which can be summarized as follows:

1. Using a predictor LF step combined with backward AB3 interpolation, calculate the previous-time step contributions:

$$u^* = u^n - \Delta t \left(-\frac{16}{12} \cdot rhs(u^{n-1}) + \frac{5}{12} \cdot rhs(u^{n-2}) \right). \tag{A-7}$$

2. Evaluate provisional variable ϕ^* from tracer forcing and advection by n-step velocities. Perform the predictor LF step with backward interpolation with AB3-like coefficients placing the resultant values at $n+1/2$:

$$\phi^{n+1/2} = \frac{5}{12}\phi^* + \frac{8}{12}\phi^n - \frac{1}{12}\phi^{n-1} \tag{A-8}$$

3. Compute the r.h.s in eq. (4.1) at time step n: pressure-gradient, Coriolis, advective terms and horizontal diffusion that will serve as forcing terms for barotropic equations. Compute diagnostically density and vertically averaged density ρ_o.

4. Barotropic time stepping described in Section A-1 .1. The baroclinic forcing terms are kept constant during this procedure, only the barotropic pressure gradient is recomputed.

5. Update vertical coordinate system is by eq. (5.10). Finalize the computation of the 3D mass fluxes using now available h^{n+1} and vertical thicknesses ds^{n+1}:

$$u^{n+1} = u^* - \frac{dt}{(dxdyds)^{n+1}}\left(\frac{23}{12}\cdot rhs(u^n)(dxdyds)^n\right) \tag{A-9}$$

Advance vertical mixing using new calculated depths. Restart the barotropic equations.

6. Interpolate the velocity components back in time to $n+1/2$ using a combination of of values from the predictor step and old time-step values $u^{n+1/2}=(u^n + u^*)/2$ corrected to ensure that their vertical integrals are equal to $<< U^{n+1/2} >>$. Calculate diagnostically vertical velocities.

7. The necessity for a conservative, constancy-preserving algorithm for tracers makes it necessary to update the velocities before the tracers get advected. Advect $\phi^{n+1/2}$ by freshly computed $u^{n+1/2}$. Time-step biological model if so intended.

This resulting time-stepping algorithm is both conservative and constancy-preserving due to slow-fast mode coupling at every baroclinic time step n (restart of the barotropic terms) and every half-step $n+1/2$ (vertical flux correction at stage 6 of the baroclinic time marching procedure). The storage requirements are reduced by using the same arrays for the newly-computed variables after predictor and corrector susbsteps. The additional computational cost of the predictor-corrector technique relative to the centered scheme, due to the elevated number of stages, may be offset by allowing the use of a larger time step and, inverse stability analysis method suggests that the Courant number for the barotropic scheme applied in ROMS can be as high as 1.14 (Shchepetkin and McWilliams, 2005). In practice however, the stability properties are additionally affected by vertical stratification, imposed topography and forcing and the resulting time-step is usually larger then theoretically predicted.